Max Planck Institute of Colloids and Interfaces
Theory and Bio-Systems

Light-induced transformations in biomembranes

Dissertation
zur Erlangung des akademischen Grades
"doctor rerum naturalium"
(Dr. rer. nat.)
in der Wissenschaftsdisziplin "Biochemie"

eingereicht an der
Mathematisch-Naturwissenschaftlichen Fakultät
der Universität Potsdam

von
Vasil Georgiev

Potsdam, den 4.1.2017

Published online at the
Institutional Repository of the University of Potsdam:
URN urn:nbn:de:kobv:517-opus4-395309
http://nbn-resolving.de/urn:nbn:de:kobv:517-opus4-395309

Disclamer

No part of this thesis has been published, but parts will be submitted for publication:

Chapter 3 – Light-induced morphological transitions in GUVs (*working title*) **Vasil Georgiev**, Andrea Grafmüller, Stefan Hecht, David Bléger, Sonja Kunstmann, Stefanie Barbirz, Reinhard Lipowsky, Rumiana Dimova.
Chapter 4 - Light control of the lipid lateral organization (*working title*) **Vasil Georgiev**, Stefan Hecht, David Bléger, Rumiana Dimova.

All data of this thesis was obtained by me, Vasil Georgiev, except the molecular dynamics simulations (3.1.5) which were performed by Andrea Grafmüler

Potsdam, 04.01.2017

Vasil Georgiev

Acknowledgements

First of all, I would like to thank my supervisor, Rumy Dimova, who gave me the freedom to work on my own, but always guided and pointed me in the right direction. I am extremely lucky to have such an approachable and helpful supervisor. *Благодаря ти, Руми!* I would also like to thank Prof. Lipowsky for the fruitful discussions and financial support. Countless thanks to my friends and colleagues at Max Planck Institute of Colloids and Interfaces for making my time there a great and special experience. In particular, I would like to thank Rafa, Tom, David, Bastian, Roland, Jan, Carmen, Ella, Kasia, Yun, Debjit, Rene, Nico, Ziliang, Vaida, Rusi, Mehmet, José, Vale, and Anja. Many thanks to Susi and Frau Ziegler for helping me to find my way in the incomprehensible for me world of documentation.

I would like to thank all the people, who collaborated with me throughout this work. In particular, I am very thankful to David Blegér for providing the photosensitive molecules and for the inspiring discussions. I am also very grateful to Andrea Grafmüller for performing all computational simulations in this work and sharing her knowledge. I thank Stefanie Barbirz for the enjoyable discussions and the opportunity to collaborate.

I would like to thank few persons, who have not been involved in this work, but whose tremendous support I have always had. Thank you, Ico, Stanko and Cheff for your priceless friendship.

My research was funded by IMPRS on Multiscale Biosystems research school. I would like to thank the whole team of the school for the support.

Finally, I would like to thank Sonja, who was always next to me during my PhD and helped me the most. Herzlichen Dank, Sonja!

Безкрайни благодарности на моето семейство за подкрепата и вярата в мен!

Abstract

Cellular membranes constantly experience remodeling, as exemplified by morphological changes during endo- and exocytosis. Regulation of membrane morphology is essential for these processes. In this work, we attempt to establish a regulation path based on the use of photoswitches exhibiting conformational changes in model membranes, namely, giant unilamellar vesicles (GUVs). The mechanism of the changes in the GUVs' morphology caused by isomerization of the photosensitive molecules has been previously explored but still remains elusive. We examine the morphological reshaping of GUVs in the presence of the photoswitch o-tetrafluoroazobenzene (F-azo) and show that the mechanism behind the resulting morphological changes involves both an increase in the membrane area and generation of a positive spontaneous curvature. First, we characterize the partitioning of F-azo in a single-component membrane using both experimental and computational approaches. The partition coefficient calculated from molecular dynamic simulations agrees with experimental data obtained with size-exclusion chromatography. Then, we implement the approach of vesicle electrodeformation in order to assess the increase in the membrane area, which is observed as a result of the conformational change of F-azo. Finally, the local and the effective membrane spontaneous curvatures were estimated from the observed shapes of vesicles exhibiting outward budding. We then extend the application of the F-azo to multicomponent lipid membranes, which exhibit a coexistence of domains in different liquid phases due to a miscibility gap between the lipids. We perform initial experiments to investigate whether F-azo can be employed to modulate the lateral lipid packing and organization. We observe either complete mixing of the domains or the appearing of disordered domains within the domains of more ordered phase. The type of behavior observed in response to the photoisomerization of F-azo was dependent on the used lipid composition. We believe that the findings introduced here will have an impact in understanding and controlling both lipid phase modulation and regulation of the membrane morphology in membrane systems.

Zusammenfassung

Zelluläre Membranen durchlaufen ständige Formveränderungen wie zum Beispiel bei der Endo- und Exozytose. Für diese und andere Prozesse ist eine Regulierung der Membranmorphologie notwendig. In der vorliegenden Arbeit wurden riesen unilamellare Vesikel (*giant unilamellar vesicles,* GUVs) als Modelmembranen genutzt. Änderungen der Vesikelform wurde durch lichtschaltbare Moleküle (Fotoschalter) erzielt. Dass die Isomerisierung von lichtempfindlichen Molekülen eine Verformung von GUV ermöglichen kann, war bekannt. Jedoch war der zugrunde liegende Mechanismus unklar.
In dieser Arbeit wurde zur Untersuchung dieses Mechanismus o-Tetrafluoroazobenzol (F-azo) als Fotoschalter verwendet. Damit konnte gezeigt werden, dass sowohl eine Vergrößerung der Membranfläche als auch das Entstehen einer positiven, spontanen Membrankrümmung den morphologischen Veränderungen zu Grunde liegen. Durch experimentelle und computergestützte Methoden konnte zunächst die Verteilung von F-azo in Membranen, die aus nur einer Komponente bestehen, quantifiziert werden. Der Verteilungskoeffizient aus molekular-dynamik Simulationen stimmte dabei mit den experimentellen Daten aus der Größenausschluss-Chromatographie überein. Im Anschluss bestimmten wir die Änderung der Membranfläche mit Hilfe von GUV-Verformung durch elektrische Felder, und konnten die Veränderung der lokalen und effektiven spontanen Membrankrümmung durch Beobachtung der Vesikelformen abschätzen.

Um herauszufinden ob F-azo die laterale Verdichtung und Organisation von Membranlipiden moduliert, weitteten wir die Experimente auf mehr-komponenten Membranen aus. Diese sind durch die Koexistenz von Domänen zweier flüssiger Lipid-Phasen gekennzeichnet. Wir konnten sowohl das Auftreten von Domänen ungeordneter Lipidphasen in geordneten Lipidphasen beobachten, als auch die Entstehung homogener GUVs durch komplette Mischung beider Lipidphasen. Wir konnten zeigen, dass die unterschiedliche Beeinflussung der Domänen durch die Licht-induzierte Isomerisierung von F-azo dabei von der Zusammensetzung der Membranen abhängig ist.
Mit den hier beschriebenen Ergebnissen legen wir einen Grundstein, für die lichtinduzierte Kontrolle über Membranenmorphologien sowie für die Foto-Modulation von Lipidphasen.

Table of contents

1 Introduction 1

1.1 Lipids and lipid membranes 1

1.2 Models of the cell membrane 3

1.3 Membrane mechanical properties and morphologies. Techniques to study them in GUVs. 4

1.3.1 Mechanical properties of the bilayers and preferred vesicle shapes 4

1.3.2 Techniques to study membrane material properties employing GUVs 7

1.4 Cell membrane and different membrane shapes existing in nature 8

1.5 The role of light in biomimetic models of membrane shape transformations 11

1.5.1 External stimuli which cause changes in the GUV shape 11

1.5.2 Light and photosensitive molecules 11

1.6 Multicomponent lipid bilayers 13

1.7 Molecular dynamic simulations of phospholipid bilayers 16

2 Methods 18

2.1 Molecules 18

2.2 Preparation of vesicles 19

2.3 Vesicle observation 20

2.4 Electrodeformation of giant vesicles 21

2.5 Fluorescence recovery after photobleaching (FRAP) 23

2.6 Fluctuation spectroscopy 25

3 Light-induced morphological transformations in GUVs 28

3.1 Methods 30

3.1.1 Vesicle preparation 30

3.1.2 Dynamic light scattering (DLS) of F-azo and LUVs 30

3.1.3 Vesicle imaging 30

3.1.4 Vesicle electrodeformation 31

3.1.5 Molecular Dynamics simulations 31

3.1.6 Size exclusion chromatography 32

3.1.7 Effect of the sugar asymmetry on the spontaneous curvature 32

3.2 Results 33

3.2.1 Behavior of the F-azo molecules in solution 34

3.2.2 F-azo partitioning in the membrane 35

3.2.3 A vesicle response to F-azo isomerization 36
3.2.4 Energy of F-azo flip-flop and desorption from membrane 37
3.2.5 Calculation of F-azo partition coefficients from MD simulations 38
3.2.6 Area change caused by F-azo isomerization 39
3.3 Discussion 43
3.4 Conclusion 47
4 Light control of the lipid lateral organization 48
4.1 Methods 49
4.1.1 Preparation of multicomponent GUVs 49
4.1.2 Determination of the miscibility temperature of GUV membranes in the presence of F-azo before and after the photoisomerization 50
4.1.3 Measuring the lateral lipid mobility in the presence of F-azo 51
4.1.4 Fluctuation analysis 51
4.2 Results 52
4.2.1 Light-induced changes in the phase state of phase-separated GUVs 52
4.2.2 Influence of F-azo conformation on miscibility temperatures in DPPC/DOPC/Chol membranes 53
4.2.3 Diffusion coefficient of l_d and l_o phase in the presence of *trans* F-azo 55
4.2.4 Effect of F-azo on the bending stiffness of the membrane 58
4.3 Discussion 59
4.4 Conclusion 61
5 Summary and outlook 62
Appendix 63
Bibliography 65
List of Abbreviations 79
List of figures 80

1 Introduction

The regulation of lipid membrane structure and morphology is critical for many cellular processes. For example, changes in membrane morphology are observed during the fission-fusion sequence in vesicular transport or endo- and exocytosis. Here, we used photosensitive molecules to modulate the membrane morphology. In addition, the photosensitive molecules were employed to probe the lipid organization in the liquid-liquid phase coexistence.

This thesis is arranged as follows. Each chapter starts with an overview to the subject and the specific goals of the study. Chapter 1 introduces a general outline of the thesis and gives a notion for the concepts and terminology relevant throughout this work. Features of phospholipid bilayer morphology and phases which are essential for the next chapters are reviewed. Of specific interest is how light can be exploited in cell model systems to explore complex biological processes. Chapter 3 describes vesicle morphological transitions triggered by light. We propose a possible mechanism for the observed morphological changes. In Chapter 4 we explore perturbations in membrane organization in the presence of photosensitive molecules. We investigated the latter probing key material properties of lipid membranes such as lateral diffusion and bending rigidity.

1.1 Lipids and lipid membranes

Lipids are amphiphilic molecules consisting of a hydrophilic (polar head) and hydrophobic (tail) part (Fig. 1-1A). The main lipid class found in biological membranes is phospholipids (PLs) which have a diverse structure in relation to both the phosphate-containing head group and the hydrophobic part composed of two fatty acyl chains (hydrocarbon chains). Depending on the polar head group, the naturally occurring phospholipids are either neutral (zwitterionic) or negatively charged at a physiological pH. The most common zwitterionic ones are: phosphatidylcholines (PCs), phosphatidylethanolamines (PEs) and sphingomyelins (SMs) while the class of negatively charged is presented by phosphatidylserines (PSs) and phosphatidylinositols (PIs).

PCs and PEs are the main lipids found in cells however PS and PI have a significant role for the parts of the membrane with a negative charge [1]. The two fatty acyl chains may differ in the number of carbons that they contain (between 16 and 24) and degree of saturation (commonly 0, 1 or 2 double bonds). While a *trans*-bond does not alter the conformation of the tail, *cis*-bond inflicts a kink. In biological membranes, the PLs have mostly unsaturated hydrocarbon chains, except for SM which is often found with saturated ones. Fatty acyl chains combined with the variety of head groups, some of which are shown in Fig. 1-1B, result in existing of hundreds different PLs in cells.

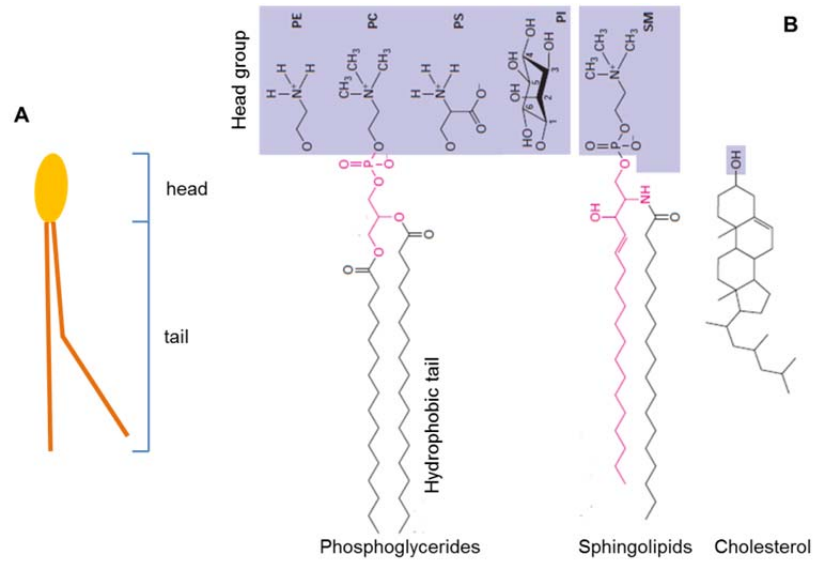

Fig.1-1. Structure of PLs and cholesterol. (A) Schematic sketch of a PL. (B) Important lipid types found in biological membranes. For phosphoglycerides and sphingolipids, glycerin and sphingosine provide the backbone (marked in red), respectively, to which the head and the tail groups are attached. The Figure is adapted with modifications from [2].

Another important component of the biological membranes is cholesterol (Fig. 1-1B). It contains four hydrocarbon rings providing a rigid structure. On one side of the rings, a small hydrophilic hydroxyl group is attached, on the other side a short lipophilic segment is found. Cholesterol typically increases the order of the fatty acyl chains which makes the bilayer thicker, typically stiffer, less water and ion permeable [3, 4]. However, it was shown that the effect of cholesterol is not universal, but rather depends on the type of lipid [5]. For instance, it does not change the rigidity of double unsaturated lipids, like dioleoylphosphatidylcholine (DOPC), while in saturated SM membranes the rigidity decreases with increasing the cholesterol content. In contrast, the cholesterol has a dual effect on the stiffness of saturated dipalmitoylphsphatidylcholine (DPPC) membranes. The rigidity of such membranes increases and reaches a maximum in the presence of a certain fraction of cholesterol (approximately until 25 %), whereas higher cholesterol amount causes a decrease in the membrane stiffness [6]. PLs and cholesterol are the main building blocks of the biological membranes. However, it should be noted that a variety of proteins and carbohydrates are embedded in the cell membranes.

The hydrophobic tails of the lipids cannot form hydrogen bonds with water molecules and thus exposing to water is energetically unfavorable. Therefore in an aqueous environment the lipids tend to organize in a way that the head groups hide the fatty acyl chains from the water. Hydrophobic attraction of the tails, although it is more an exclusion of the water than an attraction [7], together with the repulsion of the charged head groups actuates the self-assembly of PLs. Both forces determine the lipid solubility in water. The critical micelle concentration (CMC) of the lipids is in the range of 10^{-7} to 10^{-10} M [8]. The lipid shape is a crucial factor for the type of assemblies that lipids can form above the CMC [9, 10]. If the area occupied by the polar head is comparable with the one of the fatty acyl tails (cylindrical shape) the lipids typically organize in a single lamellar structure or so-called lipid bilayer

(Fig. 1-2A). In this case, the hydrophobic tails are exposed to the water at the edges of the bilayer. To avoid this, the bilayer forms closed spherical structures (vesicles), shown in Fig.1-2A (right). If the lipids are cone-shaped (smaller head), a hexagonal or cubic phase is preferred (Fig. 1-2B), whereas lipids with an inverted cone shape (usually with a single hydrocarbon chain) assembles in a micellar structure (Fig. 1-2C).

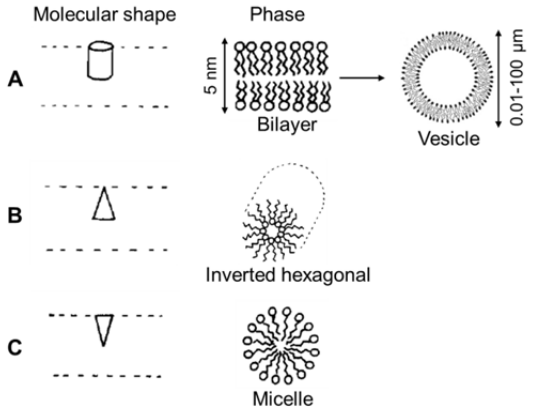

Fig.1-2. Lipid self-assembly determined by the shape of lipid molecules [11]. A, B and C correspond to lipids with a cylindrical, cone and inverted cone shape, respectively.

PCs, SMs and PIs favor the formation of the bilayer phase. Depending on the conditions, PEs and PSs tend to form either lamellar or inverted hexagonal phase [12]. However, the non-bilayer structures are important to many cellular processes e.g. membrane fusion [13]. We focus on lipid bilayers, which are the most common state of the biomembranes [14]. In the next paragraph we consider some model membrane systems.

1.2 Models of the cell membrane

Employing *in vivo* systems to study general properties of cellular membranes has several drawbacks. One has to work with complex systems in a physiological environment. In contrast, biomimetic model systems provide more flexibility. One can choose among large number of experimental parameters such as temperature, pH, buffer, type of lipids, etc. and can disentangle the contribution of individual species.

Variety of models, which mimic the cell membrane have been developed. Widely used among them are the following: vesicles, such as large unilamellar vesicles (LUVs) and giant unilamellar vesicles (GUVs), supported lipid bilayers (SBL), black lipid membranes (BLM). In addition, the computational simulations of lipid bilayers provide a multiscale description of the structure and dynamics of the membranes. Here, we would like to interject that monolayer model systems can provide an important knowledge about lipid structure, phases and interaction of various molecules [15, 16], however, lipids are not presented in a context of a bilayer. In addition, this model is restricted to the study of a planar lipid monolayers, thus it is not applicable for the study of curvature-related effects. Vesicles represent a well-established model system for exploring different aspects of bilayers. Depending on the preparation technique, they can differ in lamellarity and size. Of particular relevance are LUVs with size

50-1000 nm and GUVs, which are in the range between 1 and 100 μm. Due to their size, i.e. cell-size, GUVs are well visible under an optical microscope (see section 1.3.2), in contrast to LUVs, and this makes them a powerful tool to study membrane properties. The most used methods of preparation of GUVs are typically spontaneous swelling [17] or electroformation (Chapter 2.2) [18]. However, GUVs can be formed by fusion of small vesicles or from micellar lipid solution [19]. Critical biological processes in regard to cellular transport, exo- or endocytosis can be probed in GUVs [20]. Furthermore, a local heterogeneity (domains) even within the same phase, as a result of using only a few different lipids, can be visualized in GUVs [21, 22]. This will be discussed with more details in section 1.6. Separation of liquid phase, into domains with more ordered (l_o phase) and ones with more disordered (l_d phase) lipid configuration, is considered to mimic lipid rafts. These rafts are considered to be a small, short-living domains that sort certain membrane proteins (e. g. receptors) and influence their functionality [23]. However, the raft hypothesis remains quite controversial [24].

During the last decades computational modeling of lipid bilayers have become a well-established tool of investigations of membranes. Molecular dynamics (MD) or Monte Carlo (MC) provide an atomistic-level resolution with real-time, three-dimensional imaging of the system [25]. We used MD simulations to assess key properties of our system, see Chapter 3.2.4.

In the next section, we focus on general membrane properties and techniques to assess them in GUVs.

1.3 Membrane mechanical properties and morphologies. Techniques to study them in GUVs.

1.3.1 Mechanical properties of the bilayers and preferred vesicle shapes

Since the thickness (4-5 nm) of the phospholipid bilayer is much less than its length (scale of micrometers for GUVs and supported lipid bilayers) the bilayer may be viewed as an infinitely thin elastic sheet [26]. Mechanically, this sheet may be bent, sheared or dilated [27], see Fig. 1-3. However, this sheet approximation is inappropriate when the elastic model of vesicles shape known as area-difference elasticity model (ADE) is concerned. This model explicitly takes into account the fact that the membrane is a bilayer rather than a single sheet. The energy of all three deformations is captured in the following constants: bending rigidity, κ, shear elastic modulus, μ, and the stretching elasticity, K_a, (Fig. 1-3).

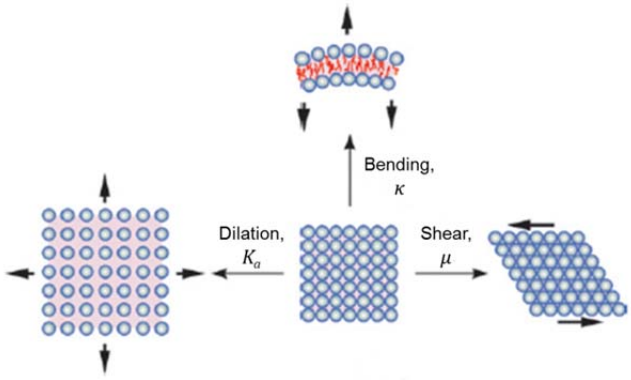

Fig.1-3. Essential material properties of phospholipid membranes: bending rigidity, shear elasticity and area compressibility modulus. Figure adapted from [27].

The forces needed to deform fluid membranes by shearing and bending are negligible compared with stretching deformations. However, in the case of fluid membranes μ = 0 [28], the shear modulus become significant when the membrane is in so-called 'gel' phase (insides about phase separation in GUVs and thus different phases are given in section 1.6 below) or attached to a polymer networking (simulating the cell cortex) [29]. Applying lateral force to the bilayer will expand (stretch) it along the direction of the force. The stretching elasticity of a liquid lipid bilayer is in the order of K_a = 240 mN/m [27].

If the area per molecule increase in the outer monolayer and decrease in the inner one the membrane will bent, in order to accommodate to this change. The bending rigidity of fluid bilayers is ~ 20 k_bT, where, k_b, is the Boltzmann constant and, T, the temperature, while for lipid bilayers in a gel phase and close to the melting point it is in the range of ~ 350 k_bT [27]. The bending rigidity sets the 'stiffness' of the membrane.

The sheet approximation allows the vesicle membrane to be considered as a closed two-dimensional surface in a three dimensional space. Such a surface can be locally described by its two radii of curvature R_1 and R_2 which determine the mean curvature, H, and the Gaussian curvature, K, see Fig. 1-4A [30], defined as

$$H \equiv \left(\frac{1}{R_1} + \frac{1}{R_2}\right) / 2 \tag{1}$$

and

$$K \equiv 1/(R_1 R_2) \tag{2}$$

Considering the entire membrane surface and assuming that the vesicle has a constant volume and area, one can describe the energy needed to deform a segment of membrane area (curvature energy) by the Helfrich Hamiltonian [28]

$$E_b = \int \frac{\kappa}{2} (2H - C_0)^2 + \kappa_g K dA \tag{3}$$

Where, A, is the surface area of the vesicle, κ, the bending rigidity, κ_g, Gaussian bending rigidity, C_0, spontaneous curvature and, H and K, the mean and the Gaussian curvature, respectively. The Gaussian bending rigidity is topological invariant which makes it difficult to

measure experimentally, in single component vesicles. However, κ_g is expected to be of the same order of magnitude as κ [30].

The spontaneous curvature reflects a possible asymmetry of the membrane. For instance, the membrane would curve in a preferred direction if lipids with different shape (intrinsic curvature of each lipid) are in the opposite leaflets or the number of molecules constituting each monolayer is different (Fig. 1-4B-D). The gradient of the lateral pressure, across the normal of the membrane, forms an intrinsic bending moment (Fig. 1-4B). Curving the membrane leads to release of the pressure (Fig. 1-4C). In addition, it should be noted that different chemical environment or asymmetric distribution of molecules, on both sides of the bilayer can be a source of spontaneous curvature as well.

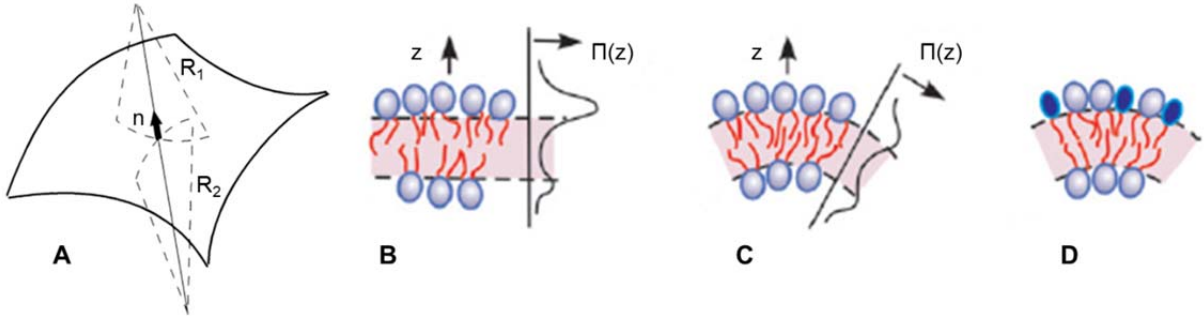

Fig.1-4. Membrane curvature. (A) Curvature of a sheet (2-D surface), adapted from [30]. (B-D) Membrane spontaneous curvature, resulting of difference in the number of molecules composing each monolayer (B-C) or asymmetrically integration of guest molecules (D) [27].

The difference in the number of lipids constituting both monolayers may deviate from one vesicle to another, depending on the preparation history. Therefore, every vesicle can have its own effective spontaneous curvature. This leads to a zoo of experimentally observable shapes, such as oblates, prolates, pears, stomatocytes, [31-33], see Fig. 1-5B. This zoo results also from the area-to-volume differences between the vesicles (reduced volume). In the absence of transbilayer lipid motion (flip-flops), which is relatively long (in order of hours), these shapes can be systemized into a morphological diagram (Fig. 1-5A) [34] according to the vesicle effective differential area, $\overline{\Delta\alpha_0}$, (the preferred curvature of a vesicle) and its reduced volume $\nu = \frac{3}{4}\,V/(\pi R_A{}^3)$, where $R_A = (A/4\pi)^{1/2}$. The latter is a convenient way of characterizing the excess vesicle area. The effective differential area describes the overall tendency of the membrane to curve. It is defined by a dimensionless combination of the spontaneous curvature and the preferred area difference between the inner and the outer monolayer. In our experiments (described in Chapter 3), we observed crossing of the $D^{pro/pear}$ and L^{pear} lines, both indicated in Fig. 1-5A. The $D^{pro/pear}$ line represents the border where prolate, symmetric shapes deform in a way such that the mirror symmetry is broken, and the vesicles attain pear-like shapes. 'D' stands for 'discontinuous' and denotes a first-order transition. L^{pear} is the pear-limiting curve, above which budding-like shape (where two spheres of different radii are connected by an ideal neck) is presented.

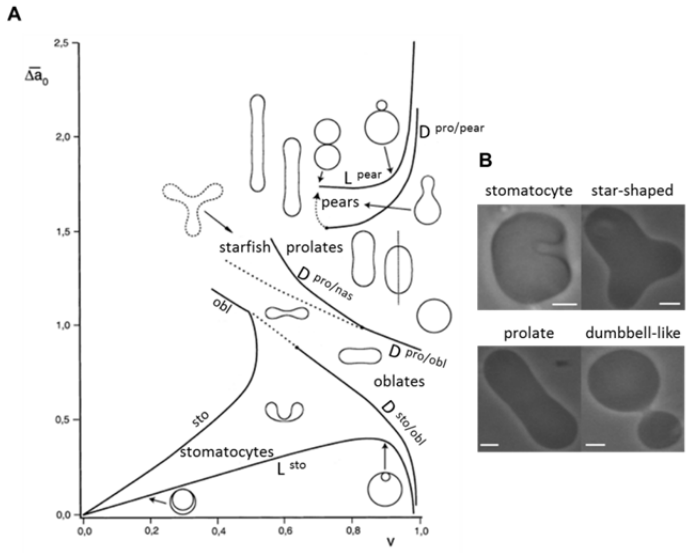

Fig.1-5. Morphology of GUVs. (A) Vesicle morphology diagram with respect to the effective differential area and reduced volume of a vesicle (described in the text), from [34]. B) Different vesicle shapes captured under phase-contrast microscopy illustrating a number of different morphologies as shown in the morphological diagram in (A). Scale bars correspond to 5 µm.

1.3.2 Techniques to study membrane material properties employing GUVs

Observing the GUVs

The membrane material properties discussed in the previous section can be assessed by observing GUVs with optical microscopes. Throughout this work we used mainly two microscopic techniques: i) phase-contrast and ii) fluorescence microscopy. The GUVs are prepared in sucrose and diluted in glucose (or vice versa) to ensure asymmetry across the bilayer. These different media, in- and outside the vesicle, have different refractive indices. Thus, the phase of a light shifts when the light travels through such environment. These small shifts are converted into different contrast in the field of view by interference between scattered and background beams. Hence, under phase-contrast microscopy the GUVs look darker on a light background (Fig. 1-6A).

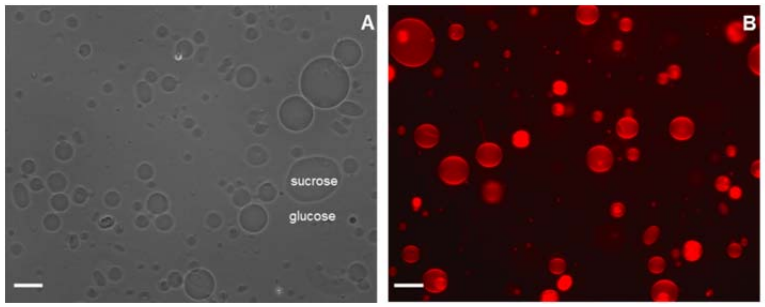

Fig.1-6. Images of GUVs taken with (A) phase-contrast and (B) fluorescence microscopy. The scale bars correspond to 30 µm

While this technique does not require staining of the sample, fluorescence microscopy (as the name itself prompts) uses fluorescent dyes in the membrane. Fluorescently labeled GUVs are shown in Fig. 1-6B. The dyes are molecules that after absorption of a photon of high energy

(short wavelength), emit a photon with lower energy (longer wavelength). Typical light sources are mercury lamps. The light passes through excitation and emission filters.

Epifluorescence microscopy is characterized by high signal-to-noise ratio, since only the emitted light together with the reflected excitatory one reaches the objective lens. More complex fluorescence microscopy technique is confocal microscopy. It offers several advantages over wide-field illumination microscopy. The light sources in confocal microscopy are usually lasers. They generate a higher photon flux than mercury lamps with filters and use point-like instead of wide-field illumination. Thus, additional information away from the focal plane is highly reduced leading to increase in the resolution. Then, it is not surprising that confocal microscopy in combination with other methods is a powerful tool to study GUVs [35-37]. Here, we used confocal microscopy in combination with FRAP (fluorescence recovery after photobleaching) to probe diffusion coefficients of lipids in different phases (see Chapter 4.2.3). This technique will be described in Chapter 2.5.

Measuring the elastic properties of membranes

Bending rigidity of membranes can be extracted from the thermal fluctuations that a vesicle experiences in a certain period of time [38]. For this purpose, a large number (typically more than 1000) of phase-contrast snapshots, of a fluctuating GUV have to be taken. By tracing the contour of the vesicle one can extract the mean square amplitudes of the fluctuations. The latter provides the mode number dependence of the bending modulus of a vesicle [39]. Data of middle-wavenumber modes (3-15) are considered in the analysis. Due to the optical resolution of the system noise is predominant in the higher wavenumber modes, while tension dominates in the case of low wavenumbers. We applied this approach, introduced in [5], to measure and compare the bending modulus of two different systems (Chapter 4.2.4).

A variety of membrane material properties have been studied when GUVs are exposed to electric fields. [40, 41]. Strong electric pulses can induce electroporation (rupture of the membrane) when a critical transmembrane potential is reached. When the electric field is switched off, the vesicle returns back to its initial shape. One can use the relaxation dynamics to examine the membrane dilatational viscosity in absence of poration or the membrane edge tension when a pore exists [42, 43]. Of particular relevance is the case when GUVs are exposed to a weak alternating electric (AC) field, resulting in vesicle deformation. The latter is associated with flattering of the membrane fluctuations due to accumulation of opposite charges at both sides of the membrane [44]. Thus, the area stored in the thermal fluctuations is pulled to afford the deformation and one can measure the whole vesicle area, a small part of which is hidden in the fluctuations (see Chapter 3.2.6).

Now let's turn our focus to biological processes, which require changing of the cell membrane morphology, discussed in the next part.

1.4 Cell membrane and different membrane shapes existing in nature

The hydrophobic core of the lipid bilayer of the cell (plasma) membrane acts as a permeability barrier that prevents the entry of unwanted materials in the cells and the exit of

needed metabolites. Also the membrane divides the eukaryotic cells into smaller subcompartments termed organelles, providing different 'working stations'. This simple barrier function is modulated by the presence of membrane proteins. The latter ensure the passage of nutrients into the cells (cytosol) and the organelles, and metabolic wastes out of them. Other proteins function to maintain the proper ionic composition of the cytosol. Beside its primary function, to serve as semi-permeable barrier, the cell membrane is a place for biochemical processes, cell-cell signaling and adhesion. The structure of the plasma membranes (Fig. 1-7) is supplemented by carbohydrates, important for the recognition of other molecules during signaling cascades, and supporting cytoskeleton filaments.

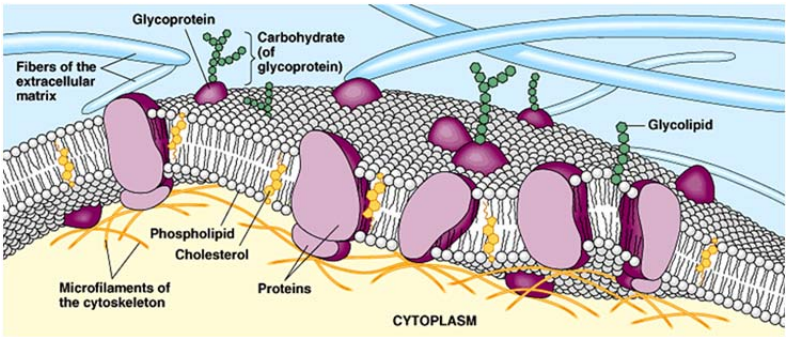

Fig.1-7. Schematic drawing of eukaryotic plasma membrane containing the essential features. Image taken from Pearson education, Inc.

Lipid composition, surface charge, amount of proteins and cholesterol may vary between different cellular membranes. Depending on the cell properties and function, different membranes, or even leaflets of a single membrane, can be selectively enriched with certain lipids. Disorders in this lipid sorting lead to developing of number of diseases [45]. Membranes from different cell types and organelles exhibit variety of shapes which complement a cell function. The shape of erythrocytes (Fig. 1-8A) allows them to squeeze through narrow blood capillaries. Another example for a functional role of a specific morphology of membranes is the inner membrane of mitochondria (Fig. 1-8B). Its curvature was found to sort membrane components [46].

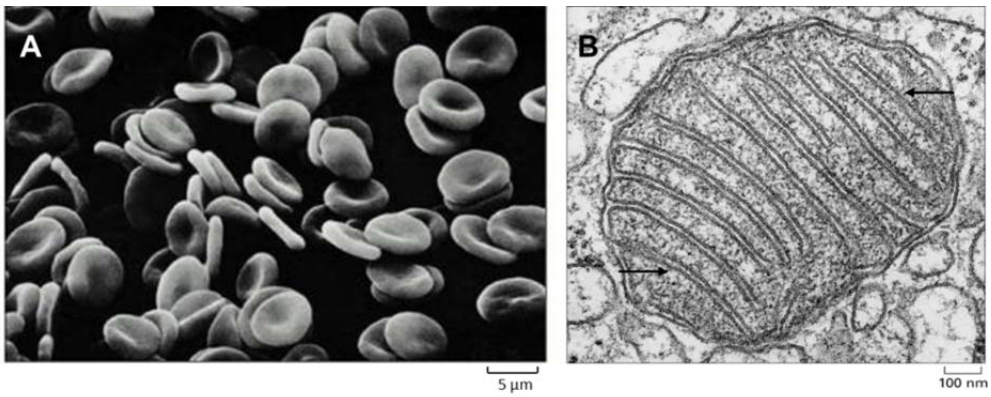

Fig.1-8. Membrane shapes in cells and organelles. (A) Erythrocytes with their typical oval biconcave shape. (B) Transmission electron micrograph of a mitochondrion. The two arrows on both sides of the mitochondrion point parts of the highly curved inner membrane. Pictures from [47].

Transport of crucial biomolecules, like proteins, occurs within (among cell organelles) and between the cells. This traffic of molecules is mediated by transport vesicles. They arise and separate from the membrane of one compartment, and deliver their cargo to the next compartment by fusing with the membrane of that compartment. The budding of vesicles, as well as their pinching off from the 'parent' membrane, and the eventual fusion with the 'target' membrane are driven by different protein complexes [48, 49]. The process of secretion of transport vesicles is known as exocytosis, whereas the opposite one (uptake inwards in the cell/organelle) is called endocytosis. Endo- and exocytosis are of central importance to signal transduction and neurotransmission. It should be noted that not only beneficial to the cells structures can be transported in the cytosol. For example, viruses and bacteria may invade in the cells via endocytosis [50, 51]. Thus, vesicular transport is essential to eukaryotic life.

As one can assume, the cytotic processes 'produce' changes in the membrane morphology (curvature). Fig. 1-9 shows exo- and endocytotic events. In both cases, the steps of the vesicular transport have a common theme. One can notice structures that exhibit discrete regions of the membrane with a high curvature. Such structures, usually called vesicle buds, appear to be an intermediate step before the completed vesicle pinches off from the membrane.

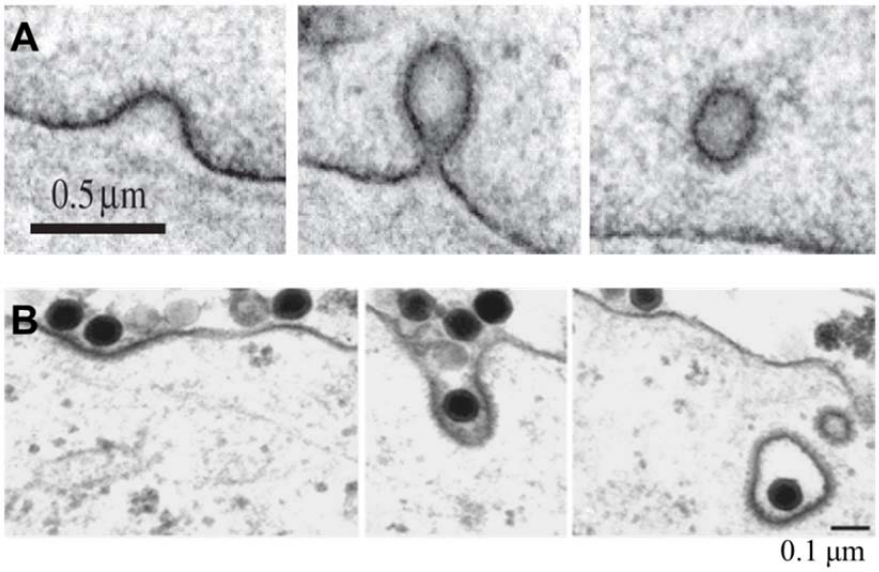

Fig.1-9. Transmission electron micrographs of different stages during (A) exocytosis and (B) endocytosis. Pictures adapted from [52, 53]

Part of this work examines the budding process in model membrane systems (Chapter 3) but before taking a step in this direction, we would like to draw the attention to some models for studying membrane morphologies.

1.5 The role of light in biomimetic models of membrane shape transformations

1.5.1 External stimuli which cause changes in the GUV shape

As mentioned in section 1.2, GUVs are a simple model of cellular membranes in a cell-size scale. The complex content of the plasma membrane is reduced only to a phospholipid bilayer composed of a single (or few) lipid type(s). The general mechanical and surface properties of the cell membrane are conserved by the lipid bilayer. Pure lipid bilayers allow to ignore the membrane complexity and focusing on the physical factors that are involved in certain cellular processes. Hence, one can use GUVs to study membrane characteristics and to mimic cytological processes of cell membranes. A number of studies investigating vesicle shape morphologies have been done, see for example [54, 55]. Initially, the GUVs have a spherical shape (if there are no defects). In order to cause shape transformations one has to change one or several factors of the external conditions. Passive permeation of charged and neutral molecules through the membrane is strongly hindered [56]. As a result, gradients of osmotic pressure, pH or ionic strength can be generated between the both sides of the bilayer. Such concentration gradients can become a source of external perturbations driving membrane deformations. For example, osmotically induced water efflux from the vesicle interior gives rise to morphological transformations in GUVs [57, 58]. In the same vain, a gradient of proton concentration across the vesicular membrane can neutralize the negatively charged lipids and thus, cause a decrease in the electrostatic repulsion between the head groups. The latter decreases the effective area of the lipids and generates an area asymmetry. Therefore, low pH in the vesicle exterior or interior can lead to inward invagination or outward budding [59]. Also, temperature changes can induce transitions of different vesicle shapes. An increase in temperature leads to expansion of the outer monolayer with respect to the inner one and thus to positive spontaneous curvature, which results in expelling of a bud [58, 60].

Throughout this work we used light as an external stimulus to trigger shape transformations in GUVs. An increasing attention is paid to this approach because light offers the supply of energy without contact with the sample or altering the chemical environment. In fact, light and GUVs have been used to investigate light receptors [61], response of the membrane to oxidative stress (including photodynamic therapy) [62] or in the field of liposome-based drug delivery [63, 64]. Much could be said about the variety of studies coupling light with GUVs but of particular concerns here are biomimetic models of cytotic processes.

1.5.2 Light and photosensitive molecules

One major advantage of light is that it offers high temporal and spatial control. One can direct the light beam and thus irradiate only part of the sample for a certain time. Moreover, use of photosensitive molecules contributes for more precise spatiotemporal control. To be effective, the photosensitive molecules should meet some requirements, the following of which are most important: i) a low light dosage to cause an event, ii) the molecule response to light must be strong enough to alter and thus lead to substantial change in the studied object and iii) the

molecules should remain stable in the experimental conditions, after the irradiation. One type of photosensitive molecules used for biological studies are molecules with a 'caging' group [65]. An essential functional group is protected by a light-sensitive protecting group ('caging' group), which makes the molecule inactive until the caging group is removed. Once uncaged, the molecule remains active. In contrast, another type of photosensitive molecules called 'photoswitches,' can undergo reversible changes such that many rounds of active/inactive states can be achieved. An example for a response of photoswitches to light is opening/closing of a ring from the structure of a molecule or isomerization of the photoswitch (changing of the molecule conformation) [66, 67]. Of particular interest are the molecules with the ability to photoisomerize, specifically azobenzene-based molecules.

Azobenzene is one of the most well characterized photoswitches [68]. Fig. 1-10 shows the absorption spectra and the structure of the azobenzene isomers. *trans*-Azobenzene exhibits a strong $\pi \rightarrow \pi^*$ band at 320 nm and a weak $n \rightarrow \pi^*$ transition around 440 nm. In comparison, the *cis* isomer shows two $\pi \rightarrow \pi^*$ transitions at 250 nm and 280 nm, due to a higher π^*-orbital energy level than in the *trans* isomer, and a higher wavelength band near 440 nm. However, the n-energy level is also higher compared to the one of the *trans* isomer, resulting in very similar net $n \rightarrow \pi^*$ energies for both isomers [69].

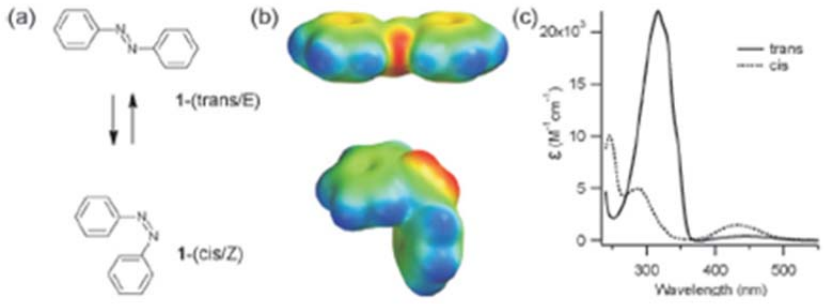

Fig.1-10. (a) Structure of azobenzene's *trans* and *cis* isomers. (b) Spacefilling models of both conformations. The blue parts correspond to a positive electrostatic potential, while the red color indicate negative values. (c) Absorption spectra of the isomers. The figure is taken from [70].

Since the *trans* isomer is more stable (with ~45 kJ mol^{-1}) than the *cis* one, it is not surprising that at equilibrium conditions (in dark) more than 99 % of the molecules are in *trans* conformation [71]. A large amount of the *cis* isomer can be produced by UV irradiation in the range of 300-350 nm (Fig. 1-10c). The *cis* isomer is characterized with more bent conformation compared to the *trans*. In addition to the geometrical changes, the length of each isomer also differs. The distance between the carbon atoms at *para* positions of the rings changes by ~3.5 Å [69]. The *trans* isomer can be regenerated by irradiation at ~ 450 nm.

An abundant number of azobenzene derivatives have been developed through the years, depending on the question of study. For instance, if the final aim involves implementation of the azobenzene derivate *in vivo* (for example as a trigger for a drug release in a drug delivery system) then the wavelength of isomerization must be biocompatible. Unmodified azobenzene

isomerizes in the UV region. Since UV light can cause damages in biomolecules in the cell (e.g. DNA), shifting the absorption wavelength towards the red region may be necessary.

It has been shown that light and azobenzene derivatives represent a convenient tool to modify biological systems [72]. Now the question is whether one can use GUVs, light and azobenzenes in order to mimic cellular processes such as exo- and endocytosis in a reversible, controlled way. Indeed, a large body of work in that direction has been reported some of which presented in the introduction of Chapter 3.

In this study we used an azobenzene derivate molecule (F-azo), which completely isomerize in the visible spectra (green light for the *trans*-to-*cis*, blue light for the reverse isomerization), i.e. without the need to apply damaging UV irradiation [73] (Fig. 1-11). The latter is achieved by introduction of four fluorine atoms *ortho* to the azo moiety. These fluorine atoms reduce the electron density near the azo bond and thus separate the n→ π* transitions of *trans* and *cis* isomers. Therefore, light in the visible range can be used to switch both conformations selectively.

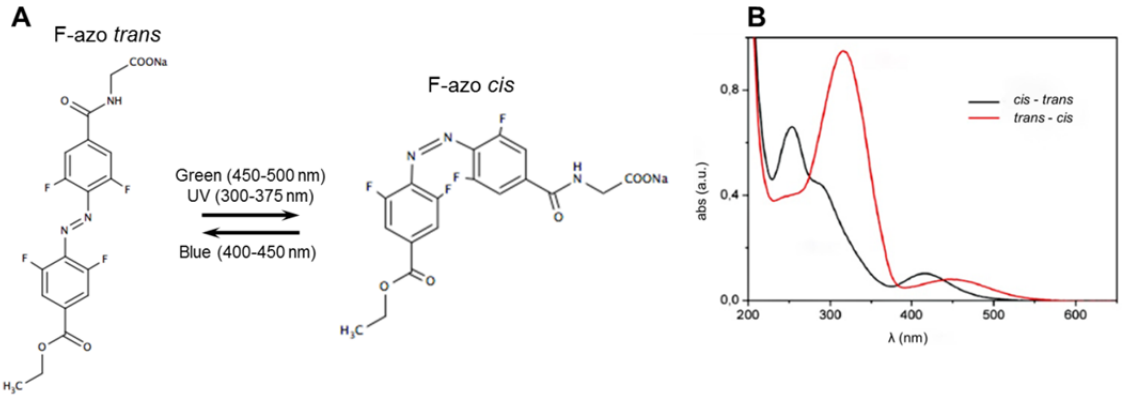

Fig.1-11. (A) Molecular structure of F-azo in both *trans* and *cis* conformation. (B) Absorption spectra of F-azo, adapted from [73]. *trans-to-cis* Photoisomerization takes place in the range between 300-350 nm or 450-500 nm, while *cis-to-trans* conformational change occurs in the range between 410-440 nm.

1.6 Multicomponent lipid bilayers

In this section we will review membrane model systems, particularly GUVs, which are composed not only by a single type of lipid but have a multi-lipid contexture. First, let's look at some aspects of single-component lipid bilayers. The latter can be either in a liquid (L_α) or gel-like (solid) state (L_β). The L_α state is characterized by a thinner bilayer thickness and larger area pre lipid compared to those of the L_β phase [74]. The shear surface viscosity of the L_α phase decreases by three orders of magnitude and the bending rigidity by one order of magnitude in contrast to the L_β phase [27]. In addition, the lipid mobility in the L_α phase is distinguished by faster diffusion times (~ 3 x 10^{-8} cm^2/sec) [75] compared to that in the L_β phase (on the order of 10^{-11} cm^2/sec). The phase state depends on the melting temperature T_m of the lipid's fatty acyl chains. For example, at temperature below T_m (i.e. in the L_β phase) the lipids are highly ordered, with acyl chains oriented perpendicular to the plane of the membrane (Fig. 1.12, left panel), forming a gel phase. In this state the lipid chains are fully extended, tightly packed and subjected to relatively little motion. Above T_m the acyl chains

undergo much more motion with rotations around the C-C acyl chain bonds and bending of the chains.

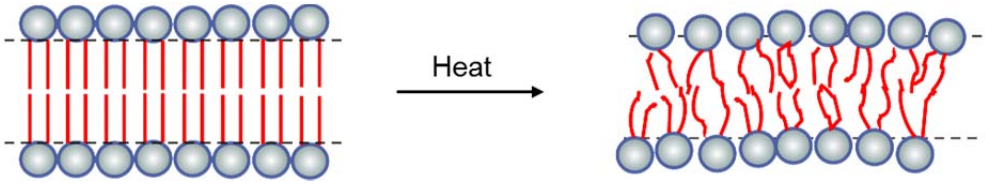

Fig.1-12. Schematic drawing of the gel (left) and fluid (right) state of the phospholipid bilayer. Increase in the temperature causes a transition from gel to fluid phase.

Long, saturated chains have the greatest tendency to aggregate, packing tightly together into a L_β state. PLs with short fatty acyl chains, which have less surface area for interaction, form more fluid bilayers. Likewise, the kinks in unsaturated fatty acyl chains result in their less stable interactions with each other than do saturated chains and hence more fluid bilayers. When a highly ordered, gel-like bilayer is heated, the increased molecular motions of the fatty acyl tails cause it to undergo a transition to a more fluid state (Fig. 1-12, right panel).

Addition of cholesterol to a saturated lipid (e.g. DPPC, SM) alone results in a more complex phase behavior. The cholesterol effect on the PLs chains order (and thus on the bilayer phase) depends on its concentration and the temperature conditions [76]. The bilayer of DPPC membranes is in gel phase, at cholesterol concentrations below 20-25 mol% and temperature lower than T_m. In contrast, when the amount of cholesterol is above 20-25 mol% its rigid structure disturbs the order of phospholipids in gel phase and a liquid sub phase known as liquid ordered phase (l_o) prevails. The l_o phase has similar properties as the liquid phase formed by low T_m unsaturated lipids such as DOPC, termed liquid disordered, l_d, phase, but the lipid tails exhibit more ordered configuration rather compatible to the one of a gel membrane.

Mixtures of saturated and unsaturated lipids and cholesterol (ternary mixtures) can either mix homogeneously or separate into different phases. In the latter case at least three possible phases can exist: a gel phase, rich in saturated lipids, a l_o phase, rich in saturated lipids and cholesterol and a l_d phase, rich in unsaturated lipids [21]. The Gibbs phase rule defines the number of phases that can coexist for a given number of components. This phase rule gives the degrees of freedom, *F*, of a system in equilibrium:

$$F = N - P + 2 \tag{4}$$

Where, *N*, is the number of components and, *P*, the number of phases. In a tree-component system with fixed composition, in which temperature and pressure are variables ($F = 2$), three phases can coexist. For example, an existence of gel, liquid ordered and liquid disordered phase can occur simultaneously. The process of reaching the coexistence of different states is usually called phase separation. It should be noted that above a certain critical temperature the components of the lipid mixture will become fully miscible. GUVs made of ternary lipid mixtures with a certain composition can capture a region with l_o and l_d phases forming

optically resolvable domains on the same vesicle [77]. Most membrane dyes used in fluorescence microscopy preferentially partition in one phase over the other. Thus, one can visualize the formed domains. The domains occur by nucleation mechanism. First, small aggregates (nuclei) are formed. Since the domains are liquid (l_d and l_o phase) they can fuse and grow over time, eventually reaching equilibrated state (Fig. 1-13). The morphology of the domains depends on their phase. Solid domains tend to form cylindrical segments or facets, whereas fluid domains are spherical [77]. The line tension at the interface between the domains influences the domain shape and size. The line tension is isotropic, and hence the equilibrium shape of the domains is circular. For solid-like domains the line tension becomes anisotropic, and the domains are no longer circular. At the critical point, where two phases become indistinguishable, the line tension is negligible. Membrane domains are considered to be relevant to the rafts in biological membranes [78].

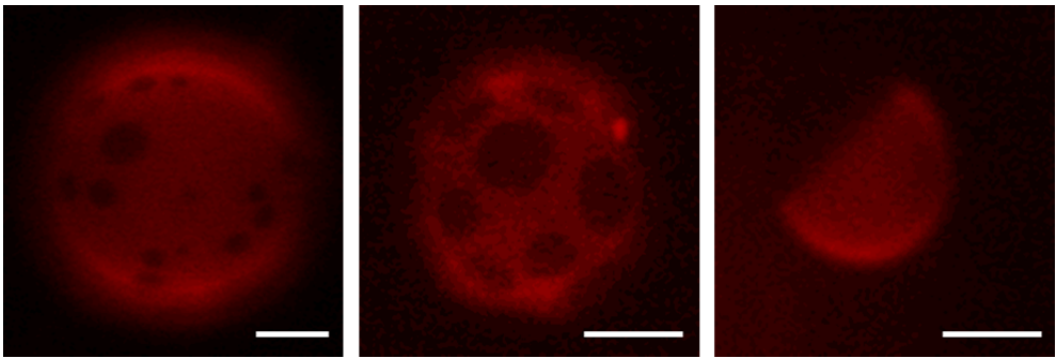

Fig.1-13. Domains in l_d (red) and l_o (dark) phase in phase separated GUVs made of DPPC:DOPC:Chol, in molar ratio 1:1:1. All pictures were taken at room temperature (23°C). The first vesicle (from left to right) has small l_o domains, while the second one shows a bigger l_o area. The third picture shows a GUV with equilibrated phases. The scale bars correspond to 10 µm.

The phase behavior of a lipid system can be graphically represented on a phase diagram. The phase diagram of a ternary system is known as a Gibbs triangle. The latter gives information about the stable phases for different compositions at a certain temperature. A number of phase diagrams have been determined and l_o-l_d phase separation was observed for a broad range of lipid compositions [79]. Fig. 1-14 shows the Gibbs triangle for a system consisting of DOPC (low melting lipid), DPPC (high melting lipid) and cholesterol [80]. Each of the tree components of the system is found at the corners of the triangle, where their corresponding mole fraction is 100%. For example, the corner where DOPC is labeled corresponds to 100 % of the DOPC mole fraction, whereas at the base of the triangle opposite that corner the mole fraction of DOPC is 0. The phases observed in this ternary mixture are outlined at panel *a* (Fig. 1-14). It should be noted that this panel contains information about more than one temperature. At temperature lower than the T_m of DPPC, four outcomes are possible, depending on the lipid composition. The GUVs can exhibit one uniform liquid phase as in region B. This occurs when vesicles contain greater than 50% Chol, a large fraction of unsaturated lipid (DOPC) or contain binary mixtures of DPPC and Chol as shown in micrographs 2 and 3. In region C (a large fraction of DPPC), the vesicles are in solid state. Increase in DOPC concentration (going to left on the DPPC-DOPC axis) leads to solid-liquid

coexistence, (region D). A typical phase-separated vesicle from D is shown in micrograph 1. The l_d-l_o coexistence region is enclosed in region E. It is also possible that a three-phase coexistence (l_d-l_o-L_β) occurs between D and E [81]. Fig.1-14 *b* shows a liquid-liquid coexistence region at a constant temperature. The morphology of the domains (micrographs 4-8) is different compared to the solid domains in micrograph 1, which are noncircular.

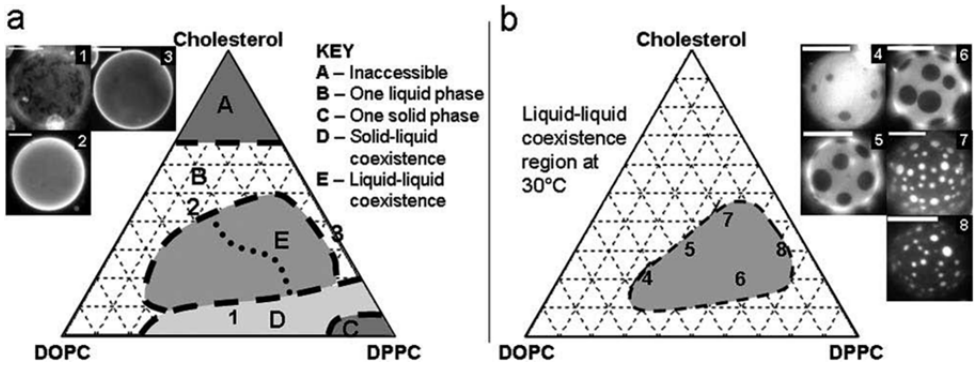

Fig.1-14. Gibbs phase triangle for a DPPC-DOPC-Chol lipid mixture. (a) Phase-separated regions observed in GUVs. The dotted line in region E represents the compositions at which the area of l_d and l_o domains is roughly equal. (b) A phase diagram of liquid immiscibility region observed in GUVs at 30°. All scale bars correspond to 20 µm. The compositions of the vesicles in micrographs 1-8 are pointed (the corresponding numbers) on the Gibbs triangles. The figure is taken from [80].

The stability of a phase is determined by the Gibbs free energy. It is interesting to note that the typical interaction energies between lipids are in the range of -3 and 2 k_bT [82]. Therefore, changing the temperature by a few degrees, adsorption of proteins or even presence of impurities can alter the membrane phase state.[83-85]. We investigated the influence of F-azo isomerization on phase separated GUVs (see Chapter 4).

In the last section of the introduction (below) we will advert key fundamentals of a computer simulation method, which we used to complement the experimental work.

1.7 Molecular dynamic simulations of phospholipid bilayers

Simulations can be used to track the behavior of individual atoms with the potential to provide a much more detailed picture of the examined system than can be obtained experimentally. In principal, molecular dynamics (MD) is a computer simulation approach that solves the classical Newton's equations of motion for a set of molecules, in order to obtain the trajectory of the system for a short period of time (tens to hundreds of nanoseconds) [86]. Non-bonded (van der Waals, electrostatic) and bonded (to keep the geometry of a covalent bond) interactions describe the model on which the MD simulations are based. Well-known pair potential for van der Waals systems is the Lenard-Jones potential, U_{LJ},

$$U_{LJ} = 4\,\varepsilon\left[\left(\frac{\sigma}{r}\right)^{12} - \left(\frac{\sigma}{r}\right)^{6}\right] \tag{5}$$

Where, ε, is the depth of the potential (governs the strength of the interaction), r, is the distance between the particles and σ, is the distance at which the inner particle potential is

zero. This potential is strongly repulsive at short r, while attractive forces dominate at large distances.

MD have been used to study a variety of biomolecular systems, including proteins, nucleotides and lipid bilayers [87-89]. Here, we focus on MD simulations for exploring phospholipid bilayers. The force field is crucial for the correct description of the system. In a nutshell, a force field is a set of parameters that characterize the interactions between atoms or particles (which build the investigated system) and describe the potential energy of the system [90]. In MD, various force fields with different levels of detail can be used. Fig. 1-15 shows some of these models, which represent a single lipid (DOPC) with different levels of detail. Force fields in which all atoms are explicitly simulated are known as 'all-atom' force fields (Fig. 1-15A). Two of the most widely used all-atom force fields are AMBER and CHARMM [91, 92] The all-atom model is one of the most accurate models, however, simulating all-atom lipids is computationally expensive. In order to decrease the computational demand, one can reduce the number of simulated particles, and thus to simplify the force field of the system. To do so, different atoms can be introduced together in one interaction site. For instance, the united-atom models (Fig. 1-15B), based on GROMOS force field [93], combine each aliphatic carbon and associated hydrogens into a single particle. Larger molecular units (such as multiple carbon atoms) are implemented in coarse-grained force fields (Fig. 1-15C). Well-known coarse-grained models are the generic model of Lipowsky et al. [94, 95] and the specific model of Marrink (MARTINI model) [96]. In this work, we use all-atom model with Lenard-Jones potential, see Chapter 3.1.5.

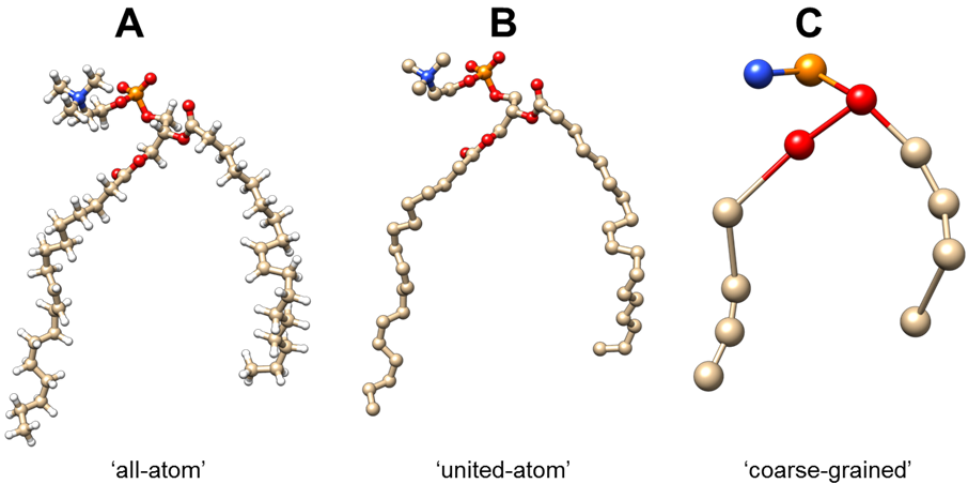

Fig.1-15. MD modelling of DOPC in different levels of detail. Carbon atoms are shown in beige, oxygen in red, nitrogen in blue and phosphorus in orange. The hydrogens in panel A are represented in white.

2 Methods

Molecules and a basic description of the methods used through this work are introduced in this chapter. Specific parameters of the measurements are stated in the corresponding chapters.

2.1 Molecules

The GUVs were prepared from commercially available phospholipids. The lipids 1,2-dioleoyl-sn-glycero-3-phosphocholine (DOPC), 1,2-dipalmitoyl-sn-glycero-3-phosphocholine (DPPC), as well as the fluorescent probe, 1,2-dipalmitoyl-sn-glycero-3-phosphoethanolamine-N-(lissamine rhodamine B sulfonyl) (DPPE-Rh) and cholesterol were purchased from Avanti Polar Lipids (Alabaster, Al). All lipids are dissolved in chloroform and stored at -21°C.

For the experiments involving morphological changes in GUVs (Chapter 3) the vesicles were composed only from DOPC, while for the study of phase-separated vesicles (Chapter 4) three-component lipid system (DOPC, DPPC and cholesterol) was used. We have chosen this system for the following reasons: i) DOPC and DPPC share the same head group and thus the same symmetry, ii) immiscible liquid phases are observed over a wide range of compositions [80]. Particulars of the used lipid mixtures are given in Chapter 4.1. Fig. 2-1 shows the chemical structures of the listed molecules. DOPC has one double bond in each fatty acyl chain and it is in a liquid phase above -22°C. In comparison, the melting temperature of DPPC (saturated lipid) is 41°C and therefore the lipid is in solid phase at room temperature. Due to the difference in the melting temperature of both lipids, a miscibility gap occurs below 41°C when the lipid mixtures contain DOPC and DPPC, (see Chapter 1.6). Since the DPPE-Rh partitions in the l_d phase in coexistence of l_d-l_o phase, we used this dye to label the l_d phase.

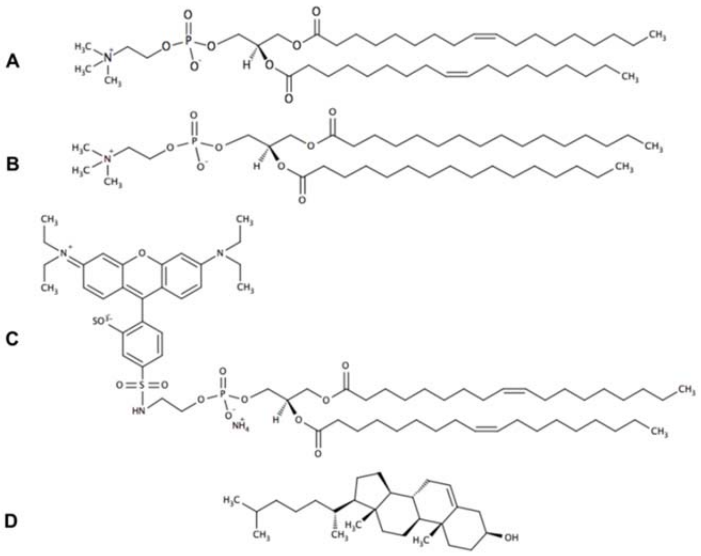

Fig.2-1. Structure of the used lipids. (A) and (B) correspond to DOPC and DPPC, respectively. (C) The fluorescent dye rhodamine attached to DPPE forms the fluorescent probe (DPPE-Rh). The molecular structure of cholesterol is shown in (D).

The photosensitive molecule, o-tetrafluoroazobenzene (F-azo), see Fig. 1-11 in Chapter 1.5.2, was provided by D. Bleger from Humboldt University. The synthesis and chemical characteristics are described in [73] and were briefly discussed in Chapter 1.5.2.

In order to visualize the GUVs under phase-contrast microscopy we used different sugars inside (sucrose) and outside (glucose) of the vesicles. The sugar asymmetry creates differences in the refractive index between the vesicle interior and exterior, and thus enhances the vesicle contrast when the GUVs are observed with phase-contrast microscopy. The sucrose and D-glucose were bought from Sigma Aldrich (St. Louis, MO). For the vesicle electrodeformation experiments a higher conductivity (attained by the presence of salt) of the solution enclosed in the GUVs is needed in order to achieve a prolate vesicle deformation (see section 2.4 below). We used sodium chloride purchased from Roth (Karlsruhe, Germany). All aqueous solutions were made with use of Milli-Q water.

2.2 Preparation of vesicles

GUVs were prepared applying the electroformation method [18]. The procedure can vary depending on the aim of the experiment, but the main steps are the following. Lipids usually dissolved in pure chloroform are spread on platinum electrodes or glass surface covered with indium thin oxide (ITO). In this work, we used ITO-coated glasses (resistance ~ 20 Ω^2). The lipids are spread on the conductive surface of the glasses and the latter are kept in low pressure conditions at room temperature for several hours, during which the chloroform is evaporated. The conductive glasses are placed together, separated by a spacer and thus forming a chamber. The lipid film is hydrated by an aqueous solution, introduced in the swelling chamber (Fig. 2-2), followed by application of an AC field.

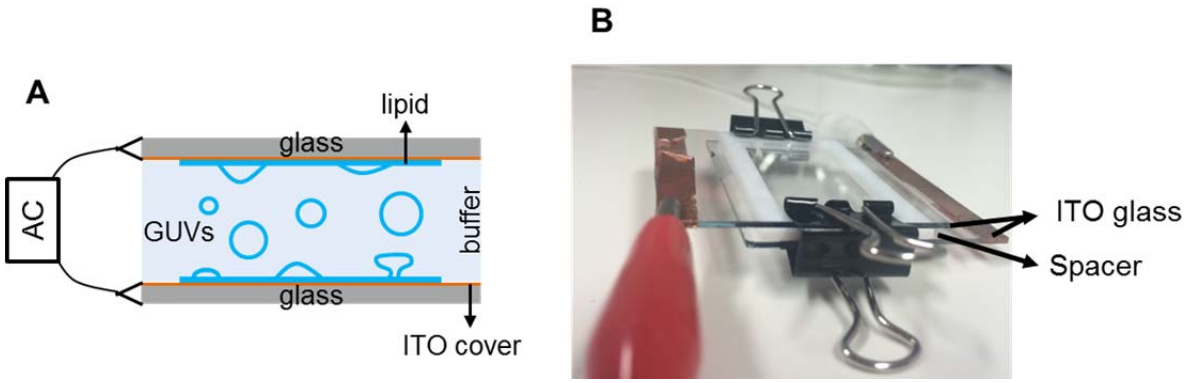

Fig.2-2. Electroformation of GUVs. (A) Sketch of the electroswelling process. (B) Electroformation chamber connected to a function generator via wires (the red and white clips in the corners).

The electric field induces swelling of the lipid film and further separation from the substrate. The vesicles are heterogeneous in size (5-100 μm) and often with defects (e. g. internal structures, tubes). Ideally, the best vesicles are unilamellar without defects. In this work the GUVs growing and diluting solutions were solutions of sucrose and glucose (the solutions are adjusted to be isotonic). Vesicles grown in the presence of sucrose and diluted in glucose are heavy and sediment on the bottom of the observing chamber, vice versa GUVs formed in the

presence of glucose and diluted in sucrose are light and sediment on the top of the microscope slide.

LUVs can be prepared by a technique called extrusion. Multilamellar vesicles are formed by hydration of a dried lipid film. The suspension of the multilamellar vesicles is forced (via applying a high pressure) to pass through a filter with pores, with well-defined size. Repeated pushes of the vesicle dispersion through the filter decrease the lamellarity of the vesicles. After a number of cycles (usually above 20) vesicles with unilamellar lipid bilayer are obtained. Here, as with the electroformation, not all vesicles are with the same size but the mean diameter of the LUVs is near the filter's pore size.

2.3 Vesicle observation

In the present work, we visualized the GUVs using both phase-contrast and epifluorescence microscopy. It has been addressed in the introduction (Chapter 1.3.2) that phase-contrast microscopy is a technique based on influences on the optical path of light, which enhances the contrast of colorless and transparent objects. The light passing through a specimen travels slower and it is shifted compared to the uninfluenced light. However, this phase difference is not visible for the human eye. In the phase-contrast microscope, the phase shift is converted into an intensity difference by a system of semi-transparent rings (Fig. 2-3A). The specimen is illuminated by the light coming through a ring, called a condenser annulus. The diffracted as well as the undiffracted light is collected by the objective lens. A phase plate is placed at the back side of the objective lens. This plate increases the phase of the undiffracted light by $\lambda/4$ and decreases that of diffracted light by $\lambda/4$ as shown in Fig. 2-3A. A total phase difference of $\lambda/2$ is therefore obtained between the diffracted and the undiffracted light beams before they are focused on the image plane. The two waves, that have $\lambda/2$ phase difference, interfere destructively, thereby diminishing the light intensity. Any phase change caused by the specimen is therefore converted into an amplitude signal by a phase-contrast microscope, resulting in increasing the contrast.

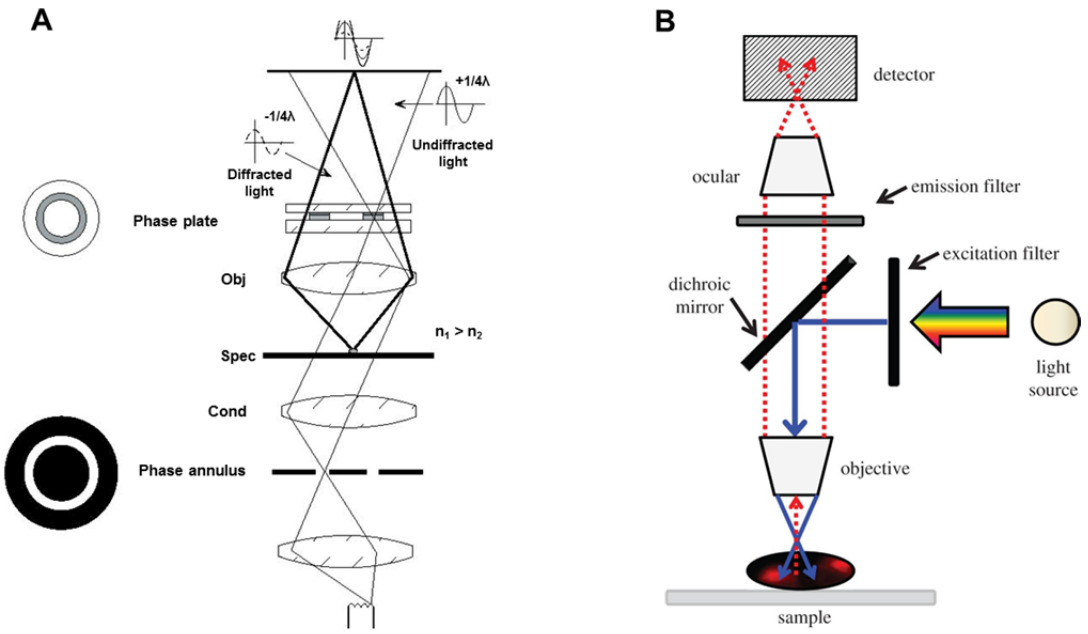

Fig.2-3. Simplified scheme of the optical path of a phase-contrast (A) and epifluorescence microscope (B). The pictures are adapted from [97] and [98], respectively.

In fluorescence microscopy, the embedded in the specimen fluorophores emit light after their excitation with light of a certain wavelength. The general principle of a fluorescence microscope (Fig. 2-3B) includes irradiation of the specimen with a specific wavelength and then separation of the much weaker emitted fluorescence from the excitation light. The light coming from the light source is filtered through the excitation filter (only light with a certain wavelength can pass through it) and reflected from a dichroic mirror towards the objective. The latter focus the excitation wavelength on the specimen. A large amount of the excitation light is transmitted from the sample, so that only the emitted fluorescence and a reflected excitation light reach the objective. An emission filter separate the excitation from the emission light in a way that only the emission light reaches the detector. Thus the fluorescent objects are visualized with high contrast against a dark background.

2.4 Electrodeformation of giant vesicles

We used the deformation of GUVs in the presence of an AC field to measure the area change of the vesicles in response to light-induced isomerization of photosensitive molecules (F-azo). The vesicles should be deflated (diluting them in a solution with a slightly higher concentration than the solution, in the presence of which they were grown), before applying the electric field, in order to decrease the membrane tension and thus make the vesicles more floppy, and easy to deform. One can impose the deformation of the vesicles, either around their equatorial or polar axis, depending on the frequency of the electric field, and conductivity ratio between the inside and the outside vesicle solutions as shown in Fig 2.4. [99]. At high frequency the vesicles are spherical, independently of the conductivity ratio, χ. At intermediate frequencies the GUVs can assume either prolate shape (transition 1), if the χ

is bigger than 1 (higher conductivity inside than outside the vesicles), or oblate shape (transition 2), when $\chi < 1$. In the regime of intermediate frequencies the vesicles can undergo morphological change between prolate and oblate shapes (transition 3) depending on the conductivity ratio. Transition 4 (from oblate to prolate) occurs in the case of decrease of the intermediate frequencies to low frequency.

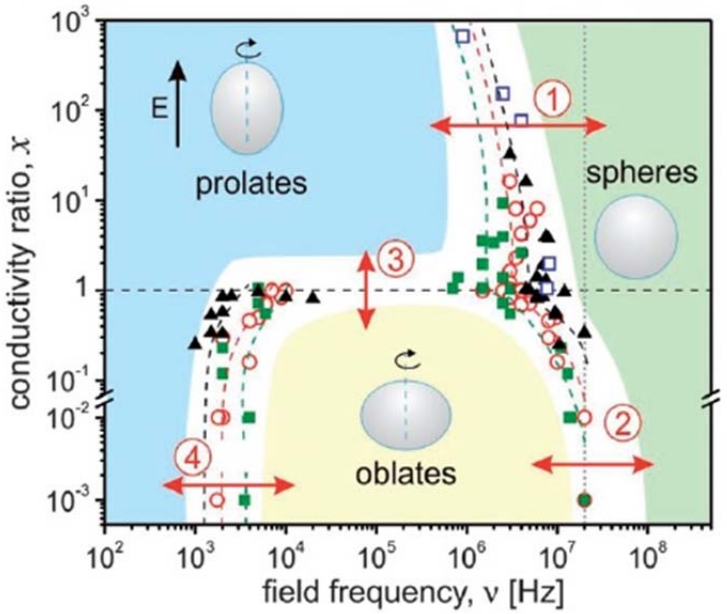

Fig.2-4. Morphological diagram of GUVs in the presence of an electric field at different field frequencies and conductivity conditions. The symbols correspond to different internal conductivity, the values of which can be found in [99]. The four types of morphological transitions are discussed in the text. The dotted vertical line shows the experimentally accessible frequency limit.

The vesicles were grown in aqueous solution containing NaCl and then diluted in NaCl-free solution, resulting in higher conductivity inside the vesicles. In these conditions, the vesicles adopt prolate deformation (elongated along the field direction), when the GUVs were subjected to an AC field with intermediate frequency. The electric field exerts forces on ions leading to their movement. Since the bilayer limits the free motion of the charges, the latter accumulate at the membrane surfaces. Because of the asymmetry of the internal and external conductivities, the charge densities across the membrane become imbalanced. Hence, the electric field induces local accumulation of cations and anions on both sides of the membrane (impermeable for ions). The net free charge density, Q, is given by

$$Q(t) = 3E_0 cos\theta \frac{\lambda_{ex}\lambda_{in}}{2\lambda_{ex}+\lambda_{in}}\left(\frac{\varepsilon_{ex}}{\lambda_{ex}} - \frac{\varepsilon_{in}}{\lambda_{in}}\right)\frac{\cos(\omega t+\phi)}{\sqrt{1+\omega^2/\omega_{MW}^2}} \quad (6)$$

where, E_0, is the electric field strength, θ and φ, are the polar and azimuthal angles, λ_{in} and λ_{ex}, are the conductivities of the solutions inside and outside the vesicle, ε_{in} and ε_{ex}, are the dielectric constants, and ω,is the angular frequency [40]. At intermediate frequencies (the range between 10^3-10^7 Hz in Fig. 2-4) the electric field lines penetrate the vesicle and acquire a component normal to the membrane. Due to its angular dependence, Q is maximal at the vesicle poles facing the electrodes and minimal at the equator. The interaction of the normal

and tangential electric fields with the charges produces normal and lateral forces f_r and f_θ, respectively. In the case of higher conductivity inside the vesicle f_θ is directed towards the poles and thus the vesicle adopts a prolate shape (Fig. 2-5A). Then one can easily calculate the vesicle area (part of which is initially hidden in the membrane fluctuations) after measuring *a* and *b*, the vesicle semi-axes along and perpendicular to the field direction, respectively. In addition, the degree of the vesicle deformation can be monitored comparing the aspect ratio, *a/b* as a function of time.

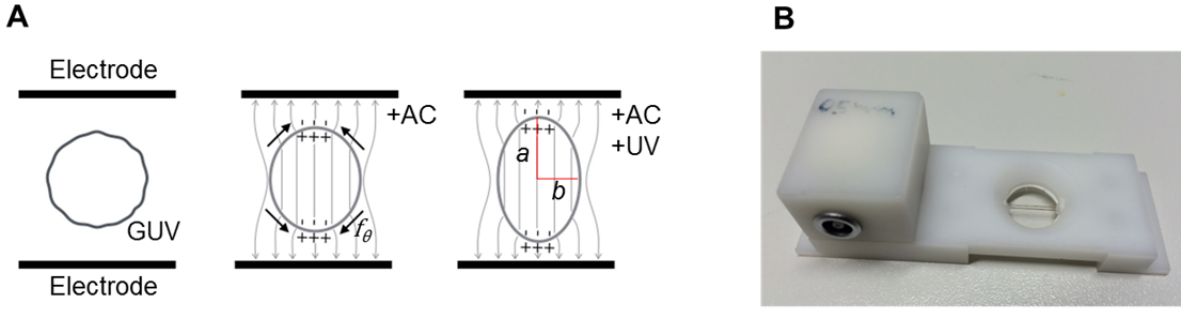

Fig.2-5. Vesicle electrodeformation. (A) Sketch of the deformation of a vesicle exposed to an AC field and UV light in the presence of F-azo. The first drawing (from left to right) shows a fluctuating GUV. Application of an electric field polarizes the membrane and stretches the vesicle (the middle sketch). Further elongation of the vesicle occurs, when the F-azo molecules photoisomerize. The two vesicle semi-axes (*a* and *b*) are indicated on the third drawing. (B) Electrodeformation chamber (top view).

After the GUVs, subjected to an AC field, attained their maximal deformation the sample was irradiated with UV light, which causes a conformational change in the F-azo molecules, integrated in the bilayer. The latter increases the area per lipid, leading to further elongation of the vesicles (Fig. 2-5A). Then we compared the vesicle areas before and during the UV irradiation and extracted the area increase, contributed by the isomerization of the photoswitches.

All electrodeformation measurements were performed in the observation chamber (Eppendorf electrofusion chamber) shown in Fig. 2-5B. It consists of a Teflon frame with a circular hole restricted below by a glass plate. A pair of parallel platinum electrodes is fixed at the glass. The vesicle solution was placed in the cavity and closed with another glass from above. The vesicles between the electrodes were observed under a phase-contrast mode.

2.5 Fluorescence recovery after photobleaching (FRAP)

The lipid lateral mobility can be quantified by FRAP. We used this technique to investigate in which phase (l_o or l_d) the F-azo molecules prefer to integrate. The FRAP method, described in Fig. 2-6, relies on the fact (regarded as a drawback in the fluorescent imaging) that the emitted fluorescence from the fluorescent probes is not a constant value and decreases with an increase in the time of excitation and/or the power of the irradiation

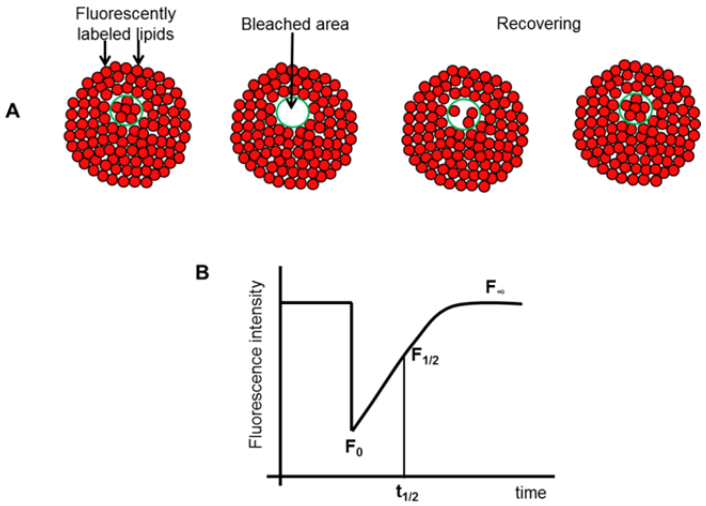

Fig.2-6. Schematic representation of FRAP. (A) A lipid bilayer stained with a red dye. A strong laser pulse bleached the fluorescent molecules in the region of interest (ROI, the green circle), followed by diffusion of unbleached molecules into the ROI. (B) A typical recovery curve, from which one can extract the diffusion coefficient (see in the main text).

A laser light is focused, on a small region of interest of the GUV, and then increased. The strong laser pulse destroys the fluorescent molecules in such a way that they irreversibly lose their fluorescence due to change in their conformation, for example. This irreversible loss of fluorescence is known as photobleaching. Since the fluorophores on the irradiated area are trapped in a state where they do not fluoresce, the bleaching region becomes dark. With time, the fluorescence of the bleached patch increases as unbleached fluorescent molecules diffuse into it and bleached ones diffuse outward. The extent of the recovery depends on the fluidity of the bilayer, its quality (whether there are any defects) and the size of the bleached area.

We obtained the diffusion coefficient, D from the recovery curves applying the following simplified equation [100]:

$$D = \frac{r_e^2 + r_n^2}{8t_{1/2}} \tag{7}$$

Where, r_e and r_n, are the effective and the nominal (i.e., user-defined) radii of the bleaching spot and $t_{1/2}$, is the half-time of fluorescence recovery or in other words the time to reach $F_{1/2}$:

$$F_{1/2} = \frac{F_0 + F_\infty}{2} \tag{8}$$

Where, F_0 and F_∞, correspond to the fluorescence intensities in the first post-bleach image and after full recovery, respectively.

The effective bleaching radius, r_e,was extracted by fitting the fluorescence intensity line profile, passing through the center of the bleached area of the first post-bleach image, with the equation:

$$f\ (x) = 1 - K\ exp\frac{-2x^2}{r_e^2} \tag{9}$$

where K is the bleaching depth. Fig. 2-7 shows the determination of r_e. Ideally, r_n and r_e would be equal, but since lipid diffusion takes place during the bleaching, the values of both radii differ. The described model accounts the latter, therefore no other corrections are needed.

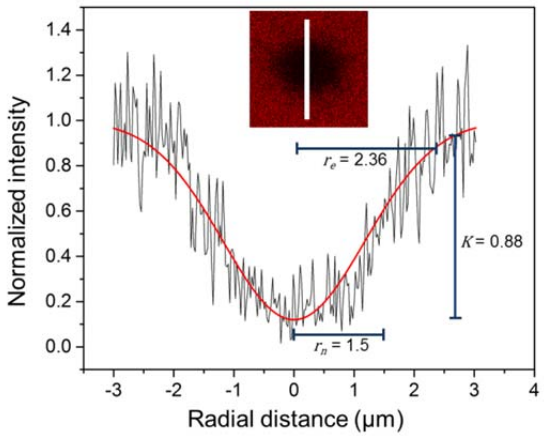

Fig.2-7. Fluorescence intensity line profile of bleached area at the first image after the bleaching. The measured intensity is shown in black. The red curve represents the fit according to eq. (9). The obtained fitting values of the effective radius (r_e) and the bleaching depth (K), as well as the nominal radius (r_n), are indicated by the blue lines. The inset shows the image used for the measurement.

2.6 Fluctuation spectroscopy

The fluctuation spectroscopy is based on direct microscopy observation and recording of the thermal fluctuations of GUVs. Vesicle shape oscillations can be used to measure the bending stiffness of membranes. The first estimate of bending rigidity using fluctuation spectroscopy was made on erythrocytes by Brochard and Lennon 40 years ago [101]. Since then the method was extended to GUVs [5, 102-104]. The measurement of κ using fluctuation spectroscopy consists of three parts: i) recording of a vesicle, ii) detection of the vesicle contour and iii) analyzing the shape fluctuations of the contour.

We used a home-developed program [5] to detect the vesicle contour from the acquired images and to perform the further analysis. Fig. 2-8 shows the process of detection of the vesicle contour. The contour finding algorithm extracts the intensity (stored in the pixels) profiles of lines in the radial direction for N different angles, which cross the vesicle contour. The cross point of a line, at certain angle, with the mean gray level of the image give the position of the vesicle contour (with a pixel resolution) at that angle. The neighboring points must have approximately the same radius in order to yield a continuous contour. The center of mass of the contour is used as a starting point to search for the contour in the next image. Thus, the vesicle movements can be traced. In the next step, a Fourier mode decomposition is performed in respect to a rescaled, by the average radius (the zeroth Fourier mode), contour.

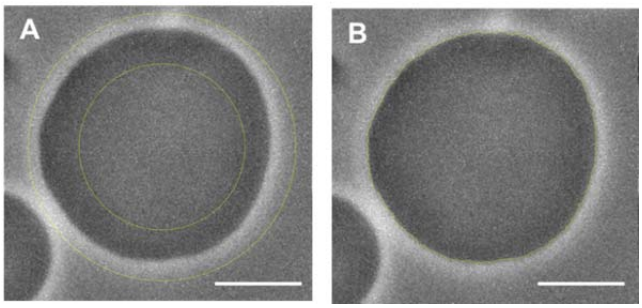

Fig.2-8. Detection of the vesicle contour. (A) the yellow circles indicate where the contour should be found. (B) the final detected contour. The scale bars correspond to 10 μm.

The spherical harmonic modes represent the modes of oscillation of a sphere. Slow oscillations are characterized by low wavenumber modes, whereas fast oscillations are represented by modes with a high wavenumber. The mean square amplitudes of the spherical harmonic modes, for quasi spherical (fluctuating) vesicles, behave as

$$\langle |u_{lm}|^2 \rangle = \frac{k_B T}{\kappa(l+2)(l-1)[l(l+1)+\bar{\sigma}]} \tag{10}$$

here $\bar{\sigma} = \sigma_{eff} R^2/\kappa$ introduces the effective tension, σ_{eff}, κ is the bending stiffness of the membrane, and $k_B T$ is the thermal energy [105]. It should be marked that for an axisymmetric vesicle, all modes which break the symmetry of the stationary shape have an index $m \neq 0$, whereas for the symmetry preserving modes (do not change the symmetry of the mean shape) $m = 0$. Since the examined vesicles remain spherical, only $m = 0$ modes contribute and thus a shift in the mean shape is reduced to a shift in the main contour merely. Considering the latter, $\langle |u_{lm}|^2 \rangle$ in eq. (10) depends only on l ($m = 0$). Therefore, one can study the vesicle fluctuations by observing only one plane. It is of importance to note that the maximum vesicle contrast is achieved at the equatorial plane (coincidence with the focal plane), where the optical axis is tangential to the membrane. Thus, one can extract information solely from the equatorial plane of a vesicle, where the mean square amplitudes follow the expression

$$\langle |v_q|^2 \rangle = \sum_{l=q}^{l_{max}} \langle |u_{lq}|^2 \rangle |P_{lq}\,(\cos\,\pi/2)\, N_{lq} \tag{11}$$

Here, l_{max}, is the cut-off of the shortest possible wavelength, P_{lq}, is the Legendre polynomial from the spherical harmonics and, $N_{lq} \equiv [(2l+1)/4\pi][(l-q)!/(l+q)!]$, is a normalization factor. The bending rigidity can be extracted from

$$\kappa/k_B T = S(q)/\langle |v_q|^2 \rangle \tag{12}$$

where

$$S(q) = \sum_{l=q}^{l_{max}} \frac{N_{lq}[P_{lq}(\cos \pi/2)]^2}{(l+2)(l-1)[l(l+1)+\bar{\sigma}]} \tag{13}$$

Considering the variance of the modes of the Fourier-expanded contour, a_q and b_q, we obtain [39]

$$\left\langle |v_q|^2 \right\rangle = \frac{1}{4}\left[\left\langle \left[a_q(t_i) - \langle a_q \rangle\right]^2 \right\rangle + \left\langle \left[b_q(t_i) - \langle b_q \rangle\right]^2 \right\rangle\right] \quad (14)$$

the measured $<|v_q|^2>$ can be introduced in eq. (11) and thus one can obtain the bending rigidity. It should be noted that vesicles which did not show a plateau for intermediate modes in a regime of reduced mean square amplitudes as a function of the vesicle mode number were discarded.

The fluctuations of a vesicle have to be recorded with a sufficient speed, which allows setting the exposure time lower than 200 μm, and for long enough time, in order to capture most of the vesicle available configurations. The camera exposure time should be ≤200 μs, otherwise the high wavenumber modes (the fast oscillations) will be lost. We used a high-speed digital camera which meets the above criteria.

3 Light-induced morphological transformations in GUVs

Almost all cellular processes occurring at the level of the membrane involve dynamic remodeling. A couple of examples of such processes include endo- and exocytosis, vesicle shedding and budding during vesicular transport [106]. Different morphological changes of the membrane are observed in the course of these processes [32, 106-108]. The mechanical properties of the bilayer and the regulating role of associated biomolecules as proteins and carbohydrates have a key function for the modulation of these shapes [109]. A well-established system for mimicking the plasma membrane when exploring such cellular processes is giant unilamellar vesicles (GUVs) [19, 27, 110, 111]. Their sizes (in the range 1-100 μm) make them amenable to direct observation of the response of the membrane in real time under a microscope. The response of GUVs when exposed to various external stimuli such as temperature and osmotic stress [85, 112-114], magnetic [115] and electric fields [99, 116-118], chemical reaction or pH gradients [59, 119] and addition of detergent [120-123] has been already characterized. Experiments with GUVs have unequivocally shown the adeptness of this system for unveiling basic material properties of the lipid bilayer.

Molecules which can reversibly photoisomerize are another intriguing tool for reshaping the membrane. The use of these molecules offers an approach for direct conversion of light into mechanical energy [124-126]. Light responsive liposomes appear to be an attractive setup for a drug delivery system. For the latter application, one typically employs liposomes encapsulating a sufficient amount of therapeutic agents. The liposomes have the ability to carry the substance in aqueous fluids (bloodstream) and modulate the drug biodistribution [127, 128]. Moreover, the application of light on liposomes, made of phoptoisomerizable lipids, can trigger a rapid release of the vesicle content [129].

Azobenzene derivatives have been the most-widely employed class of photoswitches for the photo-control of biomolecules [130]. In the past few years, the use of azobenzene derivatives for photo-control of peptides [131, 132], ion channels [133], nucleic acids and oligonucleotides [134, 135] has been reported. Azobenzene-modified lipids have been employed to study the membrane properties in model systems such as small unilamellar vesicles (SUVs) and large unilamellar vesicles (LUVs). Increase in the permeability of SUVs and LUVs [136, 137] as well as photo-control of vesicular adhesion [138] was observed.

Since GUVs are a convenient tool for directly exploring the response of the phospholipid membranes at the cell-size scale, a number of studies combining GUVs and light as an external stimuli have been performed. Different photosensitive molecules have been employed. For instance, UV irradiation of PE-porph (porphyrin bound to a lipid head group) leads to morphological changes in GUVs made of unsaturated lipids [139, 140]. When exposed to UV light, the photosensitive molecules produce singlet oxygen, which attacks the double bond(s) of the unsaturated lipids. Lipid peroxidation introduces a kink in the acyl chain, leading to expansion of the vesicle area, and thus causing the morphological changes. The membranes of GUVs dispersed in solutions of methylene blue (another light-sensitive molecule) were also observed to disrupt as a result of photooxidation [141].

As mentioned above, azobenzene derivatives present a widely used group of photosensitive molecules. Recently, bursting of multicomponent GUVs in the presence of photosensitive cationic azobenzene surfactant when exposed to UV light was reported [142]. The photosensitive molecules change their configuration from *trans*-to-*cis* under UV light irradiation. This leads to bursting of vesicles containing domains in gel or l_o phase (rigid membrane). In contrast, smaller amount of GUVs bursted, when they were composed of more fluid membrane. It was suggested that the fluid membrane can reorganize fast and thus accommodate to the change in the molecules configuration, however a mechanism of the vesicle bursting was not proposed. We also briefly examined the behavior of GUVs exposed to azobenzene molecules and observed bursting of one-component, single-phase vesicles made of DOPC (l_d phase), see Appendix A, presumably indicating that not only the membrane fluidity plays a role. Control on the membrane morphology using another type of photosensitive molecules has been reported. Reversible *exo*- and *endo*-budding transitions due to photoisomerization of an azo-lipid have been demonstrated. The effects were assigned to an increase in the membrane's surface area upon photoisomerization. [143, 144]. However, vesicles with same initial shape did not always exhibit the same morphological transformations, which might suggests that the area increase is not the only parameter involved in this process.

Despite that a number of light-triggered morphological changes in GUVs have been observed, little is known about the mechanism behind. In this Chapter, we investigated the possible mechanisms for lipid morphological transitions caused by light. We used an o-tetrafluoroazobenzene derivative (F-azo), which isomerizes upon irradiation with visible or UV light [73], see Fig. 1-11 in Chapter 1.5.2. Contrary to the typical design of azobenzene surfactants [142], F-azo is not a cationic molecule (with an ammonium group) but an anionic one (with a carboxylate group). This feature should lower the cytotoxicity of the photoswitch, as well as preventing adsorption to glass surfaces (in particular microscope slides). Finally, F-azo derivatives are highly thermally stable, i.e., their cis forms thermally convert back to the *trans* forms very slowly (half-life of ca. 20 h at 60 °C) [145].

Using experimental methods and MD simulations, we characterized the mechanism of photo-induced morphological changes in GUVs. These morphological changes were imaged employing phase-contrast microscopy. We used liquid chromatography and MD simulations to address the partitioning and the orientation of F-azo in the membrane, respectively. The relative increase in membrane's area, caused by F-azo photoisomerization, is measured by vesicle electrodeformation approach

3.1 Methods

3.1.1 Vesicle preparation

GUVs were grown using the electroformation method[18]. In brief, 16 μL of a 4 mM lipid stock solution of DOPC in chloroform were spread on a pair of conductive ITO glasses. The phospholipid film was dried under N_2 stream for 5-10 min and after that the glasses were kept under vacuum for 1-2 h to remove all traces of the organic solvent. The two glasses were placed with their conductive sides facing each other and separated by a 2 mm thick teflon spacer. This electroswelling chamber was filled with 0.1 M sucrose (or glucose) solution and connected to a function generator. An AC field (1.1 V, 10 Hz) was applied for 1 h at room temperature to swell the GUVs. After the GUVs were formed they were diluted twice in an isoosmolar glucose (or sucrose) solution containing the desired F-azo concentration. The incubation of the GUVs with F-azo lasted for 1-2 h. For the vesicle electrodeformation measurements, the GUVs were grown in the presence of 0.5 mM NaCl and 0.1 M sucrose.

LUVs were made by extrusion. 108 μl of DOPC dissolved in chloroform (21 mM) were mixed in a glass tube with 29 μl chloroform solution of DPPE-Rh (0.8 mM). The solvent was evaporated with N_2 stream and the tube was additionally dried under vacuum for 2 h. The lipid film was then hydrated by adding a 0.1 M sucrose solution, for a final DOPC concentration of 1 mM and 1 mol% (0.01 mM) of DPPE-Rh. The obtained solution was vortexed for 5-10 min and the formed multilamellar vesicles were subjected to 20 cycles of extrusion through a polycarbonate membrane (Whatman, Maidstone, UK) with pore diameter of 100 nm. The whole procedure was performed at room temperature. Before the experiments, the LUVs were diluted 5x in a 0.1 M sucrose solution.

3.1.2 Dynamic light scattering (DLS) of F-azo and LUVs

The size distribution of F-azo aggregates and the LUVs were determined at 25°C with a Zetasizer Nano ZS (Malvern Instruments, Worcestershire, UK), operating with a 4 mW HeNe laser (632.8 nm), a detector positioned at the scattering angle of 173°, and a temperature-control jacket for the cuvette. Aliquot of 1 ml F-azo with concentration of 0.25 mM was degassed for 10 min with ThermoVac (MicroCal, MA). Three DLS measurements consisting of 20 runs with duration of 5s were performed. DLS measurements were performed also on LUV suspensions to determine the vesicle size. The sample was degassed with ThermoVac for 10 min before the measurements.

3.1.3 Vesicle imaging

The giant vesicles were observed under phase-contrast mode of an Axio Observer D1 (Zeiss, Germany) microscope, equipped with a Ph2 20x (NA 0.5) objective. Images were taken with an ORCA R2 CCD camera (Hamamatsu, Japan). The samples were irradiated using the HBO 100W mercury lamp of the microscope. For UV and blue irradiation the light from the mercury lamp was filtered with a filter set 49 (with 365 nm excitation and 445/50 nm emission filters) (Zeiss) and filter set 38(with 470 /40 nm, excitation and 525/50 nm emission

filters) (Zeiss), respectively. The power of the irradiation was 6.1 mW/cm^2 for the UV filter set and 2.8 mW/cm^2 for the blue one. The power intensities were measured with LaserCheck (Melles Griot).

3.1.4 Vesicle electrodeformation

Application of an AC field to GUVs was used to measure the relative area increase due to the photoisomerization of the F-azo molecules. The approach is based on the deformation of vesicles when exposed to the field [146] and is similar to an approach developed in [139]. GUVs grown in the presence of NaCl (0.5 mM) were exposed to an AC field (5 V/m and 1 MHz) applied in an electrofusion chamber (Eppendorf, Germany) with parallel cylindrical electrodes (92 μm radius), spaced at 500 μm. Under these conditions the vesicles elongate and adopt a prolate shape with axis of symmetry parallel to the field direction [41, 146]. The experiment proceeds with first applying an AC field to a selected vesicle. The field deforms the vesicle into an ellipsoid, pulling out excess area stored in fluctuation. The total vesicle area, A, can be calculated from the vesicle axis determining from the image. Then, the vesicle is exposed to UV light and the resulting relative area increase $\Delta\bar{A}$ is calculated from:

$$\Delta\bar{A} = \frac{\Delta A}{A} = \frac{A_{UV} - A}{A} \tag{15}$$

Where, A_{UV}, is the area of the vesicle when exposed to UV light. Note that the above is valid as long as the vesicle retains its ellipsoidal shape.

3.1.5 Molecular dynamics simulations

Molecular dynamics (MD) simulations were performed using parameters from the amber lipid14 force field for DOPC [41, 147] and parameters for the F-azo molecules from [148], based on the general amber force field [149]. Partial charges were derived for the *cis* and *trans* conformations separately using the R.E.D. tool scripts [150]. Structure optimization of the molecule was performed with Gaussian at the HF/6-31G* level of theory, and the final set of charges was obtained from an ensemble average of 50 structures generated from a 20 ns MD trajectory. The topologies for F-azo and DOPC were converted using the glycam2gmx.pl script [151, 152]. The system was solvated with TIP3P water [153]. All systems contained 256 DOPC and 16800 water molecules.

The potential of mean force (PMF) of the z-coordinate of the F-azo aromatic rings relative to the center of mass of the bilayer, were performed using umbrella sampling. Initial structures for 41 umbrella windows between z=0 nm and z= 4 nm were generated for both the *cis* and *trans* conformation by pulling the molecule from its equilibrium position with a velocity of 0.211 nm/ns and a force constant of 200 kJ/mol. Each window was equilibrated for 10 ns with a force constant of 200 kJ/mol. Data was collected from 50 ns trajectories using a force constant of 1000 kJ/mol. The PMF was constructed using the weighted histogram analysis method.

To obtain the area per molecule change upon isomerization, simulations with 2, 4, 6, 8, and 10 F-azo molecules in the *cis* and in the *trans* conformation, distributed evenly between the leaflets were performed for 300 ns.

All simulations were performed in the NPT ensemble with GROMACS 4.6.4 [154, 155]. Covalent bonds involving hydrogens were constrained using LINCS [156] while water molecules were kept rigid with SETTLE [157], allowing the use of a 2 fs time step. Systems were equilibrated using the v-rescale [158] thermostat and Berendsen barostat [159].

In production simulations, temperature and pressure were controlled with the Nose-Hoover thermostat [160, 161] and Parinello-Rahmann barostat [162] with semi-isotropic pressure coupling, respectively. Lennard-Jones and short range electrostatic interactions were cut-off at 1.0 nm, long range electrostatics were calculated using the particle mesh Ewald method [163].

In this work, the MD simulations and the analysis of the obtained data from the simulations were performed by Andrea Grafmüller at Max Planck Institute of Colloids and Interfaces and the planning of the simulated system and results were discussed jointly.

3.1.6 Size exclusion chromatography

Size exclusion chromatography was performed on a Superdex™ 200 10/300 GL column (GE Healthcare, Freiburg, Germany) with a high-performance liquid chromatography (HPLC) system (Shimadzu, Duisburg, Germany) equipped with a RF-10A xl fluorescence detector and and a SPD-M10A vp diode array detector. All samples were degassed for 10 min with ThermoVac and F-azo molecules were centrifuged at 40000 rpm for 30 min at 15°C with a Sorvall Discovery M150 centrifuge (S55 rotor, Thermo Fisher Scientific, Waltham, MA, USA) before loading.

As mobile phase and sample buffer a 0.1 M sucrose/glucose solution was used. For all experiments, the final F-azo and lipid concentrations were 0.25 mM and 0.1 mM, respectively. Samples were loaded to the column at a volume of 50 µl and runs of 60 min were performed with a flow rate of 0.3 ml/min at a maximum pressure limit of 1.1 MPa. The extruded LUVs had a vesicle diameter of 136 nm prior the mixing with F-azo as measured with DLS Vesicles were incubated for 2 h with F-azo before loaded on the column to reach an equilibrium of partitioning. Fluorescently labeled LUVs were detected with excitation at 550 nm and emission at 580 nm. Absorbance of F-azo molecules was monitored at 320 nm.

The peaks of the F-azo elution profile in the presence of LUVs (see Fig. 2) were integrated using the peak analyzer tool in OriginPro 2015. The integration was performed in respect to an automatically calculated constant baseline, which corresponds to the minimum of the F-azo absorbance.

3.1.7 Effect of the sugar asymmetry on the spontaneous curvature

The GUVs were prepared by electroformation, see 3.1.1 above. Vesicles were grown in either 100 mM sucrose or glucose solutions and placed in a microfluidic chamber. The latter was produced following the method described in [164]. Briefly, the master mold of the microchannels is made on a silicon wafer by mask lithography. The casts are made of PDMS,

which was poured over the master mold to a thickness of approximately 5 mm and cured for 1 h at 70°C. Once the cast was peeled of the master, two holes were perforated as in- and outlet. The PDMS cast was sealed onto a glass cover slip after 1 min of activation of both surfaces by plasma produced with a radio-frequency generator (Plasma Cleaner PDC-32G, Harrick). For degassing, the outlet was blocked and either 100 mM glucose or sucrose was introduced via the inlet. Then, the chamber was kept under vacuum for about 10 min. By releasing the vacuum the solution fills the chamber. GUVs were placed into the inlet and suction pressure was applied by a syringe attached to the outlet to fill the chip with GUVs. The GUVs were settled into the side channels by either gravity or centrifugation. The exchange of the external solution was done in the same manner as the loading of the GUVs. The vesicles were observed under phase-contrast mode on a Zeiss Axio Observer D1 microscope equipped with a 20x air objective with NA 0.5.

3.2 Results

We used F-azo molecules, an azobenzene derivative, as photoswitch and investigated the influence of their photoisomerization on GUVs made of DOPC. The *trans* conformation of the molecules is nearly planar, while the *cis*-isomer is distorted with its phenyl rings twisted out of the plane of the azo group (see Fig. 1-11 in Chapter 1.5.2). To observe the presented in this Chapter morphological changes in GUVs, we have used an UV light for *trans*-to-*cis* F-azo isomerization. This may be of concern for the membrane and cell viability as exposure to UV light is destructive [165]. However, F-azo is able to fully isomerize under visible light: *trans*-*cis* with cyan (~ 488 nm) and *cis*-*trans* isomerization with blue (~ 420 nm) light [73], surprisingly, we did not detect any vesicle changes under cyan irradiation. We speculated that the most possible reason could be the power difference between the UV and cyan range of the spectrum of our light source (HBO mercury lamp). The emission spectrum of the latter is shown on Fig. 3-1. We measured the power of irradiation for the used wavelengths of our system (the signal was measured above the objective at the respective focal distance using LaserCheck (Melles Griot). At 488 nm, the power is ~ 1.8 mW/cm^2, while the one for the UV and blue light is 6.1 and 2.8 mW/cm^2, respectively. We employed more powerful cyan-light sources, including an in-house build device with LED source (~ 2.7 mW/cm^2 measured above the objective at the respective focal distance), but no vesicle morphological changes were observed.

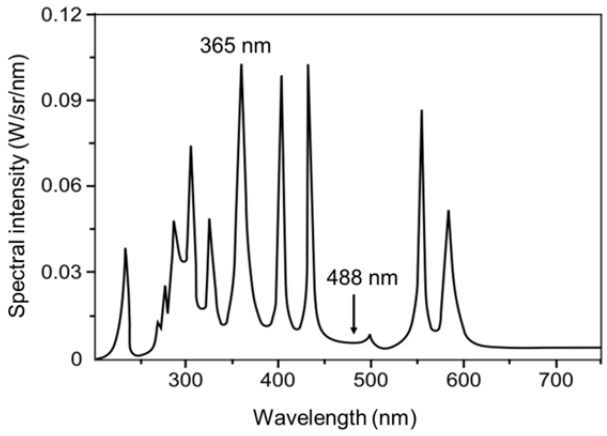

Fig. 3-1. Spectral irradiance of 100 watt high pressure mercury lamp. The intensity at 365 nm (the used UV range at which F-azo isomerize to *cis*) is much stronger than the intensity at 488 nm (the visible range where *trans*-to-*cis* F-azo isomerization takes place).

3.2.1 Behavior of the F-azo molecules in solution

In aqueous solutions, F-azo molecules form aggregates at low concentration (< 0.25mM) due to limited water solubility. Crystal-like aggregates were observed when using higher concentrated (> 0.25 mM) F-azo solutions, see Fig. 3-2A. In order to exclude the perturbing effect of these crystal-like aggregates (their presence affects the quality of the imaging), we filtered the F-azo stock solution (through a filter with pore size: 0.22 μm). The latter was stable and the crystal-like structures were not observed after filtration. We were concerned that the total concentration of F-azo molecules might have been reduced during the filtration step. We measured the absorbance at 320 nm of both unfiltered F-azo (in the concentration range of 0-0.1 mM) and filtered F-azo (for two concentrations: 0.025 mM and 0.05 mM). Then the extinction coefficients of the filtered and unfiltered F-azo (for 0.025 mM and 0.05 mM) were compared. The concentration of the filtered F-azo was ~ 3% lower than the one of the unfiltered F-azo solutions. This small concentration difference was considered in the calculation of the concentration of the stock F-azo solution.

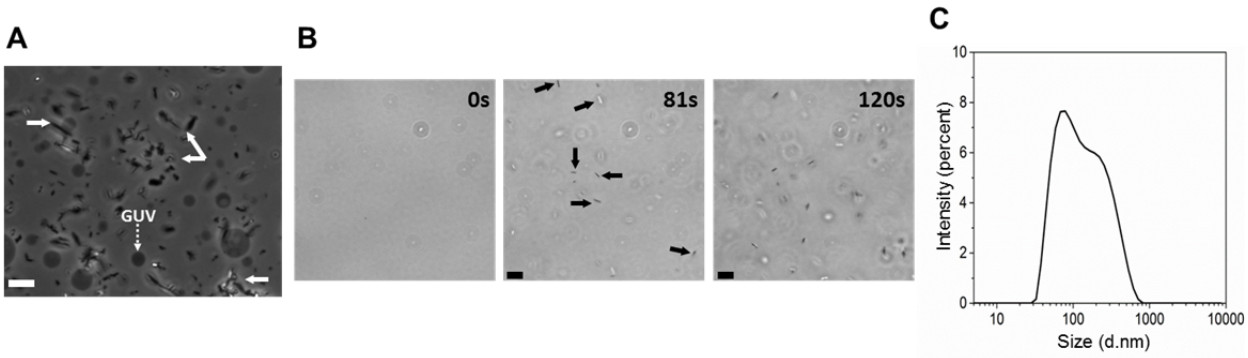

Fig. 3-2. Aggregate structures of F-azo. (A) GUVs in the presence of unfiltered F-azo. The concentration of F-azo is 1.25 mM. The continuous arrows indicate several F-azo crystal-like aggregates. (B) UV-induced aggregation of F-azo (0.25 mM). The time of the irradiation is indicated on the top-right corner of each snapshot. The snapshot at 0 s shows the sample before the UV light irradiation. The arrows point on the first appeared aggregates. The scale bars at both panels correspond to 10 μm. (C) Size distribution of F-azo aggregates in filtered, 0.25 mM F-azo solution measured by DLS.

During prolonged UV light irradiation the F-azo molecules start to form aggregates in size of a few μm, which appeared after ~ 2 min UV irradiation of a 0.25 mM filtered F-azo solution, see Fig. 3-2B. Note that during our experiments, the samples were always irradiated with UV light for less than a minute, which is below the threshold of the appearance of the aggregates. However, for the filtered solutions of 0.25 mM F-azo, the DLS measurements indicated the presence of two populations of aggregates with broad (submicron) size distribution even without UV light irradiation (Fig. 3-2C). The nature of these submicron aggregates remains unclear.

3.2.2 F-azo partitioning in the membrane

We determined experimentally the partitioning of F-azo in the membrane, employing size exclusion chromatography (Fig. 3-3). The latter, similarly to the DLS measurements, also detected two populations of F-azo aggregates. The free F-azo eluted as two peaks with maxima at ~ 7 and ~ 8.1 ml that could be detected via UV-absorbance at 320 nm. Free LUVs eluted earlier at ~ 5.5 ml, as they do not absorb at 320 nm their elution profile was monitored via their intrinsic fluorescent probe (Fig. 3-3A). However, a peak at the same retention time occurred in the chromatogram when the vesicles were mixed with F-azo at lower intensity (Fig.3-3B). The latter is in line with the large excess of F-azo in the solution also in presence of LUVs. We conclude that this peak corresponds to a signal obtained from F-azo molecules incorporated in the lipid bilayer of the LUVs. Accordingly from the peak areas (see panels C and D in Fig. 3-3), we quantified the concentration of incorporated F-azo in LUVs to 1.85 ±0.13 μM, corresponding to ~ 0.74% ± 0.05% of the total F-azo present in the sample. This implies insertion of 1 F-azo molecule on every 54 ± 4 lipids.

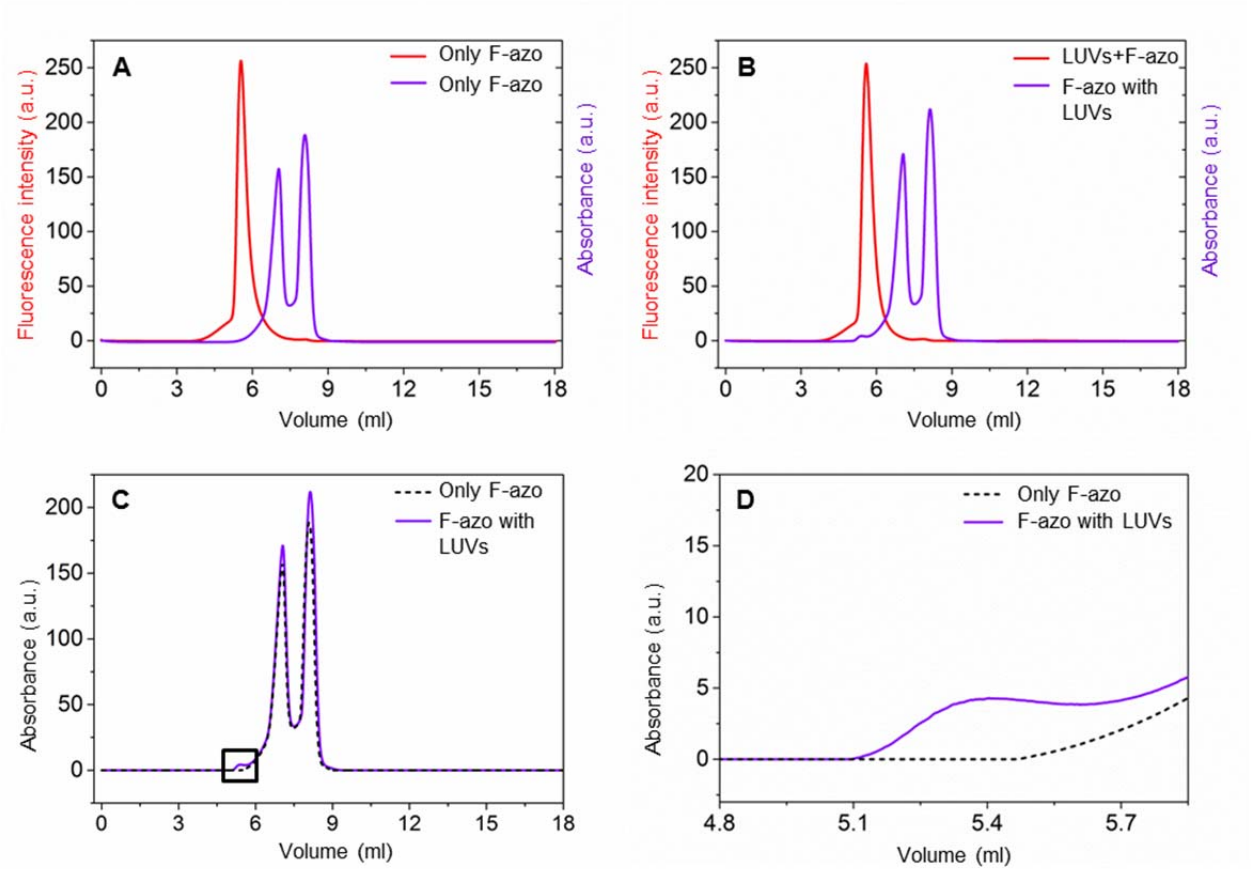

Fig. 3-3. Chromatograms of filtered F-azo molecules and LUVs. On panel (A) are shown the elution profiles of unmixed LUVs (red curve) and F-azo (purple curve). (B) Corresponds to the elution after 2 h incubation of F-azo with the liposomes. (C) Elution profiles of "free" F-azo molecules (black curve) and after incubation with LUVs for 2 h (purple curve). The peak at ~ 5.4 ml (area closed in the black box) corresponds to the integrated F-azo amount in the membrane. (D) Presents a magnification of the latter. The final F-azo and lipid concentration for all experiments was 0.25 mM and 0.1 mM, respectively. The absorbance of F-azo was measured at 320 nm.

3.2.3 A vesicle response to F-azo isomerization

GUVs electroswelled in 100 mM solution of sucrose were mixed (volume ratio 1:1) with a solution of glucose and F-azo to reach a final F-azo concentration of 0.25 mM. The molarity of the glucose/F-azo solution is slightly higher (~ 105 mM) than the one of the sucrose solution in order to deflate the GUVs, release their initial tension and render them quasi-spherical, and with visible fluctuations. After 2 h of incubation with the F-azo molecules, the GUVs were irradiated with UV (365 nm) or blue (470 nm) light and their behavior recorded.

Upon exposure to UV light, all quasi spherical vesicles exhibiting visible fluctuations underwent morphological transitions in response to the photoisomerization of F-azo. One example is shown on Fig. 3-4A. In comparison, no visible morphological changes were detected for vesicles which appeared initially tense (spherical and without visible fluctuations). Under UV light, when the F-azo molecules change their conformation from *trans*-to-*cis*, quasi-spherical vesicles transforms into a prolate-shaped vesicles which is followed by the expelling of a small bud (*exo*-bud). The latter remains connected to the vesicle via a thin neck. The process is reversible and the *exo*-bud is re-adsorbed into the vesicle body under blue light irradiation (Fig. 3-4B), yet at a slower speed.

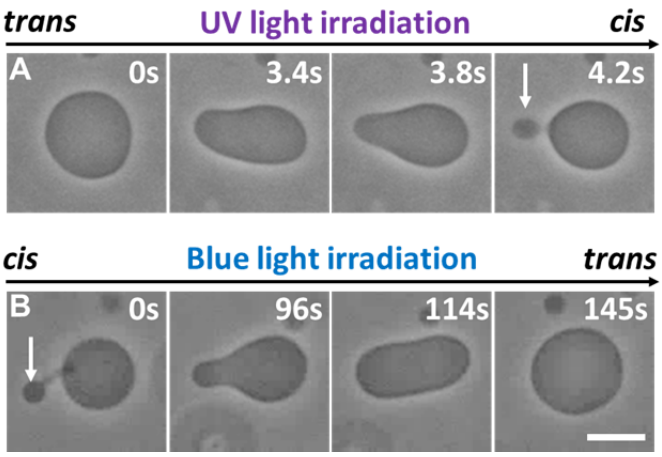

Fig. 3-4. Dynamic response of one quasi-spherical vesicle to photoisomerization of F-azo at bulk concentration of 0.25 mM. (A) Vesicle morphological changes under UV light irradiation (365 nm). The vesicle undergoes budding. The arrows point to the expelled but. (B) Shape transitions of the same vesicle when exposed to blue light (470 nm). The bud is re-adsorbed and the vesicle attains its initial quasi-spherical shape. The time after initiation of the radiation is indicated on each snapshot. The scale bar represents 10 µm.

The exchange of the filters for UV and blue light takes approximately 10 s. Under UV irradiation, vesicles with diameter of 10-20 µm undergo budding in the first 4-15 s. The vesicles remain prolates (do not expel buds) if the UV light is switched off during the first few seconds of the irradiation. The bud re-adsorption under blue light takes typically ~ 2 min to complete. The morphological cycles can be repeated without any significant differences (in the different cycles, the buds may protrude on different parts of the same vesicle). Ten cycles of this reversible morphological change were observed on another vesicle (data not shown).

We also explored the response of vesicles which were not only diluted in F-azo solutions after formation as discussed above, but were grown in the presence of F-azo (0.25 mM) and exposed to UV and blue light. The same vesicle response was observed. In contrast, no detectable changes in vesicles in the absence of F-azo were detected when exposed to UV light for 1 min, see Fig. 3-5. In addition, the UV irradiation was not found to change the temperature in the observation chamber. Thus, UV light irradiation alone cannot cause the observed shape transformations in our system when F-azo is absent.

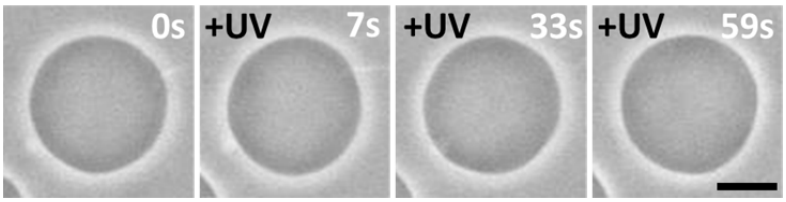

Fig. 3-5. Effect of UV light (365 nm) on F-azo-free GUV. A quasi-spherical vesicle was exposed to UV light in the absence of F-azo. The UV irradiation started at the 7th second. The vesicle does not undergo visible morphological changes for ~ 60 s of UV irradiation. The scale bar corresponds to 10 µm.

3.2.4 Energy of F-azo flip-flop and desorption from membrane

To assess the distribution of F-azo between the solution and the membrane and between the two leaflets of the membrane, we performed MD simulations. Snapshots of the DOPC bilayer with the two different isomers are shown in Fig. 3.6A, and 3.6B. The amphiphilic nature of F-

azo results in positioning the molecule at the head group – tails interface. The *trans* F-azo isomer tends to penetrate deeper into the membrane than the molecule in *cis* conformation, and to orient along the bilayer normal, whereas the *cis* isomer aligns at the head-tail interface, see Fig. 3-6A, and 3-6B.

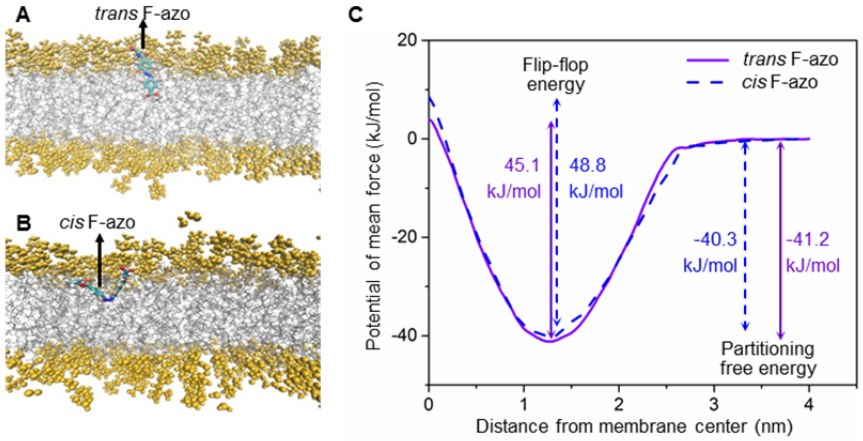

Fig. 3-6. MD simulations of one F-azo molecule in a DOPC bilayer composed of 256 lipids. (A, B) Orientation of both trans and cis F-azo in the membrane. DOPC head groups are shown in orange, tails in grey. The bonded structure of F-Azo is color-coded by atom (red: O, cyan: C, white: H, blue: N, rose: F) (C) PMF for *trans* and *cis* F-azo.

The profiles of the potential of mean force (PMF) to displace the F-azo molecule from the water phase to the center of the bilayer at z = 0 are displayed in Fig. 3-6C. The partitioning free energies, ΔG_{min} corresponding to the depths of the potential minima, are similar $\Delta G_{min} \approx$ -40 ± 5 kJ/mol for both the *trans* and *cis* conformation. This value suggests that the molecules insert into the membrane regardless of their conformation. Moreover, no desorption from the bilayer is expected due to the conformational change of F-azo.

The profile of the potential of mean force also suggests that the energy barrier for flip-flop of F-azo is ~ 50 kJ/mol (see Fig. 3-6C). This value is higher than the one of cholesterol ~ 24 kJ/mol [166], but it is lower than that of lipids ~ 78 kJ/mol [167]. The typical timescale for cholesterol flip-flop in polyunsaturated bilayers (DAPC) is < 1 s, while the flip-flop time of fluorescent lipid analog (NBD-PE) in a membrane made of DOPC (as in our model system) is ~ 1 h [166, 168]. Since the energy barrier for flip-flop of F-azo has an intermediate value, we expect that the flip-flop rate of the molecules in our system is in the time range of 1-60 min. The latter suggests that within the incubation time of the GUVs with F-azo (1-2 h), the photoswitches are distributed in both membrane leaflets.

3.2.5 Calculation of F-azo partition coefficients from MD simulations

The partition coefficient of a molecule, type I, between two phases (I and II) can be defined based on the molar concentrations c_i in the two phases, as $K^{(c,c)} = \frac{c_i^I}{c_i^{II}}$. This quantity can be easily calculated from the HPLC data, volume of the lipid phase is known. Here we use a value estimated from the area per lipid and membrane height in the simulation. Using 54 lipids per 1 F-azo molecule (obtained from the HPLC measurement), and volume of 1.73 nm^3/lipid, we obtain $K^{(c,c)} = 0.014$.

To compare this value to the MD data, there are different ways to estimate the partitioning of molecules from a free energy profile. The simplest approach is to use the free energy difference, between the minimum and the solvent phase, $\Delta G_{\min}$. This yields the ratio of molecules $K_{\Delta G_{min}}^{(N,N)} = \exp(-\beta \Delta G_{min})$, where β = 1/k_BT, in the two phases. To compare the system size dependent value $K^{(N,N)}$ to the experimental estimate of $K^{(c,c)} = K^{(N,N)} * \frac{V_w}{V_L}$, the relative volumes of the lipid and water phases are required. As a solution with 0.1 mM lipid was used, and using the above estimate of 1.73 nm^3/lipid, we obtain the ratio $\frac{V_w}{V_L}$. = 9577.5. The result suggests 1 F-azo per 11 lipids molecule (1 F-azo/11 lipids). This seems to be quite far from the experimental value 54 lipids/F-azo. On the other hand, the approximation of taking into account the minimum position only, assumes that all solutes are located at the minimum position. As the solutes are free to move, other positions in the membrane may also contribute, and can be taken into account. Since using ΔG_{min} only slightly overestimates the partitioning into the membrane, we also calculate $K^{(c,c)}$ using the entire free energy profile, by dividing the system into n thin layers, i=1 to *n*, and calculating the contributions for each layer.

$$K^{(N,N)} = \frac{\sum_{i=1}^{n_l} v(z_i) \exp(-\beta \Delta G(z_i))}{\sum_{j=n_l+1}^{n_{box}} v(z_i) \exp(-\beta \Delta G(z_i))} \quad (16)$$

where n_l is the number of slices in the membrane phase, and $i > n_l$ is the water phase. Here we define the boundary of the lipid phase to be at $z = 2.6$ nm, where the slope of the PMF becomes flat. We estimate a ratio of 1 F-azo/88 lipids. The results are summarized in Table 1.

	$K^{(c,c)}$	ΔG_{min} (kJ/mol)	Lipids/1 F-azo molecule
Experiment (HPLC)	0.014	-33.3	**54**
Minimum ΔG (MD)	0.001	**-40**	11
Minimum ΔG +Error bar	0.007	**-35**	27
Entire ΔG profile	**0.023**	-32.1	88

Table 1. Comparison of F-azo partitioning into the DOPC bilayer, using different approaches. Bold values are the 'measured' quantities, from which the others are calculated.

In addition, we estimated the partitioning free energy, ΔG_{exp}, from the experimentally obtained value of the *trans* F-azo partitioning (54 lipids/1 Fazo) to be ΔG_{exp} = -33 kJ/mol. The latter agrees reasonably well with the theoretically obtained ΔG_{min}.

3.2.6 Area change caused by F-azo isomerization

From the obtained morphological changes of quasi-spherical vesicles, we speculated that the area of the vesicle increases during the photoisomerization of F-azo in the membrane. To assess this area increase, we employed vesicle electrodeformation, see the Materials and methods (section 3.4.1). The GUVs were formed in the presence of salt and diluted with salt-

free solution to establish higher conductivity inside. This condition ensures prolate deformation in vesicles exposed to AC field [99]. The vesicles were deflated by diluting them in a solution composed of glucose (~ 105 mM) and the desired concentration of F-azo. After an incubation period of 2 h, the vesicles were exposed to electric field which deforms them and pulls out the membrane fluctuations. The total vesicle area can be calculated from the ellipsoidal vesicle shape. Subsequently, the vesicle was exposed to UV light (with the AC field still on) and the change in the vesicle area recorded. Because of the sugar asymmetry (sucrose inside and glucose outside), after preparation the vesicles appear dark on a lighter background when observed under phase contrast (Fig. 3-4). Neither the incubation with F-azo, nor the vesicle electrodeformation, nor the irradiation caused loss of contrast which is an indication that the membrane remains intact throughout the experiments.

First, we investigated the degree of deformation of F-azo-free GUVs exposed to an AC field. We found that ~ 7 seconds are typically sufficient for a vesicle (of typical radius ~ 10-20 μm) in the absence of F-azo to attain its maximal deformation (see Fig. 3-7). Hence, for the measurements presented in this section the UV light irradiation was applied after applying the electric field for at least 7 s.

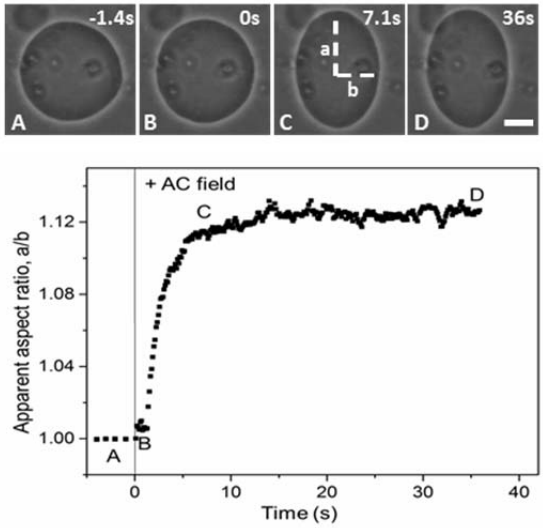

Fig. 3-7. Deformation of a vesicle in the presence of an electric field. Snapshots show the dynamic of the electrodeformation. The AC field was switched on at 0 s (snapshot B) and continued for ~35 s (C and D). The graph shows the apparent aspect ratio in relation of the time. One can see that the GUV riches its maximum deformation for ~ 7 s (C). The scale bar corresponds to 10 μm.

The initial degrees of deformation of the vesicles in AC field and in the absence of UV irradiation (compare the images and data in Fig. 3-8) are different and this is not related to the overall concentration of F-azo but depends on the initial excess area available for deformation (or volume-to-area ratio), which is different for every vesicle in the samples. This excess area is quantitatively represented by the reduced vesicle volume (i.e., the ratio between the vesicle volume and the volume of a sphere of area equal to the vesicle area) defined as

$$v = \frac{3\sqrt{4\pi}\,V}{A^{3/2}} \tag{17}$$

where V is the vesicle volume as calculated from the ellipsoidal shape of the vesicle exposed to AC field. As calculated from the maximal achieved deformation in AC field for the vesicle in Fig. 3-8A (at 7.1 s after switching the field on), the reduced volume is v ~0.996, while the reduced volume of the vesicle in Fig.3-8B is ~ 0.967 (smaller reduced volume correspond to more excess area). The electrodeformation experiments showed that the UV irradiation of vesicles in the presence of F-azo leads to an increase in the membrane area as a result of the *trans*-to-*cis* F-azo isomerization. Figure 3-8 shows the relative area increase in GUVs for two different F-azo concentrations.

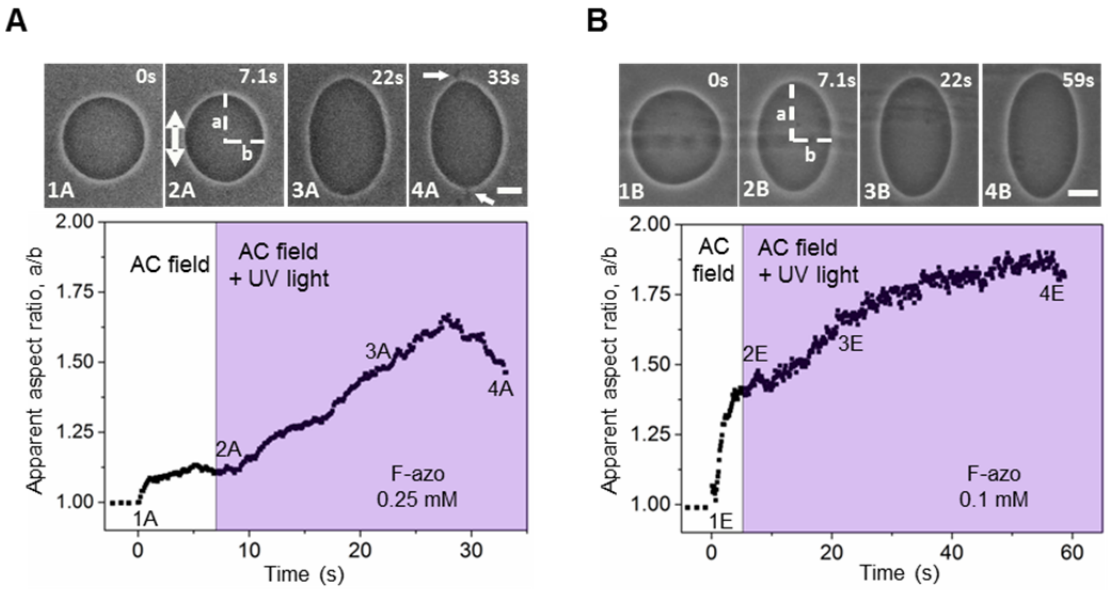

Fig. 3-8. Deformation and budding of a vesicle caused by F-azo conformational change in the membrane at two different F-azo concentrations: (A) 0.25 mM and (B) 0.1 mM. The snapshots in both panels correspond to the time frames indicated on the upper left corner. (1A and 1B) vesicle in the absence of field, (2-4 A and B) the vesicle is exposed to an AC field (5 V/m and 1 MHz). The direction of the field is indicated in snapshot 2A. The UV irradiation starts after 7.1 s (2A and 2B). At the higher F-azo concentration, the vesicle expels two buds, see arrows in snapshot 4A. The scale bars correspond to 10 µm. The graphs in (A) and (B) show the vesicles degree of deformation (a/b) over time; these data is used to calculate the change in the vesicle area resulting from *trans*-to-*cis* isomerization of F-azo under UV irradiation.

Since our other measurements (partitioning in the membrane and vesicle morphological changes) were performed with 0.25 mM F-azo, we first explored the vesicle area change at this concentration, see Fig. 3-8A. The UV irradiation is initiated at the 7.2 second. After around 22 seconds, the vesicles are typically no longer elliptical. They first adopt lemon-like shapes and start budding in the area of the poles facing the electrodes (see last snapshots in Fig. 3-8A). The exact area of the vesicle can be deduced from measuring the two semi-axes of the vesicle when the vesicle is still an ellipse. For this vesicle, the relative area increase before budding (after 22 s of irradiation) was $\Delta\bar{A}_{22s}$ = 4.6 %, see Eq. 14 in 3.1.4 above. During and after budding, the vesicle area cannot be deduced correctly from the phase-contrast microscopy images because of the small size of the buds. The relative area increase ~22 s after the irradiation (i.e. shortly before budding) measured on 30 different vesicles from different preparation batches is $\Delta\bar{A}_{22s}$ = 4.3 % with standard error of mean ±0.4 %.

The same experiment was repeated at a lower concentration of F-azo (0.1 mM), see Fig.3-8B. At this concentration, most of the vesicles did not expel buds and the GUVs remained elliptical attaining their maximum deformation under AC field. We used the data to deduce the total area change in the vesicles caused from F-azo isomerization. Between 55 and 60 s were sufficient for the vesicles to reach their maximal deformation. For the example in Fig. 3-8B, $\Delta\bar{A}_{max}$= 5.1 %. For the maximal area increase measured on 30 different vesicles from different preparation batches, we found $\Delta\bar{A}_{max}$= 4.8 % with standard error of mean ±0.5 %.

To be able to compare the results for the two measured concentrations, we also measured the relative area change ~22 seconds after the irradiation (i.e., before budding is observed for the samples with 0.25 mM F-azo). Under these conditions the average relative area increase is $\Delta\bar{A}_{22s}$ =2.4 % ±0.3 %. This value is lower than 4.3 % presumably due to the lower F-azo concentration in the membrane.

We observed bud readsorption and repeated budding in the presence of an AC field when the vesicles were irradiated with blue and UV light respectively (Fig. 3-9). The vesicle in Fig. 3-9 expels buds during UV light irradiation (snapshot B). The buds are reabsorbed by the vesicle upon blue light irradiation (snapshots C and D). The budding process repeats, when the vesicle is irradiated with UV light for a second time (snapshot E). An AC field (1 MHz, 1 Vpp) was constantly applied. The graph shows the apparent aspect ratio of the vesicle during the process. After the budding event the vesicle deformation decreases (B and E). During the blue light irradiation, the deformation reaches its previous level due to the reabsorption of the buds. Note that the gaps in the curve, after the first UV light irradiation and before the second one, are due to the change of the filters for blue and UV light.

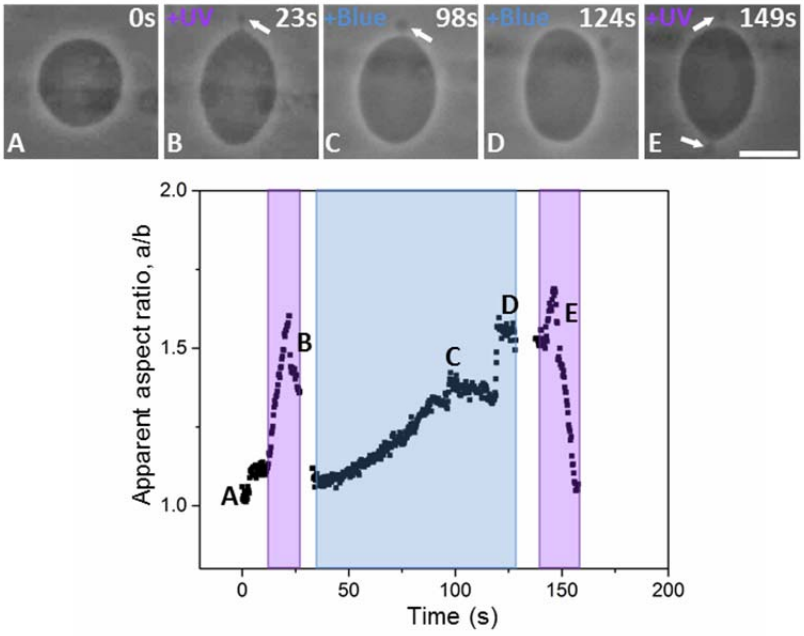

Fig. 3-9. Degree of deformation during budding-reabsorption processes. The F-azo concentration is 0.25 mM. Snapshots show the sequence of the process. The AC field was applied at 0 s (snapshot A). The arrows in B, C and E indicate the buds. The scale bar in E corresponds to 10 µm. The graph represents the degree of the vesicle deformation. The time of UV and blue light irradiation is shown by the areas in violet and blue, respectively.

The MD simulations can also be used to predict the area increase when the molecules undergo *trans*-to-*cis* isomerization. A series of simulations of DOPC bilayer patches containing between 2 and 10 F-azo molecules symmetrically distributed in both leaflet (and corresponding to the range between 128 and 25 lipids per F-azo molecule) show a maximum area increase of $\Delta A \sim 1.6$ % when 10 F-azo molecules were added. Although the effect is smaller than the experimentally measured increase, it illustrates how the conformational change of the molecules can lead to the observed increase in the vesicle area. As the area increase in the experiments is seen to continue after seconds, the different magnitude of the observed effect may be related to the much smaller length and time scales in the simulated system.

3.3 Discussion

According to the area-difference-elasticity (ADE) model [26, 169, 170], the shape of a vesicle depends on two parameters. The first one is the effective spontaneous curvature [169, 171], which combines the local spontaneous curvature of the membrane with the non-local source of bending. The latter couples the area difference between the inner and the outer monolayer to the integrated mean curvature [172-174]. It should be noted that a vesicle can undergo outward budding when the spontaneous curvature, m_{sp}, is positive, while inward budding can occur at negative m_{sp}. The second parameter which determines the shape of a vesicle is the volume-to-area ratio, as defined by the reduced volume, ν. A schematic illustration of a partial morphological diagram of the vesicle shapes as a function of the reduced volume and the m_{sp} is shown in Fig. 3-10 (reproduced from [171]). For $\nu = 1$ the vesicle is a sphere. For $\nu < 1$ the vesicle has excess area available for shape transformation. The solid curve represents the boundary above which budding occur.

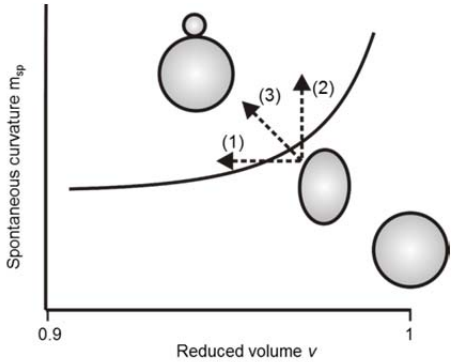

Fig.3-10. Schematic presentation of a part of the morphological diagram and possible pathways that the vesicle can take during the UV irradiation. The trajectories pointed with dashed arrows correspond to: (1) an increase of the vesicle area only (leading to a decrease in ν), (2) increasing the spontaneous curvature, m_{sp}, only, and (3) increasing both, the vesicle area and the spontaneous curvature.

Possible pathways, which the vesicles can take upon F-azo isomerization are represented by the trajectories in the morphological diagram (Fig. 3-10) as follow: (1) increase in the membrane area only (decrease in the reduced volume, $\nu < 1$) at a positive and constant m_{sp}, (2) only the membrane spontaneous curvature increase at constant reduced volume, whereby ν

$<$ 1, and (3) both the spontaneous curvature and vesicle area increase (the reduced volume decreases).

During our experiments with photo irradiation in the presence of F-azo, the GUVs did not lose their contrast (resulting from the difference in the refractive index between the interior and exterior solutions of the vesicles). This is a clear indication that the membrane remains intact and thus, the vesicle volume is constant. Image analysis of the vesicles before budding confirms that the volume remains constant (within the detection error of ± 1 pix). Therefore an increase in the vesicle area (which was detected, see 3.2.6 above) is the only source for changing the reduced volume. The observed vesicles undergo only outward budding transition in the presence of UV light and never inward budding, even if they exhibit significant excess area. This implies that the vesicles in the presence of F-azo are characterized by positive spontaneous curvature either before the UV light irradiation or they acquire this positive m_{sp} during the isomerization process.

We now discuss the possible source of positive spontaneous curvature. It is known that if the interior and the exterior solution contain the same molar concentration of two different molecule species, the membrane curves towards the solution with the smaller molecule size [175]. Accordingly, sugar distribution such as sucrose (larger molecule size than the glucose) inside the GUVs and glucose outside, as in our experiments, would induce a positive spontaneous curvature. We examined the influence of the sugar asymmetry on the spontaneous curvature using a custom-made microfluidic chamber. In these measurements, we examined vesicles grown either in sucrose (and diluted in glucose) or in glucose (and diluted in sucrose). Prior to the measurements, the GUVs were suspended in isotonic glucose or sucrose solution, respectively. During the experiments, the external solution of the respective sugar was exchanged with more concentrated solution of the same sugar using a microfluidic chamber, see section 3.1.7. Thus, an excess area in the vesicles was induced due to the efflux of water towards the more concentrated solution. Indeed, we observed outward budding (which indicates a positive m_{sp}) when the vesicles are grown in sucrose and diluted in higher concentrated solution of glucose (Fig. 3-11A), while inward buds and tubes (indicates a negative m_{sp}) were observed in the case of the opposite sugar distribution (Fig.3-11B).

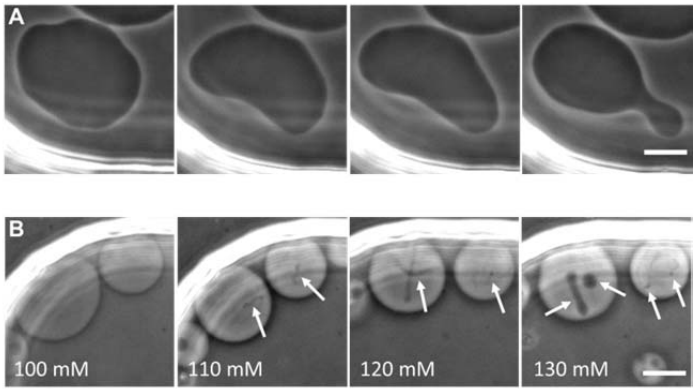

Fig. 3-11. Influence of the sugar asymmetry on the vesicle morphology. (A) GUVs grown in sucrose (100 mM) and diluted in glucose (100 mM). The glucose solution was exchanged. The presented image sequence is with 130 mM glucose solution. (B) GUVs grown in glucose (100 mM) and diluted in sucrose (100 mM). The sucrose solution was exchanged with solutions with different concentrations of sucrose (indicated in the lower left corner of the pictures). The white arrows point to the formed internal tubes and buds. The vesicles in both panels were observed 5-10 min after the exchange of the external solutions. The bright regions in the snapshots show the PDMS borders of the microfluidic chambers. The scale bars correspond to 15 µm.

In order to examine whether the sugar asymmetry (sucrose inside/glucose outside) is the sole source of the positive spontaneous curvature in our system, we investigated the influence of the F-azo isomerization on GUVs with inverted sugar distribution (glucose inside/sucrose outside). As shown in Fig. 3-11B, in the absence of F-azo, such sugar distribution causes the appearance of inward tubes, which indicates the generation of a negative spontaneous curvature. Thus, if F-azo does not have an effect on the membrane spontaneous curvature, the membrane area increase caused by the *cis* F-azo isomerization should induce inward budding. However, we again observed reversible outward budding (Fig.3-12) similar to the behavior when the vesicles were grown in sucrose and diluted in glucose (see Fig. 3-4). This suggests that the F-azo molecules induce a positive spontaneous curvature on their own, which dominates the curvature effects resulting from the sugars.

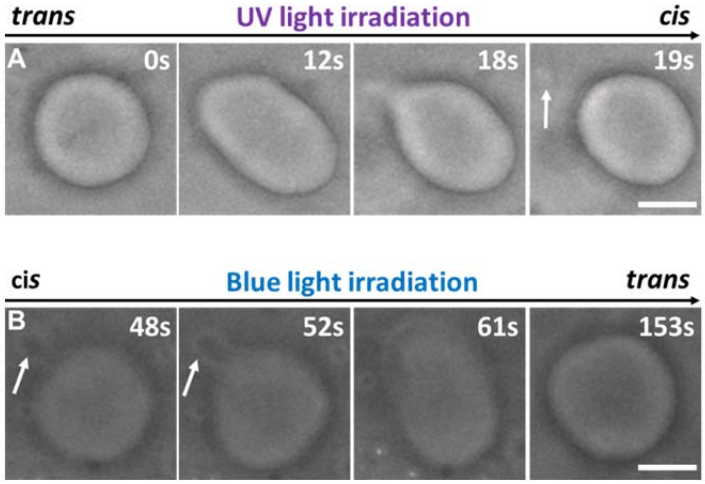

Fig. 3-12. Dynamic response of vesicles grown in glucose and diluted in sucrose to photoisomerisation of F-azo (0.25 mM). (A) Vesicle outward budding upon UV light irradiation (365 nM). (B) Re-adsorption of the expelled bud and restoring of the initial shape of the same vesicle upon blue light irradiation (470 nm). The arrows point to the expelled but. The scale bars correspond to 10 µm.

Figure 3-13 shows the possible molecular mechanisms for the observed changes in the vesicle shape in the presence of F-azo when the GUVs are exposed to UV light. These mechanisms are classified according to whether F-azo is symmetrically or asymmetrically distributed in the membrane and between the bulk in the vesicle interior and exterior. Fig.3-13A illustrates the scenario of an asymmetrical F-azo distribution in the membrane and a symmetrical one in the bulk outside and inside of the vesicle, while panel 3-13B shows an asymmetrical distribution of F-azo in the membrane and in the bulk. The last case (Fig. 13-3C) corresponds to a 'symmetrical' membrane and an 'asymmetrical' bulk. It should be noted that the F-azo aggregates are not illustrated (for clarity). They could be also asymmetrically distributed in/out of the vesicles and thus can be the source of a spontaneous curvature.

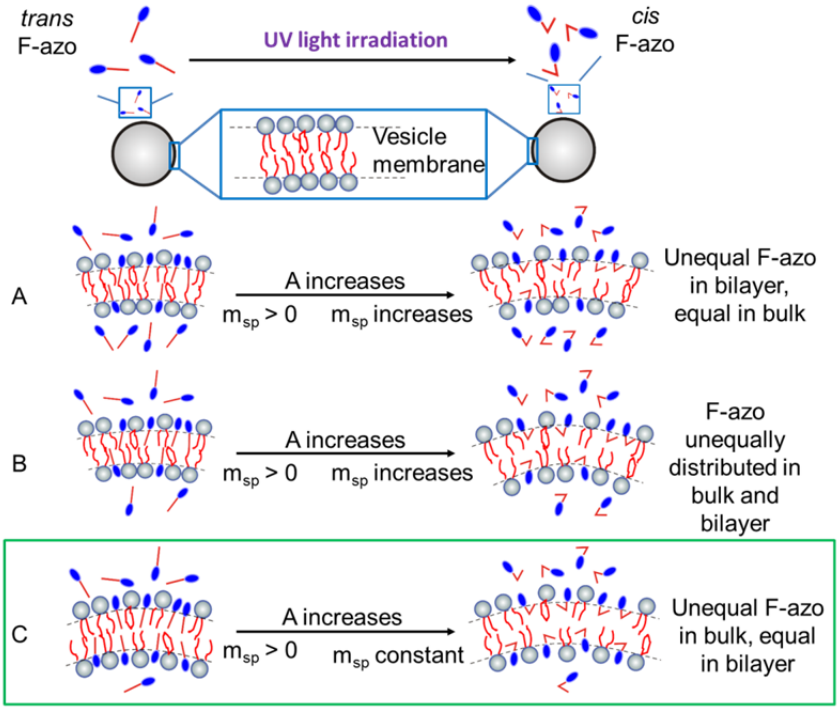

Fig. 3-13. Sketch of the mechanisms of the observed budding event at molecular level (A-C). A and m_{sp} represent the membrane area and the spontaneous curvature. The green box indicates the suggested mechanism.

It is known that both a larger number of molecules in the outer leaflet in respect to the inner one or an asymmetric distribution of molecules across the membrane (adhering of more particles on the outer leaflet than on the inner one) can be source of a positive spontaneous curvature [176]. Hence, in order to be able to induce a positive spontaneous curvature the F-azo molecules: i) are more in the outer leaflet compared to the inner one, before the UV light irradiation, ii) integrate in the outer leaflet when they isomerize from *trans*-to-*cis* upon UV light or iii) they (or their aggregates) are asymmetrically distributed across the membrane. However, the results from the MD simulations show that both F-azo forms have similar partitioning free energy, and thus insert into the lipid bilayer regardless of their conformation, and the molecules are equally distributed in the time scale of our measurement, due to the fast

flip-flop rate. The latter excludes the mechanisms proposed in panels A and B (Fig. 3-13), which include an unequal distribution of the molecules between both leaflets. Therefore, we suggest that the observed budding events occur due to an increase in the vesicle area, when there is an initial positive spontaneous curvature (which can also be induced by unequal distribution of the F-azo aggregates) as presented in Fig. 3-13C and pathway (1) in Fig. 3-10.

3.4 Conclusion

We have employed theoretical and experimental methods in order to probe crucial membrane properties, related to widely acknowledged cell processes such as endo- and exocytosis. We have observed reversible morphological changes in GUVs, in presence of photosensitive molecules, controlled by light. The isomerization of F-azo cause outward budding and reabsorption of the buds, depending on the molecules' conformation. We found that, due to *trans*-to-*cis* F-azo isomerization, the membrane area increase with ~ 5% and a positive local spontaneous curvature emerged. We have proposed a mechanism of the observed budding transition which includes both increasing in the membrane area and occurring of positive initial spontaneous curvature.

4 Light control of the lipid lateral organization

Lateral phase-separation of lipids into membrane domains is considered to sort proteins and thus to play a role in signaling cascades, apoptosis, protein transports and lipid regulation [177-179]. This lipid organization in immiscible liquid phases (liquid ordered or l_o and liquid disordered or l_d) is assumed to underlie in the formation of raft-like structures in cell membranes (see Chapter 1.6). The rafts are thought to be dynamic membrane entities in size of 10-100 nm, which are enriched in saturated long-chained lipids (e.g. SM, DPPC), cholesterol and proteins [180]. Recent reports have suggested that the driving forces in domain formation are the interfacial energy between the lipids, and the mixing entropy [181]. However, various challenges remain in understanding the organizing principles of lipid domains in cells. Even though an important progress on detection of domains in living cells has been recently reported [182], highly ordered and conserved lipid structures (lipid rafts) are hard to monitor in intact cells under physiological conditions even when employing high spatial and temporal resolution techniques [183]. In contrast, images of lipid domains have been directly observed in membrane model systems [184, 185]. Thus, simpler systems than a living cell have become an efficient tool in studying the nature of the lipid lateral organization.

Large, micron-scale domains can be directly observed in GUVs by fluorescence microscopy and thus the lipid lateral separation can be explored in a more controlled fashion than in cells. Changes in phase-separated domains, due to specific and non-specific molecular interactions, have been considerably studied in GUVs [77, 186-189]. Different strategies to initiate domain formation in simple three-component vesicles include varying the temperature or depleting the amount of cholesterol in the phospholipid bilayer by using β-cyclodextrin [80]. In addition it has been shown that the sterol structure affects the formation of l_o domains. In particular, decreasing the steroid ring planarity or increasing the head group size declines domain formation [190, 191]. Another strategy to alter the lipid phase-separation is to use non-lipid amphiphilic molecules. For instance, triton-X-100, increases the order of the l_o phase and thus leads to increase in the hydrophobic mismatch, which domain formation, while evolvesvitamin E decreases the lipid-lipid interfacial energy and promotes mixing of the lipids. [192]. Employing these approaches as a criterion for raft characterization can also exhibit several drawbacks. For instance, cholesterol plays various roles including regulation of membrane physical properties such as diffusion and thickness, which in turn can alter protein conformation and activity. Therefore, the depletion of cholesterol can disrupt [193, 194] the lipid compositional balance and affect proteins, and thus it is not sufficient to assert the role of lipid domains [195]. In addition, triton–X-100 is known to break lipid-lipid interactions, which alters the domain constituents.

Employing light is an elegant approach to modulate the lipid phase-separation in model membrane systems. Yasuhara et al. [196] observed for the first time altering of lipid domain structure by photoisomerization of azobenzene, attached to cholesterol (AzCh). In addition, they showed that the azobenzene moiety of AzCh can isomerize, upon UV light irradiation, in

both l_o and l_d phase. Since then, different strategies and photosensitive molecules have been used to tune the lateral lipid organization by light [197-199]. These studies, however, raised open questions concerning the mechanism of the lipid phase modulation using photoswitches and light.

Here, we use F-azo to examine the lipid domain disorganization. The latter is governed by the photoisomerization of F-azo upon UV light irradiation. The phase partitioning of the photoswitches was probed by monitoring the lateral diffusion of both l_d and l_o phase, and the bending rigidity of l_d in the presence of F-azo molecules (see 4.2.3 and 4.2.4). In addition, the miscibility transition temperature of phase-separated GUVs was found to be affected by the F-azo isomerization (see 4.2.2). It should be noted that some of the results in this chapter (specified in section 4.2) are preliminary. As indicated throughout this chapter, additional measurements will be performed to determine the significance of those results and the validity of the conclusions drawn here.

4.1 Methods

4.1.1 Preparation of multicomponent GUVs

Phase-separated vesicles were prepared by electroformation as described in Chapter 3.1.1 with the exception that a three component lipid composition was used, namely, mixtures of DOPC/DPPC/Chol in molar ratio (1:1:1) and (1:6:3) with 4 mM final lipid concentration. From now on we name both the 1:1:1 and the 1:6:3 mixtures, composition **A** and **B**, respectively (Fig. 4-1). Both mixtures contain 0.1 mol % fluorescent dye (DPPE-Rh). The vesicles were grown at 50°C (at which the lipids are fully miscible) and cooled down at room temperature.

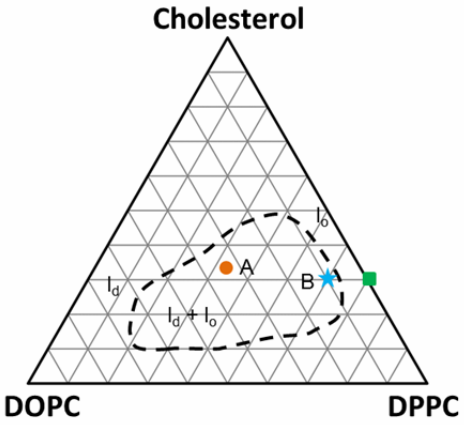

Fig.4-1. Location within the phase diagram of the different lipid compositions that were used. The orange circle represents the composition of 1:1:1 DOPC/DPPC/Chol molar ratio (composition **A**), while the blue star indicates the 1:6:3 composition (composition **B**). The green square represents the 7:3 DOPC/Chol composition used in the FRAP measurements. The dashed curve delineates the area of the l_d-l_o phase coexistence region at ~23°C reproduced from [80].

The same methodology, using different lipid compositions, was applied to prepare the vesicles for FRAP measurements. Two different batches of homogeneous GUVs in l_o and l_d phase, respectively, were prepared. However, in this case, the concentration of the DPPE-Rh was 0.5 mol % in order to increase the vesicle contrast. The vesicles in the l_o phase were composed of DPPC/Chol in molar ratio (7:3), while the l_d GUVs contain only DOPC (and DPPE-Rh).

4.1.2 Determination of the miscibility temperature of GUV membranes in the presence of F-azo before and after the photoisomerization

The measurements were performed in a custom-made chamber (see Fig. 4-2). The latter is connected to a water bath, in which the water is temperature controlled by a thermostat. The sample is placed between two glasses, which are separated by a 0.5 mm tick silicon spacer seen in Fig. 4-2A. This glass chamber is sandwiched from below by a metal frame fixing the sample chamber to a metal part housing the flowing temperature-modulated water from the water bath (Fig. 4-2A). The latter metal part has a window for illumination and transmission imaging of the sample (Fig. 4-2 B).

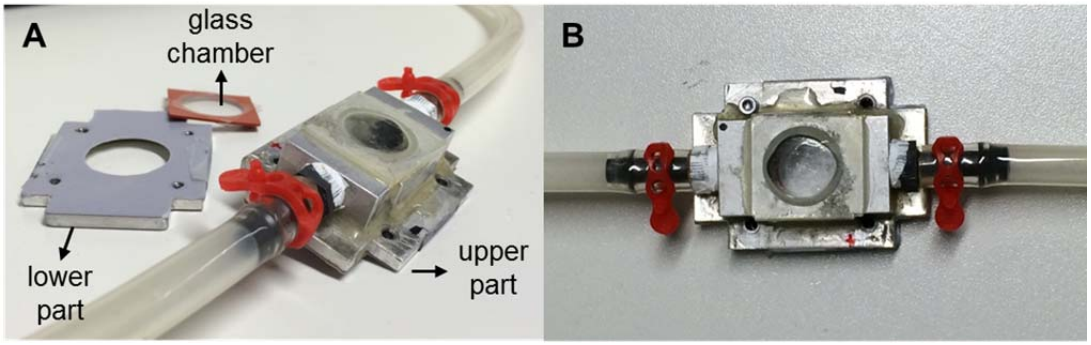

Fig. 4-2. Temperature control chamber. (A) Components of the custom-made chamber. The sample is placed between two coverslips separated by the red silicon spacer. From above (B) top view of the assembled chamber.

The vesicles were observed in epifluorescence mode on a Zeiss Axio Observer D1 microscope equipped with a 20x air objective with NA 0.5. Since all vesicles from both different lipid compositions were phase-separated at 10°C every measurement started at this temperature. The temperature was increased in 2°C steps and vesicles were left to equilibrate for 2-3 min before observation. The temperature was increased until all observed GUVs appeared homogeneous. Three independent batches of 30 vesicles at each temperature were analyzed. In the presence of F-azo (0.1 mM) the vesicles were analyzed both before and after the irradiation with UV light (lasted ~ 50-60 s). The data were fitted to the sigmoidal Boltzmann function:

$$y = \frac{A_1 - A_2}{1 + e^{T - T_{mix}/dT}} + A_2 \qquad (18)$$

Where, y, is the fraction of homogeneous GUVs, A_1 and A_2, the fraction at the lowest and the highest temperature, respectively, T, the temperature, and T_{mix}, the temperature at which half

of the vesicle population is homogeneous. A_1 and A_2 were fixed to 0 and 1, respectively. Once y reached 1 at a particular temperature, the value of y above this temperature was assumed to be 1.

4.1.3 Measuring the lateral lipid mobility in the presence of F-azo

The diffusion coefficient, D, in both l_d and l_o phase was measured by FRAP. The vesicles were diluted in a solution containing glucose and F-azo. The GUVs and F-azo molecules were incubated for 1-2 h. Then the vesicles were immobilized in agarose, similarly to the approach developed in [200]. Briefly, vesicles incubated with F-azo were mixed (in volume ratio 1:1) with melted agarose solution (0.25 % w/v agarose). Due to the agarose polymerization (during the cooling of the agarose) the vesicles are trapped in the network of the polymer. The final F-azo concentration is 0.5 mM.

The FRAP measurements were performed with a confocal microscope (Leica TSC SP5). These measurements were conducted either on the top or the bottom poles of ten GUVs in l_d phase, incubated with F-azo and then immobilized in agarose. The same measurement was performed also on ten vesicles in l_o phase. The same two measurements were repeated on F-azo-free GUVs. The fluorescent probe (DPPE-Rh) was excited with an argon laser at 561 nm. Images (256 x 256 pixels) were recorded in bidirectional scan mode at 1400 Hz and pinhole at 1 airy unit. Fifteen images at attenuated laser intensity (12%) were taken before the photobleaching. The photobleaching was performed using the argon 514 nm and 561 nm lasers at maximum intensity for 290 ms (3 frames) through a circular region of interest (ROI) of nominal radius r_n = 1.5 μm. The effective radius, r_e, was measured (see Chapter 2.5) to be 3.1 μm and 2.8 μm for composition **A** (the l_d phase) with and without F-azo, respectively. This difference already suggests faster diffusion in the presence of F-azo. For composition **B** (the l_o phase) r_e is 2.3 μm and 2.4 μm in the presence and the absence of F-azo, respectively. The laser was then switched back to attenuated intensity and the recovery images were recorded for several seconds. The diffusion coefficient for every vesicle was obtained from the collected data as described in Chapter 2.5.

4.1.4 Fluctuation analysis

The effect of F-azo on the bending rigidity, κ, of phospholipid bilayer was probed by examining the vesicle thermal fluctuations. GUVs composed only of DOPC were used as l_d vesicles. Vesicles in l_o phase, composed of DPPC/Chol (7:3), did not exhibit thermal fluctuations that are detectable and within the optical resolution of our system. Therefore, the bending rigidity of those vesicles was not accessible. GUVs grown in sucrose (100 mM) and diluted in equimolar solution of glucose were observed in phase-contrast mode on a Zeiss Axio Observer D1 microscope using a 40x air objective. We used a digital camera (sCMOS pco.edge) to record the images. The latter were acquired at a speed of 35 frames per second for 50-60 s. The exposure time of the camera was set to 200 μs. Between 1700 and 2100 images for each vesicle were analyzed following the methodology described in Chapter 2.6. The bending rigidities of vesicles incubated for 1-2 h with F-azo (0.1 mM) and F-azo-free

vesicles were extracted. In each of the cases, eight GUVs with no visible defects were analyzed.

4.2 Results

Domains in multicomponent, phase-separated GUVs can be visualized with fluorescence microscopy using fluorescent probes. In this work we used the probe DPPE-Rh, which is known to partition in the l_d domains [201], to selectively label the l_d phase in vesicles with l_o-l_d coexisting phases. Hence, the l_d and l_o domains in phase-separated vesicles are always represented in red and black, respectively, throughout this work.

4.2.1 Light-induced changes in the phase state of phase-separated GUVs

The effect of *trans*-to-*cis* F-azo isomerization on vesicles exhibiting immiscible l_d-l_o phases was examined for DOPC/DPPC/Chol in two different lipid molar ratios (1:1:1) and (1:6:3), composition **A** and **B**, respectively, see Fig. 4-1. Several reasons for the choice of the DOPC/DPPC/Chol, among several other available compositions, are pointed in Chapter 2.1. The GUVs preparation method gave good reproducibility in formation of phase-separated vesicles. After the preparation, the GUVs were left to equilibrate at room temperature for about 1 h and then were diluted in a glucose solution both with and without F-azo. The samples were observed before and after (~ 1 min) irradiation with UV light (365 nm) at room temperature (23°C).

Let's first consider the influence of the F-azo isomerization on GUVs made of composition **A**. Figure 4-3A shows fluorescent microscope images of phase-separated GUVs either in the absence of F-azo (upper panel in Fig. 4-3A) or incubated with F-azo (lower panel). In both cases circular l_o domains (dark) are observed surrounded by l_d phase before UV light irradiation. Visual effects on the domain organization (and in particular domain number and size) were not detected after UV light irradiation, when the F-azo was not present. This shows that the UV light itself does not visibly alter the l_d-l_o coexistence within the time scale of the irradiation. However, UV light irradiation of GUVs consisting of the same lipid composition but incubated with F-azo leads to appearance of new red domains (presumably in l_d phase), which have also a circular shape, within the dark domains (Fig. 4-3A lower panel).

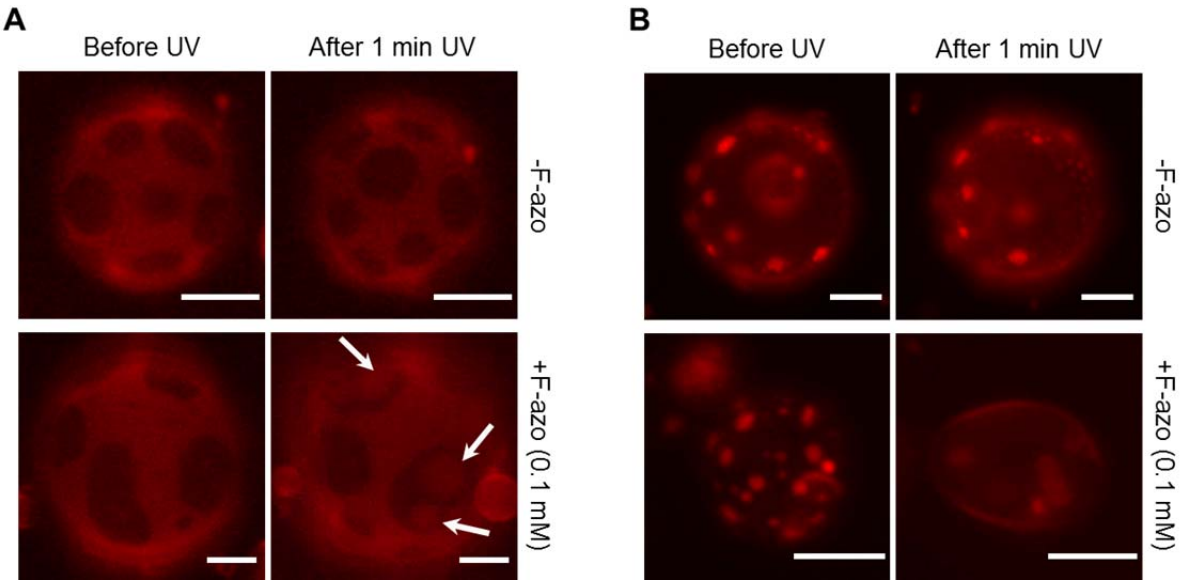

Fig.4-3. Fluorescence microscopy images acquired at room temperature (23°C) before and after UV light irradiation of phase-separated GUVs both with and without F-azo. (A) The GUVs are made of composition **A**, see Fig. 4-1. White arrows point to newly formed domains (red) within the l_o phase (dark). (B) Vesicles formed of composition **B**. All scale bars correspond to 10 µm.

Next, we examined the response of vesicles produced of composition **B** to the F-azo isomerization (Fig. 4-3B). Note that, compared to composition **A** this lipid composition is closer to the miscibility boundary, which separates the region of l_d-l_o phase coexistence from the region of full miscibility (see Fig. 4-1). The GUVs made of composition **B** also exhibits l_d-l_o phase coexistence, however, now the l_d domains are small and surrounded by the l_o phase. This increase in the area of the l_o phase relative to the l_d one is related to the increased amount of DPPC at the expense of DOPC in composition **B**. A similar behavior of the l_d and l_o phases in relation to the lipid composition was observed in [80]. Such behavior is described by the lever rule. According to the latter, the areas of the two coexisting phases are inversely proportional to the distances to the ends of a tie-line for a given composition. The UV light irradiation only, also does not disturb the structure of the domains, similar to the behavior of GUVs prepared from composition **A**. However, a different behavior was observed upon UV light irradiation of vesicles incubated with F-azo. The vesicles become homogeneous (Fig. 4-3B, lower panel). In the future, we consider performing measurements with decreased amount of the fluorescent dye in composition **B** since the dye gets highly concentrated in the small l_d domains and this might influence the membrane phase state. It was already shown above (see Chapter 1.5.2) that UV light can switch the F-azo's conformation from *trans*-to-*cis*. Hence, this conformational change destabilizes the lipid phase-separation and causes the observed effects.

4.2.2 Influence of F-azo conformation on miscibility temperatures in DPPC/DOPC/Chol membranes

We further tested the changes, which F-azo generates in the phase state of GUVs as characterized by the membrane miscibility temperature. Here, we show preliminary results of

the F-azo's effect on the miscibility temperature. We explored vesicles prepared from DOPC/DPPC/Chol in molar ratios 1:1:1 and 1:6:3 (composition **A** and **B**, respectively). The vesicles were grown in sucrose and diluted in a glucose solution, both in the presence and absence of F-azo (0.1 mM). Note that at this F-azo concentration, changes in the vesicle morphology and outward budding were not observed upon UV light within the time of the irradiation. After incubation for 1-2 h the GUVs were placed in the temperature control chamber (see Fig. 4-2). Due to the different densities of the sucrose and glucose solutions, the GUVs settle on the microscope glass, which allows an extended observation of the same vesicle population. In the case when UV light was applied, we irradiated a different vesicle population for each examined temperature in order to avoid oxidation of the fluorescent dye and thus altering the phase state of the membrane. Controls with vesicles grown from composition **B** in the absence of F-azo and upon UV light irradiation were also performed. These measurements (presented in Fig. 4.4) show that the UV light does not affect the miscibility temperature. Thus, we argue that no detectable compositional change occurs upon UV light irradiation. The same control measurements for vesicles formed of composition **A** are underway.

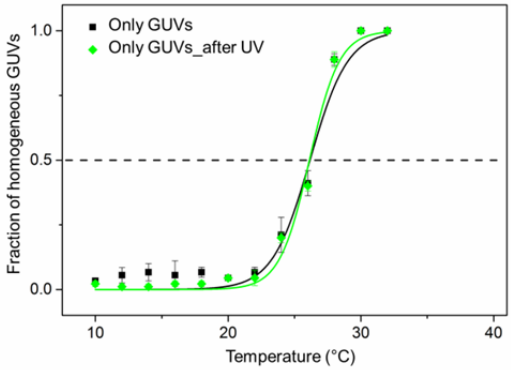

Fig.4-4. Effect of UV light on the miscibility transition temperature of vesicles made of composition **B**. The dashed line indicate T_{mix}, which was deduced from the Boltzmann model (eq. 18). Error bars correspond to standard error of mean of three measurements.

The miscibility transition temperature (at which half of the vesicles are homogeneous and the other half are phase-separated), T_{mix}, of composition **A**, as shown in Fig. 4-5A, is slightly influenced by the F-azo molecules. T_{mix} of vesicles incubated with F-azo (red triangles in Fig. 4-5A) was measured to be 29.0 ±0.2°C, which is by ~ 0.9 ±0.2°C lower compared to T_{mix} of F-azo-free GUVs (black squares). A similar shift in T_{mix} was observed when F-azo was present and the vesicles were irradiated with UV light (purple circles). This indicates that the conformation of the photoswitches does not alter the miscibility temperature of composition **A**. The latter agrees with the observed vesicle response to the isomerization of F-azo (Fig. 4-3A). Namely, the *trans*-to-*cis* switch in the molecule's conformation causes formation of new domains (assumed to be in l_d phase due to partitioning of the dye therein) within the l_o phase, however, the vesicles remain phase-separated. One could also expect that the area fraction of l_d domains in non-irradiated vesicles in the presence of F-azo is larger than that in F-azo-free vesicles. However, to probe the latter is not a trivial task because of the intrinsic heterogeneity in the composition of vesicles in the same batch as shown in Reference [82].

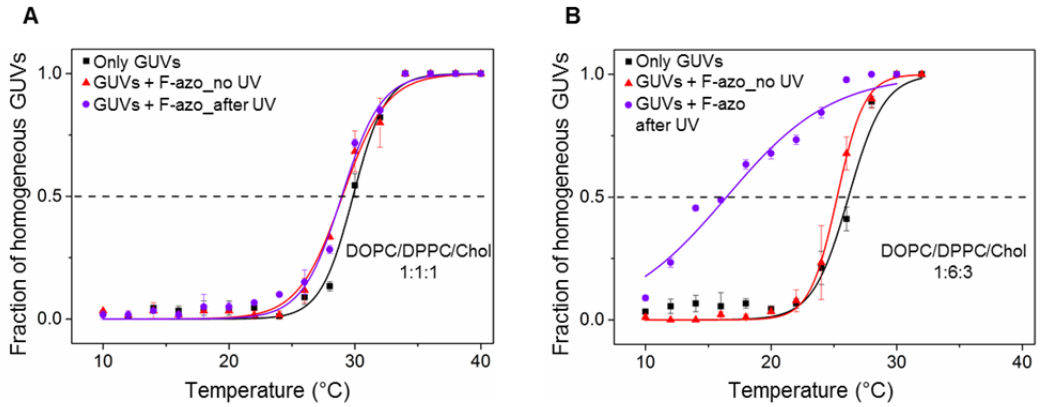

Fig.4-5. Miscibility transition curves of vesicles made of (A) composition **A** and (B) composition **B**. The F-azo concentration is 0.1 mM. The cross sections of the dashed lines with the curves indicate T_{mix}, which was deduced from the Boltzmann model (eq. 18). Error bars correspond to standard error of mean of three measurements.

In contrast, the vesicles grown from composition **B** exhibit a somewhat different behavior. The GUVs incubated with F-azo became homogeneous upon UV light irradiation (see Fig. 4-3B). This reflected in a considerable change in the miscibility temperature. Note that the miscibility temperature T_{mix} of the F-azo-free vesicles formed from composition **B** (black squares in Fig. 4-5B) appeared to be lower than T_{mix} of the F-azo-free GUVs grown from composition **A** (black squares in Fig. 4-5A), even though composition **B** is characterized by a higher fraction of DPPC. These measurements will be repeated using fresh lipid stocks to examine the significance of the determined T_{mix} of both F-azo-free and F-azo-incubated GUVs made of composition **B**. Fig. 4-5B shows the effect of F-azo on the miscibility transition temperature of vesicles consisting of composition **B**. T_{mix} of GUVs incubated with F-azo decreases by ~ 0.9 ±0.2°C compared to T_{mix} of vesicles without F-azo, as in the case of composition **A**. However, a large change in the miscibility temperature was detected in composition **B** as a result of the *trans*-to-*cis* F-azo isomerization. T_{mix} decreased by ~ 9.7 ±0.4°C upon UV light irradiation in the presence of F-azo in contrast to the T_{mix} of the vesicles without F-azo. These results indicate that the *cis* form of the F-azo conformation, caused by UV light irradiation, favors the mixing of the domains in l_d and l_o phase in composition **B**.

4.2.3 Diffusion coefficient of l_d and l_o phase in the presence of *trans* F-azo

We performed FRAP on vesicles in both l_d and l_o phase to explore the partitioning of F-azo between both liquid phases. The photobleaching was always performed on regions located on the vesicles poles. It should be noted that the method used for determination of the diffusion coefficient considers the diffusion of the lipids during the photobleaching step (see Chapter 2.5). Thus no other corrections are used. In order to reduce artifacts in the FRAP measurement caused by the GUVs displacement in the aqueous solution we immobilized the vesicles in an agarose gel. Vesicles composed of both DOPC (considered as vesicles in l_d phase) and DPPC/Chol in molar ratio 7:3, incubated in either F-azo-free or F-azo containing glucose solution, were mixed with 'melted' agarose. As reported in Lira et al. [200], after the

gelation of the agarose the vesicles are caged in the pockets of the gel network and importantly, the agarose does not affect the lateral lipid diffusion in the caged vesicles. Since the l_o phase was previously described as a state enriched in high temperature melting lipids and cholesterol [202] the membrane of GUVs made of the DPPC/Chol mixture is in the l_o phase. It should be noted that the F-azo was not irradiated with UV light neither before nor during the measurements, hence the molecules are in their *trans* form.

Figure 4-6 shows examples for recovery curves of l_d and l_o vesicles both with and without F-azo. The fluorescence in the l_d vesicles recovers fully within ~ 5 s after the photobleaching, while the one in the GUVs in l_o phase recovers slower (~ 30 s).This agrees with the reported in the literature reduced lipid mobility in the l_o phase [203]. The fluorescence recovery in the l_d phase is faster than in the l_o phase regardless of the presence of F-azo. The F-azo molecules, however, alter the time for fluorescence recovery of the membrane in l_d phase but did not show influence on the recovery time of the l_o phase. Data for two vesicles in l_d phase both with and without F-azo are presented in Fig. 4-6A. The half-time of full recovery, $t_{1/2}$, when F-azo is present is ~ 0.20 s, while without the molecules $t_{1/2}$ is ~ 0.30 s for those two particular GUVs with an standard error of ±0.01 s from two measurements. In contrast, two identical half-recovery times (1. 27 and 1.28 ±0.13 s) were measured for a l_o vesicle containing F-azo and a l_o GUV without F-azo (Fig. 4-6B). Note that the fluorescence intensity of the l_d phase looks almost recovered even on the first image after the photobleaching (the two snapshots at 0 s on Fig. 4-6A). We used the measured $t_{1/2}$ for each vesicle to extract the diffusion coefficient (see eq. 7 in Chapter 2.5). For the vesicles in l_d phase (Fig. 4-6A) the diffusion coefficients without and with F-azo are 4.18 ±0.41 $\mu m^2/s$ and 7.22 ±041 $\mu m^2/s$, respectively. In comparison, the diffusion coefficients of the vesicles in l_o phase, shown in Fig. 4-6B, are 0.78 $\mu m^2/s$ without F-azo and 0.77 $\mu m^2/s$ in the presence of the molecules with a standard error of ±0.07 $\mu m^2/s$ from two measurements.

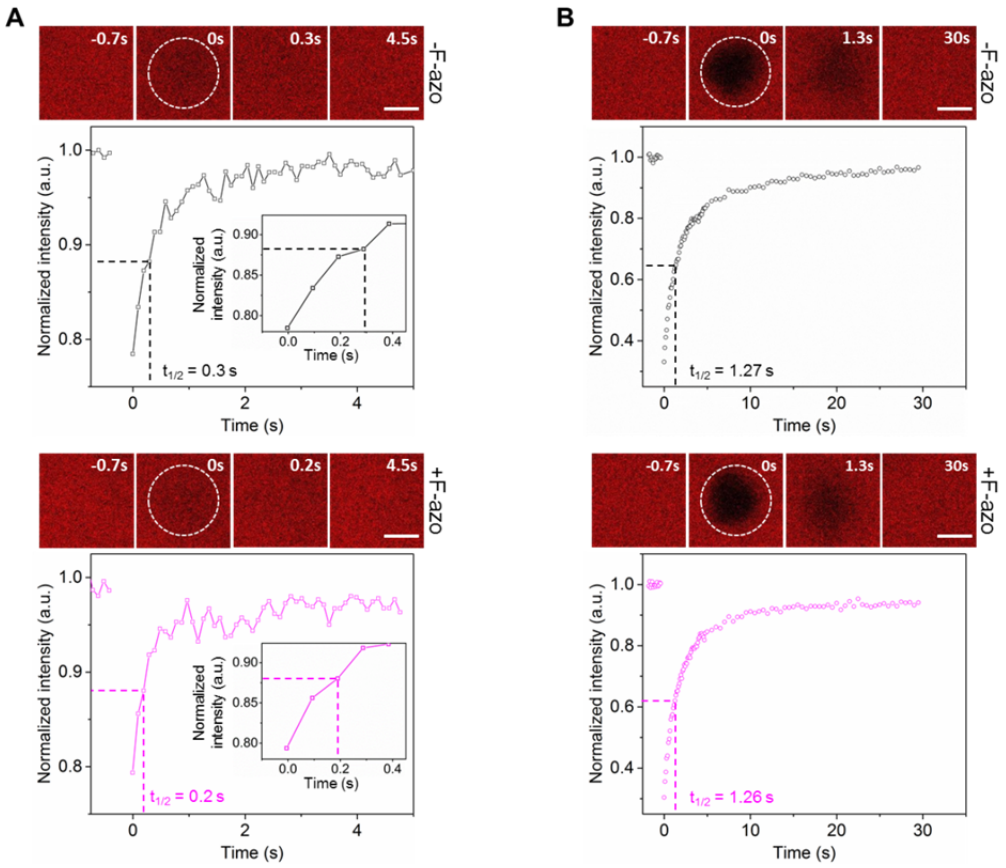

Fig.4-6. Fluorescence intensity recovery curves after photobleaching without (upper panels) and with F-azo (lower panels). The snapshots are confocal images (acquired at the top part of the GUVs) of the vesicle region where the FRAP measurement is performed. The images at t = 0 s correspond to the first picture taken after the photobleaching, while the dashed circles represent the bleached area. The scale bars correspond to 2 µm. (A) GUVs (made of DOPC only) in l_d phase. The insets in the graphs show the fluorescence recovery during the first 0.4 s. (B) Intensity recovery of GUVs (made of 7:3 DPPC/Chol) in l_o phase. The half-recovery time is defined in relation to the final fluorescence intensity.

Figure 4-7 shows the diffusion coefficients of 10 vesicles in the l_d phase incubated with F-azo and 10 vesicles in l_d phase without F-azo, and the same number of GUVs in the l_o phase also in the presence and absence of F-azo. The average diffusion coefficient, D_{av}, for the vesicles in l_d phase without F-azo is 5.57 ±1.28 µm^2/s, while in the presence of F-azo D_{av} = 7.36 ±1.29 µm^2/s. In comparison, D_{av} for the vesicles in l_o phase without and with F-azo is 0.79 ±0.20 µm^2/s and 0.75 ±0.15 µm^2/s, respectively.

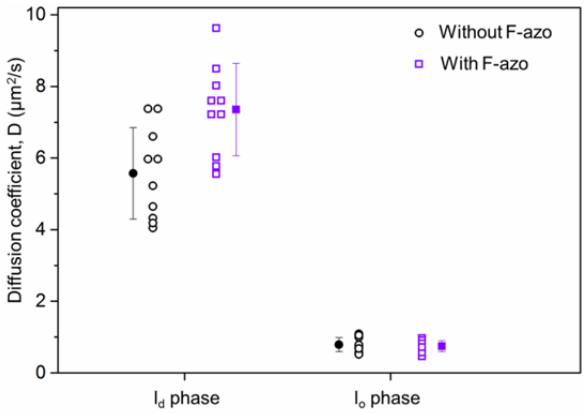

Fig.4-7. Effect of F-azo molecules on the lateral lipid diffusion in both l_d (only DOPC) and l_o (7:3 DPPC/Chol) phase. The concentration of the F-azo molecules is 0.5 mM. Each point represents a single measurement on an individual vesicle. The solid symbols and the bars correspond to mean values and standard deviation, respectively.

These results show that the *trans* F-azo increases the lipid lateral mobility of bilayers in the l_d state and does not alter the mobility in l_o membranes. The latter indicates that F-azo molecules either do not integrate in the l_o phase or they do integrate but this does not perturb the lipid mobility. To further investigate whether the F-azo molecules partition differently in the two membrane compositions explored, we will employ the size exclusion chromatography approach, used to determine the F-azo's insertion in DOPC membranes (see Chapter 3.1.6). Presumably, MD simulations would also be able to show how F-azo partitions between the l_d and the l_o phase.

4.2.4 Effect of F-azo on the bending stiffness of the membrane

We assessed the influence of F-azo on the membrane bending rigidity employing fluctuation spectroscopy on the same lipid compositions used for the FRAP measurements. GUVs made of DOPC were incubated with F-azo (0.1 mM) for ~ 1-2 h before performing the measurement. Vesicles exhibiting thermal fluctuations were recorded for ~ 1 min, yielding ~ 2000 frames. The bending rigidity, κ, was extracted from the vesicle shape fluctuations as described in Chapter 2.6. In total, eight vesicles without visual defects were analyzed. The same was done for eight F-azo-free GUVs (diluted in an F-azo-free solution). As mentioned above (see 4.1.4) we were not able to measure κ when the GUVs are composed of DPPC/Chol (7:3) due to the higher stiffness of the vesicles. Thus, we could not compare the F-azo influence on the bending rigidity of the l_o phase with the one on the l_d phase

We found that the F-azo molecules decrease the bending rigidity of the bilayer (Fig. 4-8). The average κ of the F-azo-free vesicles was measured to be 30.4 ±6.1 k_BT. In comparison, the average κ of the vesicles incubated with F-azo decreases to 20.7 ±3.6 k_BT. These results correlate with the measured increase in the lipid lateral mobility of membranes in l_d phase (see 4.2.3).

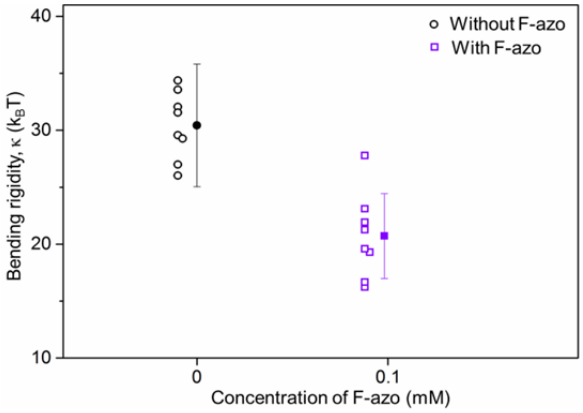

Fig.4-8. Bending rigidity of vesicles made of DOPC incubated with and without F-azo measured at room (23°C) temperature. Each point represents a single measurement on an individual vesicle. The filled points and the bars correspond to mean values and standard deviation, respectively.

4.3 Discussion

We have observed changes in the lipid domain structure of GUVs caused by *trans*-to-*cis* photoisomerization of F-azo molecules. Namely, formation of l_d domains within the l_o phase was noticed in phase-separated vesicles made of composition **A** (1:1:1 DOPC/DPPC/Chol), while the domains disappear and the vesicles become homogeneous for membranes of composition **B** (1:6:3 DOPC/DPPC/Chol), see Fig. 4-3. It is known that the energetic cost, caused by both the hydrophobic mismatch and steric interactions at the phase interface, together with the membrane curvature govern the stability of two coexisting lipid phases [204-206]. The energetic cost depends on the perimeter of the phase boundary. This effect is called line tension. The latter decreases when approaching the critical point of coexisting phases [207]. Accordingly, elevating the hydrophobic mismatch would lead to an increase in the line tension, resulting in stabilizing domains. Vice versa, lowering the hydrophobic mismatch and thus the line tension will promote mixing of the phases.

Hamada et al. investigated the influence of photoisomerization of an amphiphilic molecule (an azobenzene derivative with hydrophobic moieties), which partitions in the l_d phase, on both phase-separated and homogeneous multicomponent GUVs [198]. In phase-separated vesicles, made of lipid mixture close to the binodal facing the l_d phase, they observed the appearance of additional l_d domains in the l_o phase and the formation of l_o domains within the l_d phase due to *cis* isomerization of the molecule, while the latter induced phase-separation in one-phase vesicles. They proposed that the *cis* form of the molecules further increases the disorder of the l_d phase, resulting in increase of the hydrophobic mismatch and thus forming domains. Interestingly, we did not observe the appearance of l_o domains within the l_d phase in composition **A**, but the opposite only, after switching the F-azo molecules to *cis* form. It should be noted, however, that composition **A** is not as close to the binodal as the lipid mixture used in [198]. Similar to our results were observed in response to *cis* isomerization of azobenzene-modified cholesterol, enriched in the l_o phase [196]. The observed effects were assigned to a decrease in the packing of the l_o phase due to *cis* isomerization of the molecules and thus making the l_o domains more fluid. Hence, considering the results reported in [196,

198] and the observed formation of l_d domains within the l_o phase in response to F-azo's isomerization in composition **A**, we speculate that the *cis* F-azo isomer increases the disorder in the l_o phase in vesicles formed from composition **A**. Accordingly, the more oreder-disturbing *cis* F-azo (due to its larger area of occupancy than the *trans* form) would lead to changes in the molecular packing. Thus, a hydrophobic mismatch between the disturbed and non-disturbed lipids occurs. This mismatch could drive the formation of l_d domains within the l_o phase (Fig. 4.9A). Note that this mechanism is possible if F-azo inserts also in the l_o phase.

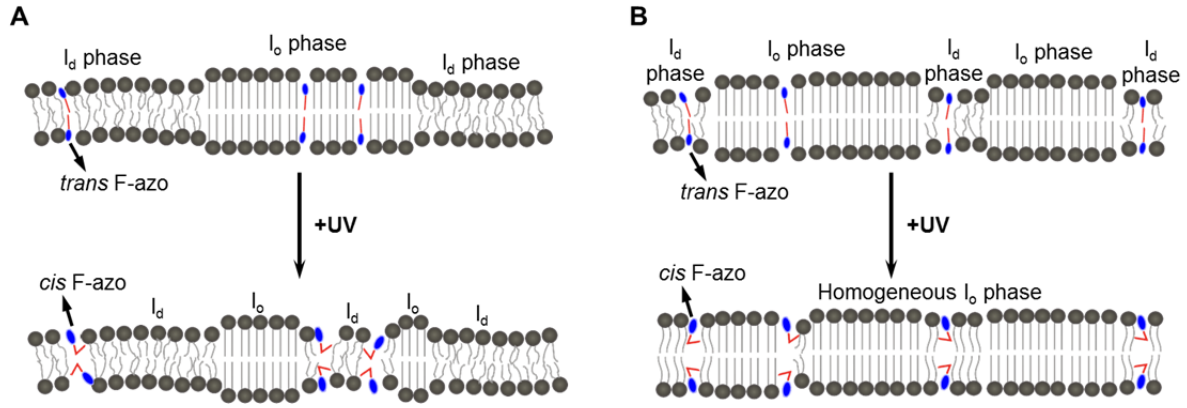

Fig.4-9. Schematic representation of F-azo isomerization in phase-separated membranes. (A) Membrane composed of 1:1:1 DOPC/DPPC/Chol (composition **A**). The *cis* form of F-azo perturbs the lipid order of the l_o phase, resulting in formation of l_d domains within the l_o phase. (B) shows the scenario for the 1:6:3 DOPC/DPPC/Chol membrane (composition **B**), where increase of the lipid order in the l_d phase (by the *cis* F-azo) and thus mixing of both phases is presumed (see the main text). The cholesterol and the DPPE-Rh are not illustrated for clarity.

In composition **B**, we observed full mixing of both phases upon UV light irradiation in the presence of F-azo. Since composition **B** is close to the binodal on the right side of the phase coexisting region (see Fig. 4-1), it is likely that the lipid organization is shifted to the right, towards the single l_o phase. Thus, in order to induce this shift, the *cis* F-azo should increase the order in the l_d phase, which will decrease the hydrophobic mismatch and lead to mixing with the l_o phase (Fig. 4-9B). However, this effect of the F-azo isomerization is different from the one observed in composition **A**. We observed a decrease in the ordering of the l_o phase and an increase in the l_d phase for compositions **A** and **B**, respectively. By the difference in the behavior of the two compositions, as shown in Figs. 4-3 and 4-5, we speculate that they do not belong to the same tie line (hence, the composition of the domains varies in the lipid mixtures used) as the l_o and l_d domains in the different membrane compositions appear to behave differently. Therefore, the effect of the *cis* F-azo form might vary between different compositions. Additionally, the F-azo's integration in the bilayer could dilute the lipid molecules and in this way change their intermolecular cohesion or simply change the local composition in terms of density of certain molecules. However, it remains to be tested what the partitioning of F-azo in the two membrane compositions (A and B) and the respective phases is.

4.4 Conclusion

We demonstrate that the lipid lateral organization of phase separated membrane in GUVs can be altered through the photoresponsive function of an anionic azobenzene molecule (F-azo). The effect of the F-azo isomerization on the phase coexistence depends on the specific membrane composition. This is, mixing of the l_d-l_o phases in a lipid composition, which is near the one phase boundary, and appearance of new l_d domains within the l_o phase. Our results indicate that the F-azo potentially affects the surface tension originated from interactions at the two-phase boundary. We discussed the mechanism of the observed photo-induced changes in the membrane phase separation in manner of changing the hydrophobic mismatch between the l_d and the l_o phase. To our knowledge, we observed for first time a profound alteration in laterally organized lipid structures caused by non-lipidated photosensitive molecule. Further studies are needed to investigate the partitioning of F-azo between the l_d and l_o phases as well as between the used lipid compositions, in order to obtain more detailed picture of the mechanisms of the observed phenomena. Also, it is appealing to study whether F-azo can influence the degree of lipid saturation in cell membranes. As such, this tool may contribute to a better understanding of plasma membrane 'rafts' and be used in targeting specific phase changes in the membrane.

5 Summary and outlook

In the present work, we studied the impact of photosensitive, anionic molecules, namely F-azo, on single- and multicomponent GUVs. In the first part of the thesis, we observed reversible *exo*-budding of single component vesicles. This was in response to isomerization of F-azo induced by UV and blue light irradiation. Two effects of the F-azo molecules on the membrane were characterized: We observed that the *trans*-to-*cis* F-azo's isomerization increases the area per lipid. Additionally, we saw that the photoswitches induce a positive spontaneous curvature in the membrane. Those two effects led invariably to outward budding events. In the next chapter, we show that the *cis* form of the photoswitches alter the lipid lateral organization in multicomponent, phase-separated vesicles. Here, we found that the F-azo's isomerization induces two different pathways of domain transformation, dependent on the lipid composition. One is disorganization in the l_o phase, which led to appearance of l_d domains within the l_o phase in GUVs consisting of equimolar lipid composition. The other is the hindrance of the phase-separation and promoting phase mixing in vesicles made of non-equimolar, close to the phase boundary lipid mixture. The molecule explored throughout the thesis, F-azo, in combination with GUVs has the potential to act as a platform for modeling complex cellular processes.

Appendix

Light-triggered bursting of giant unilamellar vesicles

A1 Photosensitive molecules

We have used azobenzene-containing-trimethyl-ammonium bromide (C_4-Azo-OC_nTMAB) as photo-responsive molecules, provided by S. Santer's group (University of Potsdam, Germany). Two types of molecules, in respect to the length of the alkyl spacer between the head group and the azobenzene moiety (see Fig. A-1A), were implemented in this study, namely, molecules with butyl (C_4-Azo-OC_4TMAB) and hexyl (C_4-Azo-OC_6TMAB) spacers. In the dark, the molecules are in *trans* conformation, since the latter is thermodynamically favorable. The azobenzene can be switched between *trans* and *cis* forms upon UV and blue light irradiation (Fig. A-1B) [208]. The UV-visible absorption spectrum of C_4-Azo-OC_6TMAB is shown in Fig. A-1C.

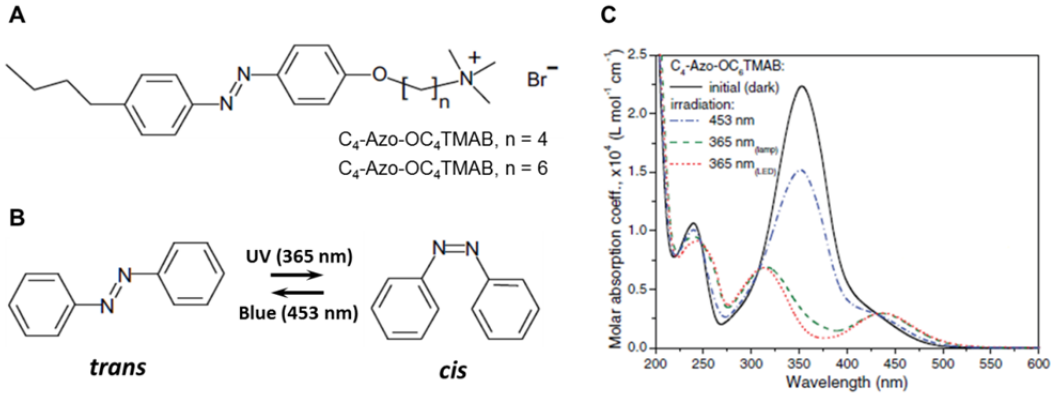

Fig. A-1. Structure and isomerization of the used molecules. (A) Chemical structure of both photoswitches. (B) Isomerization of the azobenzene molecules. (C) Absorption spectrum of C_4-Azo-OC_6TMAB. The structures and the spectrum are adopted from [208].

A2 Bursting of giant unilamellar vesicles in response to *cis* isomerization of C_4-Azo-OC_nTMAB molecules

The giant unilamellar vesicles (GUVs) were prepared by electroformation, as described in Chapter 2.2. The photosensitive molecules (with the desired concentration) were incubated with the vesicles after the formation of the GUVs. Both the observation and the irradiation of the vesicles were performed as in the case of implementing the F-azo molecules (see Chapter 3.1). We observed vesicle bursting in the presence of both TMAB molecules (in concentrations as low as 0.05 mM) upon UV light. Fig. A-2 shows bursting of GUVs incubated with 0.5 mM solution of C_4-Azo-OC_4TMAB. The mechanism of the membrane rupturing includes pore formation, as observed in Fig. A-2B. The pore initiation occurs within the first 10 ms of the UV light irradiation.

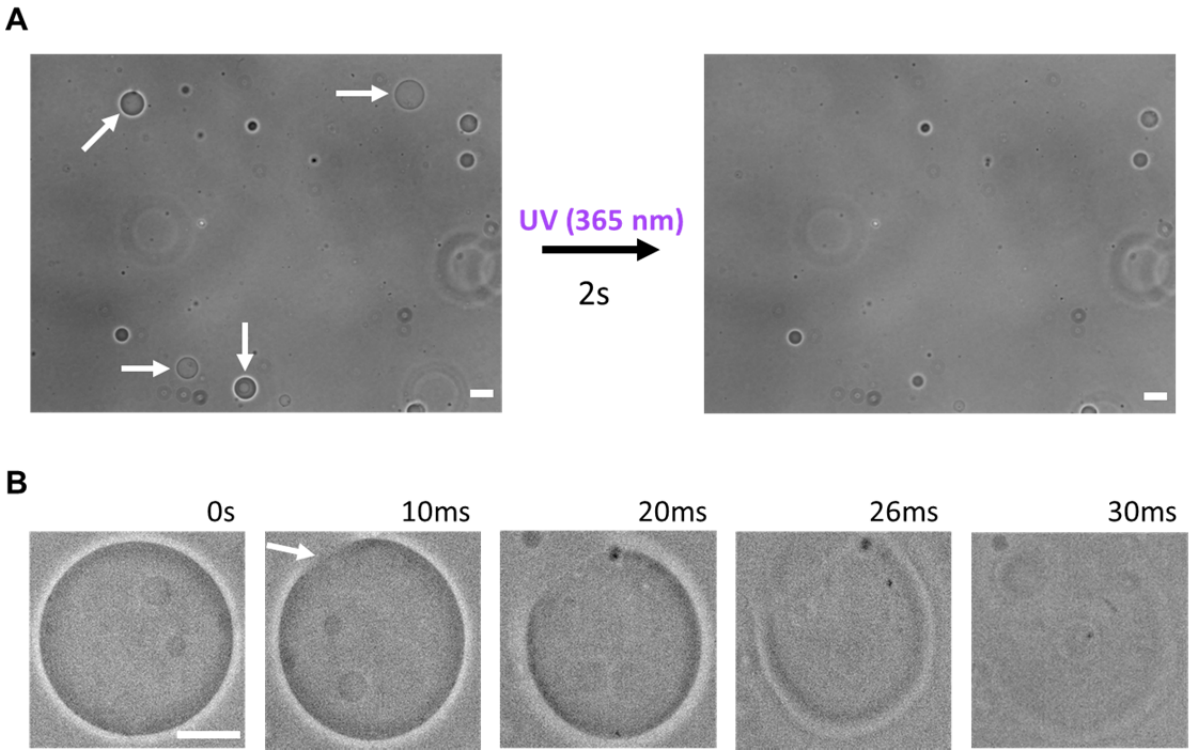

Fig. A-2. Light-induced bursting of GUVs in the presence of C_4-Azo-OC_4TMAB. (A) Phase-contrast microscopy images of GUVs before (left panel) and after (right panel) UV light irradiation. The concentration of the photosensitive molecules is 0.5 mM. The arrows of the left panel point the vesicles which bursted upon UV light. (B) Time-lapse observation of bursting of an individual vesicle. The arrow in the second snapshot indicates the formed pore. The scale bars correspond to 20 µm.

Bibliography

1. Yeung, T., et al., *Membrane phosphatidylserine regulates surface charge and protein localization.* Science, 2008. **319**(5860): p. 210-213.

2. Lodish, H., et al, *Molecular cell biology*, ed. 5th. 2003, New York: W. H. Freeman.

3. Pan, J.J., S. Tristram-Nagle, and J.F. Nagle, *Effect of cholesterol on structural and mechanical properties of membranes depends on lipid chain saturation.* Physical Review E, 2009. **80**(2).

4. Rawicz, W., et al., *Elasticity, strength, and water permeability of bilayers that contain raft microdomain-forming lipids.* Biophysical Journal, 2008. **94**(12): p. 4725-4736.

5. Gracià, R.S., et al., *Effect of cholesterol on the rigidity of saturated and unsaturated membranes: fluctuation and electrodeformation analysis of giant vesicles.* Soft Matter, 2010. **6**(7): p. 1472.

6. Oradd, G., V. Shahedi, and G. Lindblom, *Effect of sterol structure on the bending rigidity of lipid membranes: A H-2 NMR transverse relaxation study.* Biochimica Et Biophysica Acta-Biomembranes, 2009. **1788**(9): p. 1762-1771.

7. Israelachvili, J.N., *Intermolecular and Surface Forces, 3rd Edition.* Intermolecular and Surface Forces, 3rd Edition, 2011: p. 1-674.

8. Smith, R. and C. Tanford, *Critical Micelle Concentration of L-Alpha-Dipalmitoylphosphatidylcholine in Water and Water/Methanol Solutions.* Journal of Molecular Biology, 1972. **67**(1): p. 75-&.

9. Gruner, S.M., et al., *Lipid Polymorphism - the Molecular-Basis of Nonbilayer Phases.* Annual Review of Biophysics and Biophysical Chemistry, 1985. **14**: p. 211-238.

10. Israelachvili, J.N., D.J. Mitchell, and B.W. Ninham, *Theory of Self-Assembly of Hydrocarbon Amphiphiles into Micelles and Bilayers.* Journal of the Chemical Society-Faraday Transactions Ii, 1976. **72**: p. 1525-1568.

11. Cullis, P.R. and B. Dekruijff, *Lipid Polymorphism and the Functional Roles of Lipids in Biological-Membranes.* Biochimica Et Biophysica Acta, 1979. **559**(4): p. 399-420.

12. Cullis, P.R., Hope, M. J., *Biochemistry of Lipids and Membranes*. 1985, Benjamin Cummings: Menlo Park.

13. Chernomordik, L., M.M. Kozlov, and J. Zimmerberg, *Lipids in Biological Membrane-Fusion.* Journal of Membrane Biology, 1995. **146**(1): p. 1-14.

14. Hui, S.W., *Ultrastructural Studies of the Molecular Assembly in Biomembranes - Diversity and Similarity.* Current Topics in Membranes and Transport, 1987. **29**: p. 29-70.

15. Brezesinski, G. and H. Mohwald, *Langmuir monolayers to study interactions at model membrane surfaces.* Advances in Colloid and Interface Science, 2003. **100**: p. 563-584.

16. Mcconnell, H.M., *Structures and Transitions in Lipid Monolayers at the Air-Water-Interface.* Annual Review of Physical Chemistry, 1991. **42**: p. 171-195.

17. Akashi, K., et al., *Preparation of giant liposomes in physiological conditions and their characterization under an optical microscope.* Biophysical Journal, 1996. **71**(6): p. 3242-3250.

18. Angelova, M.I. and D.S. Dimitrov, *Liposome Electroformation.* Faraday Discussions, 1986. **81**: p. 303-+.

19. Walde, P., et al., *Giant Vesicles: Preparations and Applications.* Chembiochem, 2010. **11**(7): p. 848-865.

20. Angelova, M.I., N. Hristova, and I. Tsoneva, *DNA-induced endocytosis upon local microinjection to giant unilamellar cationic vesicles.* European Biophysics Journal with Biophysics Letters, 1999. **28**(2): p. 142-150.

21. Feigenson, G.W. and J.T. Buboltz, *Ternary phase diagram of dipalmitoyl-PC/dilauroyl-PC/cholesterol: Nanoscopic domain formation driven by cholesterol.* Biophysical Journal, 2001. **80**(6): p. 2775-2788.

22. Scherfeld, D., N. Kahya, and P. Schwille, *Lipid dynamics and domain formation in model membranes composed of ternary mixtures of unsaturated and saturated phosphatidylcholines and cholesterol.* Biophysical Journal, 2003. **85**(6): p. 3758-3768.

23. Pike, L.J., *Rafts defined: a report on the Keystone Symposium on Lipid Rafts and Cell Function.* Journal of Lipid Research, 2006. **47**(7): p. 1597-1598.

24. Cottingham, K., *Do you believe in lipid rafts?* Analytical Chemistry, 2004. **76**(21): p. 403a-406a.

25. Lyubartsev, A.P. and A.L. Rabinovich, *Recent development in computer simulations of lipid bilayers.* Soft Matter, 2011. **7**(1): p. 25-39.

26. Seifert, U., *Configurations of fluid membranes and vesicles.* Advances in Physics, 1997. **46**(1): p. 13-137.

27. Dimova, R., et al., *A practical guide to giant vesicles. Probing the membrane nanoregime via optical microscopy.* Journal of Physics-Condensed Matter, 2006. **18**(28): p. S1151-S1176.

28. Helfrich, W., *Elastic Properties of Lipid Bilayers - Theory and Possible Experiments.* Zeitschrift Fur Naturforschung C-a Journal of Biosciences, 1973. **C 28**(11-1): p. 693-703.

29. Mohandas, N. and E. Evans, *Mechanical-Properties of the Red-Cell Membrane in Relation to Molecular-Structure and Genetic-Defects.* Annual Review of Biophysics and Biomolecular Structure, 1994. **23**: p. 787-818.

30. Seifert, U., Lipowsky, R., *Handbook of biological physics*. 1 ed. Morphology of vesicles. 1995.

31. Haluska, C.K., et al., *Giant hexagonal superstructures in diblock-copolymer membranes.* Physical Review Letters, 2002. **89**(23).

32. Lipowsky, R., *The Conformation of Membranes.* Nature, 1991. **349**(6309): p. 475-481.

33. Mutz, M. and D. Bensimon, *Observation of Toroidal Vesicles.* Physical Review A, 1991. **43**(8): p. 4525-4527.

34. Dobereiner, H.G., *Properties of giant vesicles.* Current Opinion in Colloid & Interface Science, 2000. **5**(3-4): p. 256-263.

35. Guo, L., et al., *Molecular diffusion measurement in lipid Bilayers over wide concentration ranges: A comparative study.* Chemphyschem, 2008. **9**(5): p. 721-728.

36. Monzel, C., et al., *Measuring fast stochastic displacements of bio-membranes with dynamic optical displacement spectroscopy.* Nature Communications, 2015. **6**.

37. Veatch, S.L., et al., *Critical fluctuations in plasma membrane vesicles.* Acs Chemical Biology, 2008. **3**(5): p. 287-293.

38. Henriksen, J., A.C. Rowat, and J.H. Ipsen, *Vesicle fluctuation analysis of the effects of sterols on membrane bending rigidity.* European Biophysics Journal with Biophysics Letters, 2004. **33**(8): p. 732-741.

39. Pecreaux, J., et al., *Refined contour analysis of giant unilamellar vesicles.* European Physical Journal E, 2004. **13**(3): p. 277-290.

40. Dimova, R., et al., *Vesicles in electric fields: Some novel aspects of membrane behavior.* Soft Matter, 2009. **5**(17): p. 3201-3212.

41. Dimova, R., et al., *Giant vesicles in electric fields.* Soft Matter, 2007. **3**(7): p. 817-827.

42. Riske, K.A. and R. Dimova, *Electro-deformation and poration of giant vesicles viewed with high temporal resolution.* Biophys J, 2005. **88**(2): p. 1143-55.

43. Portet, T. and R. Dimova, *A New Method for Measuring Edge Tensions and Stability of Lipid Bilayers: Effect of Membrane Composition.* Biophysical Journal, 2010. **99**(10): p. 3264-3273.

44. Milner, S.T. and S.A. Safran, *Dynamic Fluctuations of Droplet Microemulsions and Vesicles.* Physical Review A, 1987. **36**(9): p. 4371-4379.

45. Maxfield, F.R. and I. Tabas, *Role of cholesterol and lipid organization in disease.* Nature, 2005. **438**(7068): p. 612-621.

46. Knorr, R.L., et al., *Membrane Morphology Is Actively Transformed by Covalent Binding of the Protein Atg8 to PE-Lipids.* Plos One, 2014. **9**(12).

47. Alberts, B., *Molecular Biology of the Cell*. 4 ed. 2002, New York: Garland Science.

48. Chen, Y.A. and R.H. Scheller, *Snare-mediated membrane fusion.* Nature Reviews Molecular Cell Biology, 2001. **2**(2): p. 98-106.

49. Matsuoka, K., et al., *COPII-coated vesicle formation reconstituted with purified coat proteins and chemically defined liposomes.* Cell, 1998. **93**(2): p. 263-275.

50. Cureton, D.K., et al., *Vesicular Stomatitis Virus Enters Cells through Vesicles Incompletely Coated with Clathrin That Depend upon Actin for Internalization.* Plos Pathogens, 2009. **5**(4).

51. Veiga, E., et al., *Invasive and adherent bacterial pathogens co-opt host clathrin for infection.* Cell Host & Microbe, 2007. **2**(5): p. 340-351.

52. Dahm, R., et al., *Homeostasis in the vertebrate lens: mechanisms of solute exchange.* Philosophical Transactions of the Royal Society B-Biological Sciences, 2011. **366**(1568): p. 1265-1277.

53. Meier, O., et al., *Adenovirus triggers macropinocytosis and endosomal leakage together with its clathrin-mediated uptake.* Journal of Cell Biology, 2002. **158**(6): p. 1119-1131.

54. Li, Y.H., et al., *Wetting-Induced Budding of Vesicles in Contact with Several Aqueous Phases.* Journal of Physical Chemistry B, 2012. **116**(6): p. 1819-1823.

55. Nikolov, V., R. Lipowsky, and R. Dimova, *Behavior of giant vesicles with anchored DNA molecules.* Biophysical Journal, 2007. **92**(12): p. 4356-4368.

56. Deamer, D.W. and J. Bramhall, *Permeability of Lipid Bilayers to Water and Ionic Solutes.* Chemistry and Physics of Lipids, 1986. **40**(2-4): p. 167-188.

57. Oglecka, K., et al., *Osmotic gradients induce bio-reminiscent morphological transformations in giant unilamellar vesicles.* Frontiers in Physiology, 2012. **3**.

58. Sackmann, E., H.P. Duwe, and H. Engelhardt, *Membrane Bending Elasticity and Its Role for Shape Fluctuations and Shape Transformations of Cells and Vesicles.* Faraday Discussions, 1986. **81**: p. 281-+.

59. Khalifat, N., et al., *Membrane Deformation under Local pH Gradient: Mimicking Mitochondrial Cristae Dynamics.* Biophysical Journal, 2008. **95**(10): p. 4924-4933.

60. Berndl, K., et al., *Shape Transformations of Giant Vesicles - Extreme Sensitivity to Bilayer Asymmetry.* Europhysics Letters, 1990. **13**(7): p. 659-664.

61. Kahya, N., et al., *Spatial organization of bacteriorhodopsin in model membranes - Light-induced mobility changes.* Journal of Biological Chemistry, 2002. **277**(42): p. 39304-39311.

62. Weber, G., et al., *Lipid oxidation induces structural changes in biomimetic membranes.* Soft Matter, 2014. **10**(24): p. 4241-4247.

63. Alvarez-Lorenzo, C., L. Bromberg, and A. Concheiro, *Light-sensitive Intelligent Drug Delivery Systems.* Photochemistry and Photobiology, 2009. **85**(4): p. 848-860.

64. Leung, S.J. and M. Romanowski, *Light-activated content release from liposomes.* Theranostics, 2012. **2**(10): p. 1020-36.

65. Lee, H.M., D.R. Larson, and D.S. Lawrence, *Illuminating the Chemistry of Life: Design, Synthesis, and Applications of "Caged" and Related Photoresponsive Compounds.* Acs Chemical Biology, 2009. **4**(6): p. 409-427.

66. Beharry, A.A., et al., *Fluorescence Imaging of Azobenzene Photoswitching In Vivo.* Angewandte Chemie-International Edition, 2011. **50**(6): p. 1325-1327.

67. Katsonis, N., et al., *Reversible conductance switching of single diarylethenes on a gold surface.* Advanced Materials, 2006. **18**(11): p. 1397-+.

68. Dokic, J., et al., *Quantum Chemical Investigation of Thermal Cis-to-Trans Isomerization of Azobenzene Derivatives: Substituent Effects, Solvent Effects, and Comparison to Experimental Data.* Journal of Physical Chemistry A, 2009. **113**(24): p. 6763-6773.

69. Fliegl, H., et al., *Ab initio calculation of the vibrational and electronic spectra of trans- and cis-azobenzene.* Journal of the American Chemical Society, 2003. **125**(32): p. 9821-9827.

70. Beharry, A.A. and G.A. Woolley, *Azobenzene photoswitches for biomolecules.* Chemical Society Reviews, 2011. **40**(8): p. 4422-4437.

71. Dias, A.R., et al., *Enthalpies of Formation of Cis-Azobenzene and Trans-Azobenzene.* Journal of Chemical Thermodynamics, 1992. **24**(4): p. 439-447.

72. Brieke, C., et al., *Light-Controlled Tools.* Angewandte Chemie-International Edition, 2012. **51**(34): p. 8446-8476.

73. Bleger, D., et al., *o-Fluoroazobenzenes as Readily Synthesized Photoswitches Offering Nearly Quantitative Two-Way Isomerization with Visible Light.* Journal of the American Chemical Society, 2012. **134**(51): p. 20597-20600.

74. Nagle, J.F., *Theory of the Main Lipid Bilayer Phase-Transition.* Annual Review of Physical Chemistry, 1980. **31**: p. 157-195.

75. Korlach, J., et al., *Characterization of lipid bilayer phases by confocal microscopy and fluorescence correlation spectroscopy.* Proceedings of the National Academy of Sciences of the United States of America, 1999. **96**(15): p. 8461-8466.

76. Vist, M.R. and J.H. Davis, *Phase-Equilibria of Cholesterol Dipalmitoylphosphatidylcholine Mixtures - H-2 Nuclear Magnetic-Resonance and Differential Scanning Calorimetry.* Biochemistry, 1990. **29**(2): p. 451-464.

77. Lipowsky, R. and R. Dimova, *Domains in membranes and vesicles.* Journal of Physics-Condensed Matter, 2003. **15**(1): p. S31-S45.

78. Simons, K. and W.L.C. Vaz, *Model systems, lipid rafts, and cell membranes.* Annual Review of Biophysics and Biomolecular Structure, 2004. **33**: p. 269-295.

79. Veatch, S.L. and S.L. Keller, *Seeing spots: Complex phase behavior in simple membranes.* Biochimica Et Biophysica Acta-Molecular Cell Research, 2005. **1746**(3): p. 172-185.

80. Veatch, S.L. and S.L. Keller, *Separation of liquid phases in giant vesicles of ternary mixtures of phospholipids and cholesterol.* Biophysical Journal, 2003. **85**(5): p. 3074-3083.

81. Smith, A.K., et al., *Ternary phase diagram of the lipid mixture sphingomyelin/DOPC/cholesterol.* Biophysical Journal, 2003. **84**(2): p. 372a-372a.

82. Bezlyepkina, N., et al., *Phase Diagram and Tie-Line Determination for the Ternary Mixture DOPC/eSM/Cholesterol.* Biophysical Journal, 2013. **104**(7): p. 1456-1464.

83. Koan, M.M. and G.J. Blanchard, *Gauging the effect of impurities on lipid bilayer phase transition temperature.* Journal of Physical Chemistry B, 2006. **110**(33): p. 16584-16590.

84. Pataraia, S., et al., *Effect of cytochrome c on the phase behavior of charged multicomponent lipid membranes.* Biochimica Et Biophysica Acta-Biomembranes, 2014. **1838**(8): p. 2036-2045.

85. Vequi-Suplicy, C.C., et al., *Vesicles with charged domains.* Biochimica Et Biophysica Acta-Biomembranes, 2010. **1798**(7): p. 1338-1347.

86. Wang, Y., McCammon, J. A., *Introduction to Molecular Dynamics: Theory and Applications in Biomolecular Modeling*. 2012: Springer.

87. Grafmuller, A., J. Shillcock, and R. Lipowsky, *Pathway of membrane fusion with two tension-dependent energy barriers.* Physical Review Letters, 2007. **98**(21).

88. Scheraga, H.A., M. Khalili, and A. Liwo, *Protein-folding dynamics: Overview of molecular simulation techniques.* Annual Review of Physical Chemistry, 2007. **58**: p. 57-83.

89. Sonne, J., et al., *Simulation of the coupling between nucleotide binding and transmembrane domains in the ATP binding cassette transporter BtuCD.* Biophysical Journal, 2007. **92**(8): p. 2727-2734.

90. Marrink, S.J., A.H. de Vries, and D.P. Tieleman, *Lipids on the move: Simulations of membrane pores, domains, stalks and curves.* Biochimica Et Biophysica Acta-Biomembranes, 2009. **1788**(1): p. 149-168.

91. Dickson, C.J., et al., *Lipid14: The Amber Lipid Force Field.* Journal of Chemical Theory and Computation, 2014. **10**(2): p. 865-879.

92. Klauda, J.B., et al., *Update of the CHARMM All-Atom Additive Force Field for Lipids: Validation on Six Lipid Types.* Journal of Physical Chemistry B, 2010. **114**(23): p. 7830-7843.

93. Berger, O., O. Edholm, and F. Jahnig, *Molecular dynamics simulations of a fluid bilayer of dipalmitoylphosphatidylcholine at full hydration, constant pressure, and constant temperature.* Biophysical Journal, 1997. **72**(5): p. 2002-2013.

94. Goetz, R., G. Gompper, and R. Lipowsky, *Mobility and elasticity of self-assembled membranes.* Physical Review Letters, 1999. **82**(1): p. 221-224.

95. Shillcock, J.C. and R. Lipowsky, *Equilibrium structure and lateral stress distribution of amphiphilic bilayers from dissipative particle dynamics simulations.* Journal of Chemical Physics, 2002. **117**(10): p. 5048-5061.

96. Marrink, S.J., et al., *The MARTINI force field: Coarse grained model for biomolecular simulations.* Journal of Physical Chemistry B, 2007. **111**(27): p. 7812-7824.

97. Ruzin, S.E., *Plant microtechnique and microscopy*. 1999, New York: Oxford University Press.

98. Bunzli, J.C.G., *Lighting up cells with lanthanide self-assembled helicates.* Interface Focus, 2013. **3**(5).

99. Aranda, S., et al., *Morphological transitions of vesicles induced by alternating electric fields.* Biophys J, 2008. **95**(2): p. L19-21.

100. Kang, M., et al., *Simplified Equation to Extract Diffusion Coefficients from Confocal FRAP Data.* Traffic, 2012. **13**(12): p. 1589-1600.

101. Brochard, F. and J.F. Lennon, *Frequency Spectrum of Flicker Phenomenon in Erythrocytes.* Journal De Physique, 1975. **36**(11): p. 1035-1047.

102. Duwe, H.P., J. Kaes, and E. Sackmann, *Bending Elastic-Moduli of Lipid Bilayers - Modulation by Solutes.* Journal De Physique, 1990. **51**(10): p. 945-962.

103. Faucon, J.F., et al., *Bending Elasticity and Thermal Fluctuations of Lipid-Membranes - Theoretical and Experimental Requirements.* Journal De Physique, 1989. **50**(17): p. 2389-2414.

104. Schneider, M.B., J.T. Jenkins, and W.W. Webb, *Thermal Fluctuations of Large Quasi-Spherical Bimolecular Phospholipid-Vesicles.* Journal De Physique, 1984. **45**(9): p. 1457-1472.

105. Seifert, U., *The Concept of Effective Tension for Fluctuating Vesicles.* Zeitschrift Fur Physik B-Condensed Matter, 1995. **97**(2): p. 299-309.

106. McMahon, H.T. and J.L. Gallop, *Membrane curvature and mechanisms of dynamic cell membrane remodelling.* Nature, 2005. **438**(7068): p. 590-6.

107. Trajkovic, K., et al., *Ceramide triggers budding of exosome vesicles into multivesicular Endosomes.* Science, 2008. **319**(5867): p. 1244-1247.

108. Lipowsky, R., *Remodeling of membrane compartments: some consequences of membrane fluidity.* Biol Chem, 2014. **395**(3): p. 253-74.

109. Lipowsky, R. and E. Sackmann, *Structure and dynamics of membranes* Vol. 1A. 1995, Amsterdam: Elsevier.

110. Dimova, R., *Giant Vesicles: A Biomimetic Tool for Membrane Characterization*, in *Advances in Planar Lipid Bilayers and Liposomes*, A. Iglič, Editor. 2012, Academic Press. p. 1-50.

111. Fenz, S.F. and K. Sengupta, *Giant vesicles as cell models.* Integrative Biology, 2012. **4**(9): p. 982-995.

112. Bernard, A.L., et al., *Raspberry vesicles.* Biochimica Et Biophysica Acta-Biomembranes, 2002. **1567**(1-2): p. 1-5.

113. Kas, J. and E. Sackmann, *Shape Transitions and Shape Stability of Giant Phospholipid-Vesicles in Pure Water Induced by Area-to-Volume Changes.* Biophysical Journal, 1991. **60**(4): p. 825-844.

114. Menger, F.M. and M.I. Angelova, *Giant vesicles: Imitating the cytological processes of cell membranes.* Accounts of Chemical Research, 1998. **31**(12): p. 789-797.

115. Menager, C., et al., *Lipid bilayer elasticity measurements in giant liposomes in contact with a solubilizing surfactant.* Langmuir, 2008. **24**(9): p. 4968-4974.

116. Riske, K.A., R.L. Knorr, and R. Dimova, *Bursting of charged multicomponent vesicles subjected to electric pulses.* Soft Matter, 2009. **5**(10): p. 1983-1986.

117. Yu, M., et al., *Ellipsoidal Relaxation of Deformed Vesicles.* Phys Rev Lett, 2015. **115**(12): p. 128303.

118. Haluska, C.K., et al., *Time scales of membrane fusion revealed by direct imaging of vesicle fusion with high temporal resolution.* Proc Natl Acad Sci U S A, 2006. **103**(43): p. 15841-6.

119. Petrov, P.G., J.B. Lee, and H.G. Dobereiner, *Coupling chemical reactions to membrane curvature: A photochemical morphology switch.* Europhysics Letters, 1999. **48**(4): p. 435-441.

120. Hamada, T., et al., *Dynamic processes in endocytic transformation of a raft-exhibiting giant liposome.* J Phys Chem B, 2007. **111**(37): p. 10853-7.

121. Long, M.S., A.S. Cans, and C.D. Keating, *Budding and asymmetric protein microcompartmentation in giant vesicles containing two aqueous phases.* J Am Chem Soc, 2008. **130**(2): p. 756-62.

122. Staneva, G., et al., *Detergents induce raft-like domains budding and fission from giant unilamellar heterogeneous vesicles: a direct microscopy observation.* Chem Phys Lipids, 2005. **136**(1): p. 55-66.

123. Yanagisawa, M., M. Imai, and T. Taniguchi, *Shape deformation of ternary vesicles coupled with phase separation.* Phys Rev Lett, 2008. **100**(14): p. 148102.

124. Bleger, D., Z. Yu, and S. Hecht, *Toward optomechanics: maximizing the photodeformation of individual molecules.* Chem Commun (Camb), 2011. **47**(45): p. 12260-6.

125. Finkelmann, H., et al., *A new opto-mechanical effect in solids.* Phys Rev Lett, 2001. **87**(1): p. 015501.

126. Hugel, T., et al., *Single-molecule optomechanical cycle.* Science, 2002. **296**(5570): p. 1103-6.

127. Bonacucina, G., et al., *Colloidal Soft Matter as Drug Delivery System.* Journal of Pharmaceutical Sciences, 2009. **98**(1): p. 1-42.

128. Nii, T. and F. Ishii, *Encapsulation efficiency of water-soluble and insoluble drugs in liposomes prepared by the microencapsulation vesicle method.* International Journal of Pharmaceutics, 2005. **298**(1): p. 198-205.

129. Bisby, R.H., C. Mead, and C.C. Morgan, *Wavelength-programmed solute release from photosensitive liposomes.* Biochemical and Biophysical Research Communications, 2000. **276**(1): p. 169-173.

130. Beharry, A.A. and G.A. Woolley, *Azobenzene photoswitches for biomolecules.* Chem Soc Rev, 2011. **40**(8): p. 4422-37.

131. Dong, S.L., et al., *A photocontrolled beta-hairpin peptide.* Chemistry-a European Journal, 2006. **12**(4): p. 1114-1120.

132. Schrader, T.E., et al., *Light-triggered beta-hairpin folding and unfolding.* Proceedings of the National Academy of Sciences of the United States of America, 2007. **104**(40): p. 15729-15734.

133. Lien, L., et al., *Photomodulated blocking of gramicidin ion channels.* Journal of the American Chemical Society, 1996. **118**(48): p. 12222-12223.

134. Estevez-Torres, A., et al., *Sequence-independent and reversible photocontrol of transcription/expression systems using a photosensitive nucleic acid binder.* Proc Natl Acad Sci U S A, 2009. **106**(30): p. 12219-23.

135. Matsunaga, D., H. Asanuma, and M. Komiyama, *Photoregulation of RNA digestion by RNase H with azobenzene-tethered DNA.* Journal of the American Chemical Society, 2004. **126**(37): p. 11452-11453.

136. Kuiper, J.M. and J.B.F.N. Engberts, *H-aggregation of azobenzene-substituted amphiphiles in vesicular membranes.* Langmuir, 2004. **20**(4): p. 1152-1160.

137. Sato, T., et al., *Photochemically Controlled Ion Permeability of Liposomal Membranes Containing Amphiphilic Azobenzene.* Langmuir, 1991. **7**(10): p. 2330-2335.

138. Higuchi, M., et al., *Photocontrol of Vesicular Adhesion and Functions by a Photoresponsive Polypeptide.* Macromolecules, 1987. **20**(11): p. 2888-2892.

139. Riske, K.A., et al., *Giant vesicles under oxidative stress induced by a membrane-anchored photosensitizer.* Biophys J, 2009. **97**(5): p. 1362-70.

140. Itri, R., et al., *Membrane changes under oxidative stress: the impact of oxidized lipids.* Biophysical Reviews, 2014. **6**: p. 47-61.

141. Caetano, W., et al., *Photo-induced destruction of giant vesicles in methylene blue solutions.* Langmuir, 2007. **23**(3): p. 1307-1314.

142. Diguet, A., et al., *UV-induced bursting of cell-sized multicomponent lipid vesicles in a photosensitive surfactant solution.* J Am Chem Soc, 2012. **134**(10): p. 4898-904.

143. Hamada, T., et al., *Reversible photoswitching in a cell-sized vesicle.* Langmuir, 2005. **21**(17): p. 7626-8.

144. Ishii, K., et al., *Reversible control of exo- and endo-budding transitions in a photosensitive lipid membrane.* Chembiochem, 2009. **10**(2): p. 251-6.

145. Knie, C., et al., *ortho-Fluoroazobenzenes: Visible Light Switches with Very Long-Lived Z Isomers.* Chemistry-a European Journal, 2014. **20**(50): p. 16492-16501.

146. Aranda, S., et al., *Morphological transitions of vesicles induced by alternating electric fields.* Biophysical Journal, 2008. **95**(2): p. L19-L21.

147. Dickson, C.J., et al., *Lipid14: The Amber Lipid Force Field.* Journal of Chemical Theory and Computation, 2014. **10**(2): p. 865-879.

148. Duchstein, P., et al., *Molecular mechanics modeling of azobenzene-based photoswitches.* Journal of Molecular Modeling, 2012. **18**(6): p. 2479-2482.

149. Wang, J., et al., *Development and testing of a general amber force field.* Journal of Computational Chemistry, 2004. **25**(9): p. 1157-1174.

150. Dupradeau, F.-Y., et al., *The R.E.D. tools: advances in RESP and ESP charge derivation and force field library building.* Physical Chemistry Chemical Physics, 2010. **12**(28): p. 7821-7839.

151. Sorin, E.J. and V.S. Pande, *Exploring the Helix-Coil Transition via All-Atom Equilibrium Ensemble Simulations.* Biophysical Journal, 2005. **88**(4): p. 2472-2493.

152. Wehle, M., et al., *Mechanical Compressibility of the Glycosylphosphatidylinositol (GPI) Anchor Backbone Governed by Independent Glycosidic Linkages.* Journal of the American Chemical Society, 2012. **134**(46): p. 18964-18972.

153. Jorgensen, W.L., et al., *Comparison of simple potential functions for simulating liquid water.* The Journal of Chemical Physics, 1983. **79**(2): p. 926-935.

154. Pronk, S., et al., *GROMACS 4.5: a high-throughput and highly parallel open source molecular simulation toolkit.* Bioinformatics, 2013. **29**(7): p. 845-854.

155. van der Spoel, D., et al., *GROMACS: Fast, flexible, and free* J. Comput. Chem., 2005. **26**: p. 1701-1718.

156. Hess, B., et al., *LINCS: a linear constraint solver for molecular simulations.* Journal of Computational Chemistry, 1997. **18**(12): p. 1463-1472.

157. Miyamoto, S. and P.A. Kollman, *SETTLE - an Analytical Version of the SHAKE and RATTLE Algorithm for Rigid Water Models.* Journal of Computational Chemistry, 1992. **13**(8): p. 952-962.

158. Bussi, G., D. Donadio, and M. Parrinello, *Canonical sampling through velocity rescaling.* The Journal of Chemical Physics, 2007. **126**(1): p. 014101.

159. Berendsen, H.J., et al., *Molecular dynamics with coupling to an external bath.* J. Chem. Phys., 1984. **81**(8): p. 3684-3690.

160. Nos\'e, Shuichi, *A unified formulation of the constant temperature molecular dynamics methods.* J. Chem. Phys., 1984. **81**(1): p. 511-519.

161. Hoover, W.G., *Canonical dynamics: equilibrium phase-space distributions.* Phys. Rev. A, 1985. **31**(3): p. 1695.

162. Parrinello, M. and A. Rahman, *Polymorphic transitions in single crystals: A new molecular dynamics method.* J. Appl. Phys., 1981. **52**(12): p. 7182-7190.

163. Darden, T., D. York, and L. Pedersen, *Particle mesh Ewald: An N log (N) method for Ewald sums in large systems.* J. Chem. Phys, 1993. **98**(12): p. 10089-10092.

164. Vrhovec, S., et al., *A microfluidic diffusion chamber for reversible environmental changes around flaccid lipid vesicles.* Lab on a Chip, 2011. **11**(24): p. 4200-4206.

165. Forman, J., M. Dietrich, and W.T. Monroe, *Photobiological and thermal effects of photoactivating UVA light doses on cell cultures.* Photochemical & Photobiological Sciences, 2007. **6**(6): p. 649-658.

166. Bennett, W.F.D., et al., *Molecular View of Cholesterol Flip-Flop and Chemical Potential in Different Membrane Environments.* Journal of the American Chemical Society, 2009. **131**(35): p. 12714-12720.

167. Tieleman, D.P. and S.J. Marrink, *Lipids out of equilibrium: energetics of desorption and pore mediated flip-flop.* J Am Chem Soc, 2006. **128**(38): p. 12462-7.

168. Armstrong, V.T., et al., *Rapid flip-flop in polyunsaturated (docosahexaenoate) phospholipid membranes.* Archives of Biochemistry and Biophysics, 2003. **414**(1): p. 74-82.

169. Miao, L., et al., *Budding Transitions of Fluid-Bilayer Vesicles - the Effect of Area-Difference Elasticity.* Physical Review E, 1994. **49**(6): p. 5389-5407.

170. Svetina, S., M. Brumen, and B. Zeks, *Lipid Bilayer Elasticity and the Bilayer Couple Interpretation of Red-Cell Shape Transformations and Lysis.* Studia Biophysica, 1985. **110**(1-3): p. 177-184.

171. Dobereiner, H.G., et al., *Mapping vesicle shapes into the phase diagram: A comparison of experiment and theory.* Physical Review E, 1997. **55**(4): p. 4458-4474.

172. Evans, E.A., *Bending Resistance and Chemically-Induced Moments in Membrane Bilayers.* Biophysical Journal, 1974. **14**(12): p. 923-931.

173. Helfrich, W., *Blocked Lipid Exchange in Bilayers and Its Possible Influence on Shape of Vesicles.* Zeitschrift Fur Naturforschung C-a Journal of Biosciences, 1974. **C 29**(9-10): p. 510-515.

174. Sheetz, M.P. and S.J. Singer, *Biological-Membranes as Bilayer Couples - Molecular Mechanism of Drug-Erythrocyte Interactions.* Proceedings of the National Academy of Sciences of the United States of America, 1974. **71**(11): p. 4457-4461.

175. Rozycki, B. and R. Lipowsky, *Membrane curvature generated by asymmetric depletion layers of ions, small molecules, and nanoparticles.* J Chem Phys, 2016. **145**(7): p. 074117.

176. Rozycki, B. and R. Lipowsky, *Spontaneous curvature of bilayer membranes from molecular simulations: Asymmetric lipid densities and asymmetric adsorption.* Journal of Chemical Physics, 2015. **142**(5).

177. Deans, J.P., H.D. Li, and M.J. Polyak, *CD20-mediated apoptosis: signalling through lipid rafts.* Immunology, 2002. **107**(2): p. 176-182.

178. Tsui-Pierchala, B.A., et al., *Lipid rafts in neuronal signaling and function.* Trends in Neurosciences, 2002. **25**(8): p. 412-417.

179. Edidin, M., *Shrinking patches and slippery rafts: scales of domains in the plasma membrane.* Trends in Cell Biology, 2001. **11**(12): p. 492-496.

180. Simons, K. and E. Ikonen, *Functional rafts in cell membranes.* Nature, 1997. **387**(6633): p. 569-572.

181. Pike, L.J., *The challenge of lipid rafts.* Journal of Lipid Research, 2009. **50**: p. S323-S328.

182. Eggeling, C., et al., *Direct observation of the nanoscale dynamics of membrane lipids in a living cell.* Nature, 2009. **457**(7233): p. 1159-U121.

183. Honigmann, A., et al., *Scanning STED-FCS reveals spatiotemporal heterogeneity of lipid interaction in the plasma membrane of living cells.* Nature Communications, 2014. **5**.

184. Thomas, J.L., et al., *Large-Scale Coaggregation of Fluorescent Lipid Probes with Cell-Surface Proteins.* Journal of Cell Biology, 1994. **125**(4): p. 795-802.

185. Veatch, S.L. and S.L. Keller, *Organization in lipid membranes containing cholesterol.* Physical Review Letters, 2002. **89**(26).

186. Bagatolli, L.A., *To see or not to see: Lateral organization of biological membranes and fluorescence microscopy.* Biochimica Et Biophysica Acta-Biomembranes, 2006. **1758**(10): p. 1541-1556.

187. Baumgart, T., et al., *Large-scale fluid/fluid phase separation of proteins and lipids in giant plasma membrane vesicles.* Proceedings of the National Academy of Sciences of the United States of America, 2007. **104**(9): p. 3165-3170.

188. Dietrich, C., et al., *Lipid rafts reconstituted in model membranes.* Biophysical Journal, 2001. **80**(3): p. 1417-1428.

189. Veatch, S.L., K. Gawrisch, and S.L. Keller, *Observing immiscible liquid phases in lipid bilayers containing cholesterol by fluorescence microscopy and NMR.* Biophysical Journal, 2003. **84**(2): p. 371a-371a.

190. Bacia, K., P. Schwille, and T. Kurzchalia, *Sterol structure determines the separation of phases and the curvature of the liquid-ordered phase in model membranes.* Proceedings of the National Academy of Sciences of the United States of America, 2005. **102**(9): p. 3272-3277.

191. Wang, J.W., Megha, and E. London, *Relationship between sterol/steroid structure and participation in ordered lipid domains (lipid rafts): Implications for lipid raft structure and function.* Biochemistry, 2004. **43**(4): p. 1010-1018.

192. Muddana, H.S., H.H. Chiang, and P.J. Butler, *Tuning Membrane Phase Separation Using Nonlipid Amphiphiles.* Biophysical Journal, 2012. **102**(3): p. 489-497.

193. Botelho, A.V., et al., *Curvature and hydrophobic forces drive oligomerization and modulate activity of rhodopsin in membranes.* Biophysical Journal, 2006. **91**(12): p. 4464-4477.

194. Pucadyil, T.J. and A. Chattopadhyay, *Role of cholesterol in the function and organization of G-protein coupled receptors.* Progress in Lipid Research, 2006. **45**(4): p. 295-333.

195. London, E., *How principles of domain formation in model membranes may explain ambiguities concerning lipid raft formation in cells.* Biochimica Et Biophysica Acta-Molecular Cell Research, 2005. **1746**(3): p. 203-220.

196. Yasuhara, K., Y. Sasaki, and J. Kikuchi, *A photo-responsive cholesterol capable of inducing a morphological transformation of the liquid-ordered microdomain in lipid bilayers.* Colloid and Polymer Science, 2008. **286**(14-15): p. 1675-1680.

197. Frank, J.A., et al., *Optical Control of Lipid Rafts with Photoswitchable Ceramides.* J Am Chem Soc, 2016. **138**(39): p. 12981-12986.

198. Hamada, T., et al., *Photochemical control of membrane raft organization.* Soft Matter, 2011. **7**(1): p. 220-224.

199. Ramirez, D.M.C., et al., *Lipid phase separation and protein-ganglioside clustering in supported bilayers are induced by photorelease of ceramide.* Soft Matter, 2013. **9**(19): p. 4890-4899.

200. Lira, R.B., et al., *Posing for a picture: vesicle immobilization in agarose gel.* Scientific Reports, 2016. **6**.

201. Baumgart, T., et al., *Fluorescence probe partitioning between L-o/L-d phases in lipid membranes.* Biochimica Et Biophysica Acta-Biomembranes, 2007. **1768**(9): p. 2182-2194.

202. London, E. and D.A. Brown, *Insolubility of lipids in Triton X-100: physical origin and relationship to sphingolipid/cholesterol membrane domains (rafts).* Biochimica Et Biophysica Acta-Biomembranes, 2000. **1508**(1-2): p. 182-195.

203. Korlach, J., et al., *Characterization of lipid bilayer phases by confocal microscopy and fluorescence correlation spectroscopy (vol 96, pg 8461, 1999).* Proceedings of the National Academy of Sciences of the United States of America, 1999. **96**(17): p. 9966-9966.

204. Baumgart, T., S.T. Hess, and W.W. Webb, *Imaging coexisting fluid domains in biomembrane models coupling curvature and line tension.* Nature, 2003. **425**(6960): p. 821-824.

205. Garcia-Saez, A.J., S. Chiantia, and P. Schwille, *Effect of line tension on the lateral organization of lipid membranes.* Journal of Biological Chemistry, 2007. **282**(46).

206. Garcia-Saez, A.J. and P. Schwille, *Stability of lipid domains.* Febs Letters, 2010. **584**(9): p. 1653-1658.

207. Tian, A.W., et al., *Line tension at fluid membrane domain boundaries measured by micropipette aspiration.* Physical Review Letters, 2007. **98**(20).

208. Zakrevskyy, Y., et al., *Photosensitive surfactants: Micellization and interaction with DNA.* Journal of Chemical Physics, 2014. **140**(4).

List of abbreviations

AC	Alternating current
ADE	Area-difference elasticity
BLM	Black lipid membranes
Chol	Cholesterol
CMC	Critical micelle concentration
DAPC	Dirachidoylphosphocholine
DLS	Dynamic light scattering
DOPC	Dioleoylphosphatidylcholine
DPPC	Dioleoylphosphatidylcholine
DPPE-Rh	Dipalmitoylphosphoethanolamine-N- rhodamine
F-azo	Fluoroazobenzene
FRAP	Fluorescence recovery after photobleaching
GUV(s)	Giant unilamellar vesicle(s)
HPLC	High-performance liquid chromatography
ITO	Indium thin oxide
LUV(s)	Large unilamellar vesicle(s)
MC	Monte Carlo
MD	Molecular dynamics
NA	Numerical aperture
PC(s)	Phosphatidylcholine(s)
PDMS	Polydimethylsiloxane
PE(s)	Phosphatidylethanolamine(s)
PI(s)	Phosphatidylinositol(s)
PL(s)	Phospholipid(s)
PMF	Potential of mean force
PS(s)	Phosphatidylserine(s)
ROI	Region of interest
SLB	Supported lipid bilayers
SM(s)	Sphingomyelin(s)

List of figures

Fig.1-1. Structure of PLs and cholesterol 2
Fig.1-2. Lipid self-assembly determined by the shape of lipid molecules 3
Fig.1-3. Essential material properties of phospholipid membranes 5
Fig.1-4. Membrane curvature 6
Fig.1-5. Morphology of GUVs 7
Fig.1-6. Images of GUV taken with phase-contrast and fluorescence microscopy 7
Fig.1-7. Schematic drawing of eukaryotic plasma membrane 9
Fig.1-8. Membrane shapes in cells and organelles 9
Fig.1-9. Transmission electron micrographs of different stages during (A) exocytosis and (B) endocytosis. 10
Fig.1-10. Structure of azobenzene's *trans* and *cis* isomers 12
Fig.1-11. (A) Molecular structure of F-azo in both *trans* and *cis* conformation. (B) Absorption spectra of F-azo, adapted from 13
Fig.1-12. Schematic drawing of the gel and fluid state of the phospholipid bilayer 14
Fig.1-13. Domains in l_d (red) and l_o (dark) phase in phase separated GUVs made of DPPC:DOPC:Chol, in molar ratio 1:1:1 15
Fig.1-14. Gibbs phase triangle for a DPPC-DOPC-Chol lipid mixture 16
Fig.1-15. MD modelling of DOPC in different levels of detail 17

Fig.2-1. Structure of the used lipids 18
Fig.2-2. Electroformation of GUVs 19
Fig.2-3. Simplified scheme of the optical path of a phase-contrast (A) and epifluorescence microscope (B) 21
Fig.2-4. Morphological diagram of GUVs in the presence of an electric field at different field frequencies and conductivity conditions 22
Fig.2-5. Vesicle electrodeformation 23
Fig.2-6. Schematic representation of FRAP 24
Fig.2-7. Fluorescence intensity line profile of bleached area at the first image after the bleaching 25
Fig.2-8. Detection of the vesicle contour 26

Fig.3-1. Spectral irradiance of 100 watt high pressure mercury lamp 34

Fig.3-2. Aggregate structures of F-azo 34

Fig.3-3. Chromatograms of filtered F-azo molecules and LUVs 36

Fig.3-4. Dynamic response of one quasi-spherical vesicle to photoisomerization of F-azo at bulk concentration of 0.25 mM 37

Fig.3-5. Effect of UV light (365 nm) on F-azo-free GUV 37

Fig.3-6. MD simulations of one F-azo molecule in a DOPC bilayer composed of 256 lipids 38

Fig.3-7. Deformation of a vesicle in the presence of electric field 40

Fig.3-8. Deformation and budding of a vesicle caused by F-azo conformational change in the membrane at two different F-azo concentrations: (A) 0.25 mM and (B) 0.1 mM 41

Fig.3-9. Degree of deformation during budding-reabsorption processes 42

Fig.3-10. Schematic presentation of a part of the morphological diagram and possible pathways that the vesicle can take during the UV irradiation 43

Fig.3-11. Influence of the sugar asymmetry on the vesicle morphology 45

Fig.3-12. Dynamic response of vesicles grown in glucose and diluted in sucrose to photoisomerisation of F-azo (0.25 mM) 45

Fig.3-13. Sketch of the mechanisms of the observed budding event at molecular level 46

Fig.4-1. Location within the phase diagram of the different lipid compositions that were used 49

Fig.4-2. Temperature control chamber 50

Fig.4-3. Fluorescence microscopy images acquired at room temperature (23°C) before and after UV light irradiation of phase-separated GUVs both with and without F-azo 53

Fig.4-4. Effect of UV light on the miscibility transition temperature of vesicles made of composition **B** 54

Fig.4-5. Miscibility transition curves of vesicles made of (A) composition **A** and (B) composition **B** 55

Fig.4-6. Fluorescence intensity recovery curves after photobleaching without (upper panels) and with F-azo (lower panels) 57

Fig.4-7. Effect of F-azo molecules on the lateral lipid diffusion in both l_d (only DOPC) and l_o (7:3 DPPC/Chol) phase 58

Fig.4-8. Bending rigidity of vesicles made of DOPC incubated with and without F-azo measured at room (23°C) temperature 59

Fig.4-9. Schematic representation of F-azo isomerization in phase-separated membranes 60